GEOPOLYMER COMPOSITES AND THEIR APPLICATIONS IN STRESS WAVE MITIGATION

BY

SHINHU CHO

DISSERTATION

Submitted in partial fulfillment of the requirements
for the degree of Doctor of Philosophy in Mechanical Engineering
in the Graduate College of the
University of Illinois at Urbana-Champaign, 2015

Urbana, Illinois

Doctoral Committee:

Professor Alexander F. Vakakis, Chair
Professor Waltraud M. Kriven, Director of Research
Professor Jian Ku Shang
Assistant Professor Paramita Mondal

ABSTRACT

In recent years, environmentally friendly materials have been the focus as alternatives to ordinary Portland cement (OPC), which generates about 6% of the total carbon dioxide emission in the world today and contributes to global warming. An alternative material to cement is aluminosilicate inorganic polymer, also known as "geopolymer" which emits about 80% less CO_2 than OPC. Therefore, the chemical, mechanical, thermal and electrical properties of geopolymers have been of interest for the past two decades.

The processes and microstructures of potassium-based geopolymer ($K_2O \cdot Al_2O_3 \cdot 4SiO_2 \cdot 11H_2O$) have been studied by many researchers with various techniques. However, the brittleness and relatively lower strength limited the use of geopolymer in certain applications. Therefore, short carbon fibers (60 and 100 μm) have been introduced to reinforce the mechanical properties of potassium based geopolymer. The proper mixing and drying conditions of carbon fiber reinforced potassium geopolymer (C_f KGP) were determined since the mechanical properties varied in wide range depending on the drying conditions. Various static mechanical tests (flexure, uniaxial compression, hardness, toughness and biaxial tensile tests) and statistical analyses of brittle fractures (Weibull distribution) have been performed to investigate the optimal mechanical strengths of C_f KGP composites. In addition to the static measurements, the Young's and shear moduli of C_f KGP have been measured by dynamic methods such as impulse excitation (IE) and resonant ultrasound spectroscopy (RUS) and compared with various theoretical models.

Graphene nanoplatelets have high mechanical, electrical and thermal properties that can significantly improve the desired properties of composites at even low contents. 1, 2 and 3 wt%

of graphene nanoplatelet-reinforced, potassium geopolymers (GNP KGP) were prepared and their microstructures were investigated by SEM, XRD and Raman spectroscopy. The mechanical properties such as flexure strength, Weibull modulus, Vickers hardness and Young's modulus were measured by four-point flexure, microindentation and impulse excitation testing. In addition to mechanical properties, the electrical and thermal properties of GNP KGP were investigated by measuring electrical resistances and thermal conductivities. Moreover, silicon functionalized graphene nanoplatelets (sGNP) were prepared in order to enhance interfacial bonding between GNP and the geopolymer matrix. The various mechanical properties of sGNP KGP were measured and compared with GNP KGP, in order to investigate the effect of silicon functionalization.

Due to their similarity with concrete, geopolymers have been mainly used as structural materials. With documented chemical and mechanical properties of geopolymers, their use could be expanded to applications in many disciplines. In this work, geopolymers were used as granular media and displayed interesting dynamic behavior for stress wave mitigation and as acoustic metamaterials. The fabrication of geopolymer beads was achieved by simple injection into a Polydimethylsiloxane (PDMS) polymer mold. Based on the mechanical properties of geopolymers, the dynamic responses of homogeneous and dimer chains were theoretically predicted and experimentally investigated under impulse excitation. By substituting metal beads for geopolymer beads which are 6 times lighter, a linear array of lightweight granular media was created to mitigate the effects of a stress wave.

ACKNOWLEDGEMENTS

Thanks to my advisor, Professor Waltraud M. Kriven, for her advice and support of this research. I have learned a lot from her not only about research but also about maturity. I really enjoyed to discuss with her any topics, in research and life. Needless to say, my Ph.D. would not be possible without her help. It is also my pleasure to say thank you to Professor Vakakis, for his advice on the nonlinear dynamics and generosity to allow me to use his laboratory. A great deal of appreciation goes to the committee members and the Kriven Research Group for their valuable advice and comments. I would like to thank the Korean graduate students in the Department of Mechanical Science and Engineering and also thanks to the MechSE Department and all the staff members. I would like to say thanks to my parents and parents-in-law for their endless support to achieve this goal. At last but not least, I would like to thank my wife, Myoung Eun An, and family, Ryan Hyunwoo Cho and Julia Eunseo Cho, for their endless support, patience and love throughout this work.

TABLE OF CONTENTS

CHAPTER 1: INTRODUCTION

1. 1 Overview of Geopolymers

Geopolymers are an inorganic polymer containing alumina, silica, an alkali metal oxide and water. Since the geopolymer are liquid mixtures, complex shapes of final products can be molded by a simple cast process. Geopolymers are cured at room temperature for 24 hours and the period of curing time reduces at higher curing temperatures.[1, 2] The microstructure of geopolymers is X-ray amorphous with chemical formula of $M_2O•Al_2O_3•4SiO_2•11H_2O$, where the alkali metal cations such as sodium (Na), potassium (K) or cesium (Cs) have been used for fully reacted geopolymer which was investigated by TEM and EDS analyses.[3] In my work, the composition of geopolymers is based on potassium as an alkali metal source and the 1:1:4:11 composition with a curing temperature of 50 ℃ for 24 hours. This composition resulted in the highest mechanical properties and the most uniform particulate size (around 20 ~ 30 nm) with fully reacted phase of geopolymer. The sub-nanoporosity inside the individual precipitates of potassium geopolymer was measured by HRTEM and the nano porosity of geopolymers is approximately 40% by volume.[4]

There are three-part chemical reactions to form geopolymers. The aluminosilicate source (metakaolin) is dissolved into highly alkaline solution (waterglass). The waterglass is the mixture of metal cations, silica fume and deionized water. Once the aluminosilicate source dissolves in waterglass, the polycondensation of SiO_4 and AlO_4^- tetrahedra occurs according to the reaction

$$2Si(OH)_4 + Al(OH)_4^- \rightarrow (\text{-Si-O-Al-O-Si-O-}) + 6H_2O.$$

The alkali ion (K^+) attacks the amorphous metakaolin to form AlO_4^- and remains near the polymeric chain in order to charge balance the negatively charged Al^{3+} ions in IV-fold coordination.[3] Finally, the polymerized chain precipitates into a rigid, inorganic polymer.

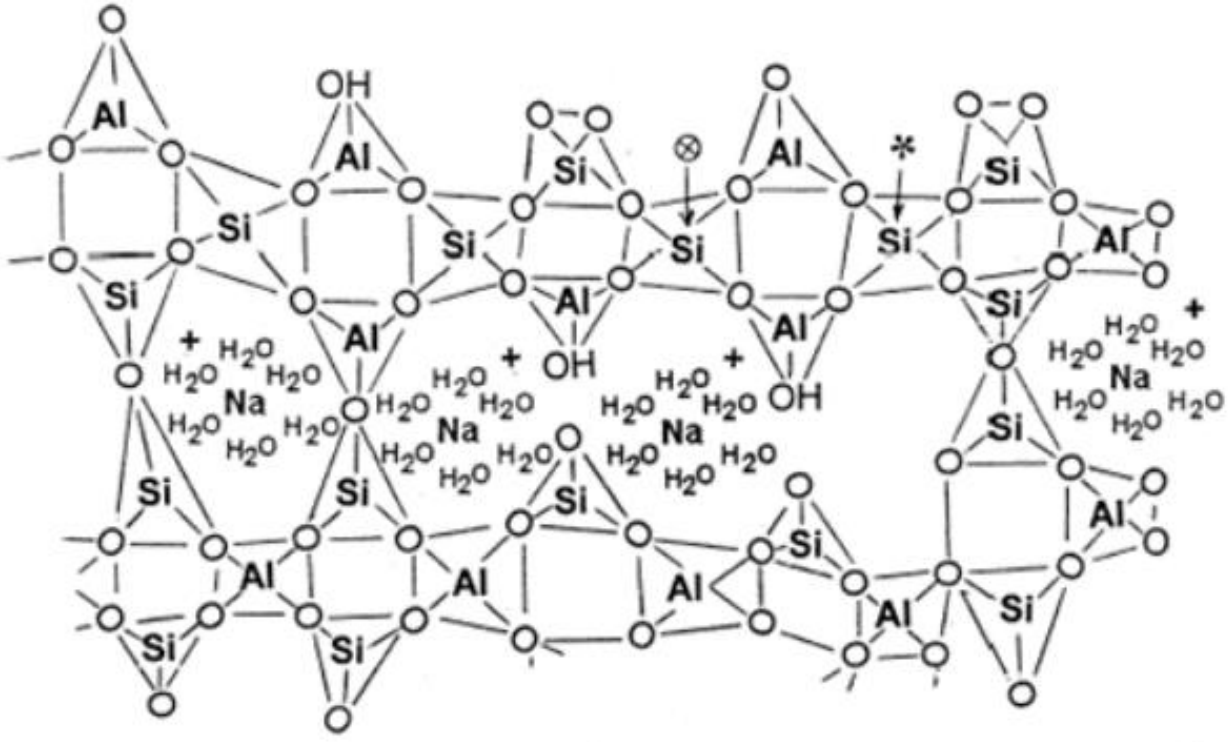

Fig. 1.1. The schematic of geopolymer molecular structure.[3]

Geopolymers are one of the alternatives to ordinary Portland cement (OPC) generating 6% of the total carbon dioxide emission in the world. The geopolymers can reduce 80% of the emission of carbon dioxide compared to the cement since the geopolymers produce only 0.2 tons of carbon dioxide for every ton of production.[3] With the abundance of aluminosilicate sources in the world, the cost will be more efficient in the near future than OPC.[2, 5] Geopolymers can bond with other types of materials such as metal, ceramics and glasses.[3] Due to the ease of synthesis and adhesion to many reinforcements, geopolymers can be used as a good binder or matrix for composites. Thus, the maximum load can be transferred to reinforcements in geopolymer composites and subsequently the strength of geopolymer composites increase. The strength or toughness of geopolymers can be modified by adding different types of reinforcements. There

are a wide range of reinforcements such as particulates, short fibers, continuous fibers and woven fabrics. Geopolymers have not only high strength but also rapid setting, high resistance to acids and alkali, high thermal resistance and high endurance to thermal shock.[3]

Potassium geopolymer is stable at high temperatures around 1000 ℃ before crystallization occurs. The cost of potassium is higher than sodium but much cheaper than cesium. The particle size distribution of potassium geopolymer is much more uniform than sodium but less than cesium. At higher temperature, the potassium geopolymer with 1:1:4:11 ratio turned into the cubic leucite ($KAlSi_2O_6$) in the range of 1000 and 1100 ℃. Leucite can be used for many dental applications. The cubic phase of potassium geopolymer undergoes a phase transformation during the cooling process. The cubic to tetragonal phase transformation occurs at 650 ℃ on cooling and at 450 ℃ on heating. Leucite has a high melting point (1693 ℃), which is good as a refractory or thermal barrier coating material and a high coefficient of thermal expansion (15.1 – 31 x 10^{-6} / ℃K), which is useful as a cermet.[6] The cubic phase of leucite can be stabilized by forming a solid solution with cesium.[7] The low viscosity of potassium geopolymer slurry allows ease of manufacture as well as low cost. Therefore, potassium geopolymer was mainly used in this work.

Since geopolymer contains 11 moles of water at the beginning, the dehydration of geopolymer should be carefully considered to avoid damage to the final material. Most of the water evaporates below 100 ℃ where the water was physically attached near the surface of geopolymer. At this range, the evaporation of water did not damage the material.[3] From 100 to 300 ℃, the chemically bonded or interstitial water dehydrates. Above 300℃, dehydration of OH groups occurs.[3] The shrinkage of geopolymer during dehydration of chemically bonded water induces microcracks in the material and crack sizes increase with increasing temperature. Once

the microcracks are present in the material, further crack propagation will be induced by stress gradients during dehydration when the chemically bound water is intensively extracted by capillary forces and contraction.[3 4, 8] In order to avoid crack developments during dehydration, the reinforcements are added to bridge the cracks as they develop and to provide the pathways for graceful water evaporation.[9] In this work, most of the geopolymer composites were tested and used at ambient temperatures. Although the extraction of surface water did not cause high internal stresses, the pure potassium geopolymers were weak enough to be damaged by desiccant dehydration. Thus, the drying rate was controlled by the humidity chamber at 20℃ with 30% humidity.

1. 2 Reinforcement Materials

Although geopolymers have higher compressive strengths than OPC, the brittleness of ceramics limits their possible applications. Therefore, many types of reinforcements, particulates, short or continuous fibers, and woven fibers has been used to enhance the mechanical properties. Recently, natural fibers have also been considered to improve the strength of geopolymers with low cost and low impact to the environment. In this work, the short carbon fibers and graphene nano platelets have been used to increase the flexural strength, hardness and elastic modulus without deteriorating the benefits of simple processing of geopolymer composites. In this section, different types of short fibers and particulates, which are currently used as reinforcements, are discussed.

Two different lengths (1/2 and 1/4 inch) of basalt fibers have been used to reinforce potassium geopolymers.[10] The aspect ratio of basalt fiber was 967:1 and 488:1, respectively. Such a high aspect ratio resulted in high flexural strengths (19.5 and 27 MPa at 10 wt% chopped

fiber additions) of geopolymer, at room temperature. The chopped polypropylene fibers were also proposed to increase the mechanical properties of sodium based geopolymers. The 0.5", 1" and 2" fibers were used with different fiber contents of 0.92, 1.01, 1.32, 2.48 wt%. The most reliable and highest flexure strengths were obtained with 2" long fibers at 2.48 wt%.[11] The 60 and 100 μm long short carbon fibers were used to reinforce the potassium geopolymer at 5, 10, 15 and 20 wt% of fiber contents. The detail of fibers and carbon fiber reinforced potassium geopolymer will be described in the chapters 2 and 3.

Chamotte and mullite particulates were utilized as reinforcements for potassium geopolymer. Chamotte contains significant amounts of crystalline mullite, so that the powder did not react with the geopolymer slurry during curing and remained in the composite as a reinforcement. The chamotte is good for ceramic bonding in creep resistant application or refectory material due to its high mullite content.[12] At ambient temperature, the 50 wt% of chamotte content increased the flexural strength of potassium geopolymer from 8.7 to 15 MPa. Moreover, the statistical analysis showed that the reliability increased by approximately 6 times at 50 wt% of chamotte content compared to that of pure potassium geopolymer. Alumina platelets (WCA 50) were used as reinforcements in the potassium geopolymer with Nextel woven fabric composite panels. The alumina platelets have 5:1 aspect ratio and crystalline powder with 99% purity. The flexural strength increased from 2 to 20 MPa at room temperature and it further increased up to 40 MPa at high temperature, 600 ℃. Graphene nanoplatelets were used in this study to enhance not only the mechanical properties but also the electrical and thermal properties of geopolymer composites for possible applications in the field of electrical or thermal ceramics. The detail of materials, processing and properties will be described in the chapter 4.

1. 3 Energy Dissipation by Toughening

There are two big categories of energy dissipation. One of them is where the material itself consumes the energy and another mechanism is by structural or architectural energy dissipation. For this section, the energy dissipation of material by toughening mechanisms will be discussed.

There are three types of toughening mechanisms for fiber reinforced brittle materials such as geopolymer, glass and ceramic composites.[13] The first mechanism is fiber pullout which induces the crack deflection at fiber-matrix interfaces. Thus, fiber pullout toughening can be carried out by coating the fiber to form an inherently low fracture toughness. With high interfacial bonding between fiber and matrix, the cracks propagate through the fibers rather than pullout the fibers and subsequently show cleavage fractures. Secondly, a similar mechanism of toughening can be used with fine-scale matrix porosity, avoiding the need for a fiber coating. For this mechanism, the porous matrix should be phase compatible with the fibers to have intimate contact for its durability. The third mechanism is the use fugitive coatings, which leaves a narrow gap at the fiber and matrix interface.

Phase transformation of ceramic materials can be used to enhance the toughness of ceramic matrix composites. The crack is deflected at the interface between two different materials due to their elastic mismatch. The higher the elasticity mismatch, the more deflection occurs at the interface. The deflection is promoted when the crack propagates from an elastic material to a stiff material.[14] This analysis explains that the lower the interfacial bonding between fiber and matrix interface increases the toughness of material as we described above. This indicates that the weak matrix, which results in elastic material, needs to be formed in the ceramic matrix composites to achieve crack deflections. The transformation weakening

consumes the incoming energy to trigger the transformation and the shrinkage of transformation weaken interfacial bonding (or debonding) and lower its stiffness. In subsequence, the crack deflects through favorable ways at the weaken interface due to the transformation and it results in further toughening of composites.

1. 4 Granular Media in Stress Wave Mitigation

The structural or architectural designed materials absorb more energy than do those of monolithic materials of the same composition. The complex biominerals such as nacre, mollusc shells and crustacean have been reported to have a much higher fracture toughness than that of monolithic ceramics.[15] This motivated three dimensional architectures include the size-effect on a nano or sub-nano scale where the material has totally different properties at small sizes.

In order to scale up the effect of high energy absorption by designing the architecture of materials rather than change the material properties, the woodpecker-inspired shock isolation[16] will be discussed in this chapter. The sponge bone within the skull of the woodpecker inspired a mimicking man-made structure by using micro-granular beads in a metal housing. This shock isolation was tested by using a vibration exciter up to 25 kHz. This experiment demonstrated that the cut-off frequency (2.2-15.8 kHz) and roll-off steepness (-155.0 to -78.7 dB decade^{-1}) were inversely proportional to the size of micro beads (68-875 μm). The vibration absorptivity (0.23-0.87) increased as the size of beads increased. The high speed air gun experiment up to 60,000g was carried out to verify the woodpecker's shock isolation effect. The granular beads embedded shock isolation was superior in shock absorption compare to that of conventional hard resin based shock isolation.[16]

These types of work indicated that the designed structures of materials (especially granular media) can absorb more energy than the monolithic materials. In this work, we studied the effect of strongly nonlinear dynamics of granular media on stress wave mitigation in the size of mm scale. Furthermore, the geopolymer beads have been used as granular media, which are conventionally composed of metal beads, in order to achieve lightweight granular acoustic metamaterial. The details of experimental results and discussion are in the chapter 5.

1. 5 References

1. R. E. Lyon, "Fire Response of Geopolymer Structural Composites." in. DTIC Document, 1996.

2. S. A. Bernal, E. D. Rodríguez, R. M. de Gutiérrez, M. Gordillo and J. L. Provis, "Mechanical and Thermal Characterisation of Geopolymers Based on Silicate-Activated Metakaolin/Slag Blends," *Journal of Materials Science,* **46**[16] 5477-86 (2011).

3. J. Davidovits, "Geopolymers and Geopolymeric Materials," *Journal of Thermal Analysis and Calorimetry,* **35**[2] 429-41 (1989).

4. W. Kriven, J. Bell and M. Gordon, "Microstructure and Nanoporosity of as-Set Geopolymers," *Mechanical Properties and Performance of Engineering Ceramics II: Ceramic Engineering and Science Proceedings,* **27**[2] 491-503 (2008).

5. J. Van Jaarsveld, J. Van Deventer and G. Lukey, "The Effect of Composition and Temperature on the Properties of Fly Ash-and Kaolinite-Based Geopolymers," *Chemical Engineering Journal,* **89**[1] 63-73 (2002).

6. J. L. Bell, P. E. Driemeyer and W. M. Kriven, "Formation of Ceramics from Metakaolin-Based Geopolymers. Part Ii: K-Based Geopolymer," *Journal of the American Ceramic Society,* **92**[3] 607-15 (2009).

7. P. He, D. Jia, M. Wang and Y. Zhou, "Effect of Cesium Substitution on the Thermal Evolution and Ceramics Formation of Potassium-Based Geopolymer," *Ceramics International,* **36**[8] 2395-400 (2010).

8. J. L. B. W. M. Kriven, M. Gordon, and G. Wen,, "Geopolymers: More Than Just Cements," *World Congress Geopolymer* Geopolymer, Green Chemistry and Sustainable Development Solutions 179-83 (2005).

9. S. S. Musil, G. Kutyla and W. Kriven, "The Effect of Basalt Chopped Fiber Reinforcement on the Mechanical Properties of Potassium Based Geopolymer," Ceram. Eng. Sci. Proc., **33**[10] 31-42 (2012).

10. E. Rill, D. Lowry and W. Kriven, "Properties of Basalt Fiber Reinforced Geopolymer Composites," Ceram. Eng. Sci. Proc., **31**[10] 57-69 (2010).

11. D. R. Lowry and W. M. Kriven, "Effect of High Tensile Strength Polypropylene Chopped Fiber Reinforcements on the Mechanical Properties of Sodium Based Geopolymer Composites," Ceram. Eng. Sci. Proc., **31**[10] 47-56 (2010).

12. V. A. Estani, A. D. Mazzoni and E. F. Aglietti, "Vibrocast Refractories-Influence of Chamotte Grains on Thermochemical Properties," *Refractories Applications and News,* **10**[4] 10-13 (2005).

13. F. W. Zok, "Developments in Oxide Fiber Composites," *Journal of the American Ceramic Society,* **89**[11] 3309-24 (2006).

14. D. Tullock, I. Reimanis, A. Graham and J. Petrovic, "Deflection and Penetration of Cracks at an Interface between Two Dissimilar Materials," *Acta Metallurgica et Materialia,* **42**[9] 3245-52 (1994).

15. D. Jang, L. R. Meza, F. Greer and J. R. Greer, "Fabrication and Deformation of Three-Dimensional Hollow Ceramic Nanostructures," *Nature materials,* **12**[10] 893-98 (2013).

16. S.-H. Yoon, J.-E. Roh and K. L. Kim, "Woodpecker-Inspired Shock Isolation by Microgranular Bed," *Journal of Physics D: Applied Physics,* **42**[3] 035501 (2009).

CHAPTER 2: SHORT CARBON FIBER-REINFORCED, GEOPOLYMER COMPOSITES

PART I. INTRINSIC MECHANICAL PROPERTIES

2. 1 Abstract

Geopolymers are aluminosilicate, inorganic, polymeric materials which are cured from the liquid phase under ambient conditions. Just as with ceramics, the brittleness of geopolymers limits their potential applications. Carbon fiber reinforcements of 60 μm in length were used to increase not only strength but also fracture toughness which was also compared with values from 100 μm reinforcements of geopolymer composites. In this study, the mechanical properties of randomly oriented, short carbon fiber-reinforced, potassium geopolymers have been investigated by four-point bending and Vickers hardness testing. The results measured values of four-point flexure strength (14 ± 2 MPa), fracture modulus (5 ± 0.4 GPa), Weibull modulus (23), fracture toughness (0.5 ± 0.1 MPa√m for 60 μm and 0.5 ± 0.3 MPa√m for 100 μm), as well as hardness (439 ± 23 MPa) which reached a maximum at 15 wt% fiber content.

2. 2 Introduction

In recent years, environmentally friendly materials have been studied as alternatives to ordinary Portland cement (OPC), which generates about 6% of the total carbon dioxide emission in the world today and contributes to global warming.[1, 2, 3] An alternative material to cement is aluminosilicate inorganic polymer, also known as "geopolymer" which emits about 80% less CO_2 than OPC. Therefore, the chemical, mechanical, thermal and electrical properties of geopolymers have been of interest for the past two decades.[4, 5, 6, 7, 8, 9]

Geopolymer itself is an inorganic ceramic polymer having good strength, rapid setting, substantial resistance to acid, alkali and temperature properties.[10, 11, 12, 13, 14, 15] However, the brittle nature of geopolymer, like that of ceramics limits its possible applications. Therefore, geopolymers reinforced with various fibers such as basalt,[16 17] PVA,[18] polypropylene[19], corn husk[20], jute[21], fique[22], malva[23], rice husk[24] and cotton[25] have been studied rigorously by different researchers in order to improve their mechanical properties. Carbon fiber reinforced geopolymers have more advantages compared to other fibers due to their high elastic modulus, strength and electrical conductivity.[26] Recently, a sheet-like, short carbon preform was used to reinforce a geopolymer and the flexural strength was enhanced by up to 5 times with 7 mm long carbon fibers.[26, 27]

However, such long and sheet-like carbon fibers are restricted for use in geopolymer composites having complex structures or require a machining process to achieve desired configurations. The mechanical properties of randomly oriented, short carbon fiber-reinforced geopolymer have not been reported yet. Therefore, in this paper we have investigated the mechanical properties of randomly oriented carbon fibers of 60 µm in length by 7 µm in diameter, with 5, 10, 15 and 20 wt% loadings corresponding to 3.9, 7.9, 12 and 16.1 vol%, respectively, in potassium geopolymer followed by statistical analyses and Weibull moduli determination.

2. 3 Experimental Procedures

a. Composite Processing

Table 2.1. Properties of Milled Carbon Fiber

Average Length (µm)	Average Diameter (µm)	Bulk Density (g/l)	Carbon Density (g/cm^3)	Young's Modulus (GPa)	Tensile Strength (GPa)	Ultimate Elongation (%)	Electrical Resistivity (mmΩ-cm)
60 and 100	7	550	1.82	225	4.275	1.9	1.38

Milled short carbon fibers (Tenax® –A HT M100) were commercially available from Toho Tenax® (Toho Tenax America, Inc., Rockwood, TN) and the fiber characteristics supplied by the company are summarized in Table 2.1. Note that the average diameter was 7 µm which resulted in an aspect ratio of 9:1 for 60 µm carbon fiber and 14:1 for 100 µm. For some applications, high aspect ratios provided sufficient mechanical reinforcement and electrical conductivities to produce a useful ceramic composite. In our study, we focused mainly on the mechanical improvement of carbon fiber-reinforced, potassium geopolymer composites. Before incorporating the carbon fibers, potassium geopolymer was synthesized by mixing with potassium silicate solution, (waterglass), and metakaolin (Metamax HRM, BASF Corp., Florham Park, NJ). The final chemical formula of potassium geopolymer was $K_2O \cdot Al_2O_3 \cdot 4SiO_2 \cdot 11H_2O$. In order to decrease the unreacted metakaolin phase in geopolymer, we used a high shear mixer (Model RW20DZM, IKA, Wilmington, NC) for 5 minutes at 2000 rpm, followed by additional planetary mixing (Thinky ARE-250, Intertronics, Kidlington, Oxfordshire, UK) for 3 minutes at 1200 rpm, and then followed by degassing for 3 minutes at 1400 rpm, in order to remove air bubbles from the geopolymer slurry. Once the geopolymer slurry was prepared, the carbon fibers were loaded into the slurry at different weight percentages and then mixed by hand and then Thinky mixed again. The carbon fiber reinforced potassium geopolymer (C_f KGP) was cured at 50℃ for 24 hours and then dried in a

humidity controlled chamber (1000H Series Temperature/Humidity Chamber, TestEquity, Moorpark, CA) at 20℃ and 30% relative humidity for 7 days. The details of fiber orientations and distributions were observed by subsequent SEM images in Figs. 2.2 and 2.3.

b. Mechanical Testing

i. Four-point Flexure

The C_f KGP slurry was poured end-on into 1 x 1 x 10 cm Delrin molds to minimize bubble formation on the surfaces and to fabricate flexural samples. The four-point bending test was performed in an Instron according to the ASTM C78/C78M-10 standard.[28] In order to match with the standard loading rate of 1.0 MPa/min, the cross head loading rate based on the sample dimension was set as 23 N/min. The upper and lower spans of the 4-point fixture were 20 and 40 mm. The flexural strength was calculated based on Eq. (2.1).

$$\sigma_{\text{strength}} = \frac{3PL}{4bd^2} \tag{2.1}$$

Here σ is the flexure strength, P is the flexure load, L is lower span, b is sample width, and d is sample thickness, respectively. The flexure modulus was determined as the slope of the stress versus strain curve of the flexure test.

ii. Fracture Toughness

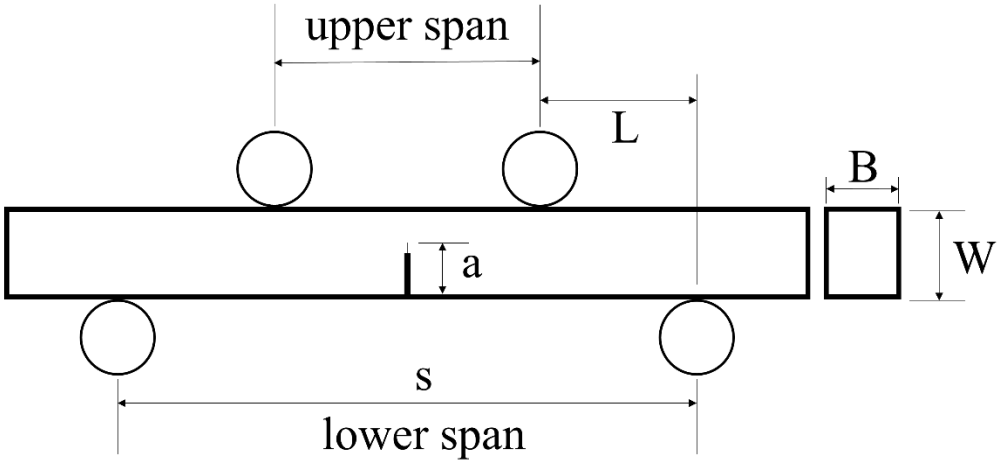

Fig. 2.1. Configuration of the single edge, notched beam fracture test.

The 1 x 1 x 10 cm Delrin mold was also used to prepare single edge-notched beam (SENB) specimens based on the ASTM D5045[29] standard as shown in Fig. 2.1. The initial edge notch was generated by cutting the material with a band saw and then the crack was sharpened by a razor blade to make a sharp tip. The initial length of edge, a, lay in the range $0.45 < \alpha = a/W < 0.55$. The specimens were tested with the same fixture as was used for the flexure test. The span length of the lower span, s, was 40 mm. The distance L was 10 mm since the length of the upper span was 20 mm. The fracture toughness, K_{IC}, was calculated by following Eqs. (2.2), (2.3) and (2.4).

$$K_{IC} = \sigma\sqrt{\pi a} * F(\alpha) \tag{2.2}$$

$$\sigma = \frac{3P_c L}{BW^2} \tag{2.3}$$

$$F(\alpha) = 1.122 - 1.121\alpha + 3.740\alpha^2 + 3.873\alpha^3 - 19.05\alpha^4 + 22.55\alpha^5 \tag{2.4}$$

Hardness

The hardness of C_f KGP was investigated by using Vickers microindentation. The surface of the specimen was cleaned and more than 10 indents were chosen from which to measure the hardness. In order to avoid interference from neighboring indents, these were separated by a distance of more than 10 times larger than the diagonal length of a single indent. The applied force was fixed at 1 kg load for all of the specimens. The loading rate was 0.3 mm/sec followed by 10 sec holding time. Since the carbon fiber was in the 60 µm size, microindentation would be suitable for C_f KGP in order to investigate the overall effect of the reinforcement on the geopolymer. With the measured average diagonal length, d, and the applied force, F, the Vickers hardness was calculated from Eq. (2.5).

$$\mathrm{HV} = \frac{\mathrm{F}}{\mathrm{A}} = \frac{1.8554F}{d^2} \tag{2.5}$$

c. Statistical Analysis

In general, for a brittle material, the average value of the fracture test is not reliable due to the defects present randomly inside the material. Therefore, a Weibull analysis based on the ASTM C1239[30] standard needed to be conducted to understand the fracture behavior of brittle materials such as ceramics, cements, and geopolymers. The Weibull modulus is a dimensionless parameter of the Weibull distribution.

$$\mathrm{P_f} = 1 - \exp[-\left(\frac{\sigma}{\sigma_\theta}\right)^m] \tag{2.6}$$

The Weibull modulus, m, can be calculated from Eq. (2.6). P_f is the probability of failure at a certain value σ of the strength, σ_θ is the Weibull characteristic strength associated with test specimens. A high value of Weibull modulus indicates that the value of strength is distinctly confined to a certain narrow range of values. On the other hand, a lower Weibull modulus has

scattered data points which meant a wide range of strength values. In order to estimate the Weibull modulus, 20 samples were tested in 4-point bending and a 95 % confidence interval was used in this statistical analysis. The linear regression was also performed to plot the Weibull distribution of C_f KGP.

2. 4 Results

a. Microstructures

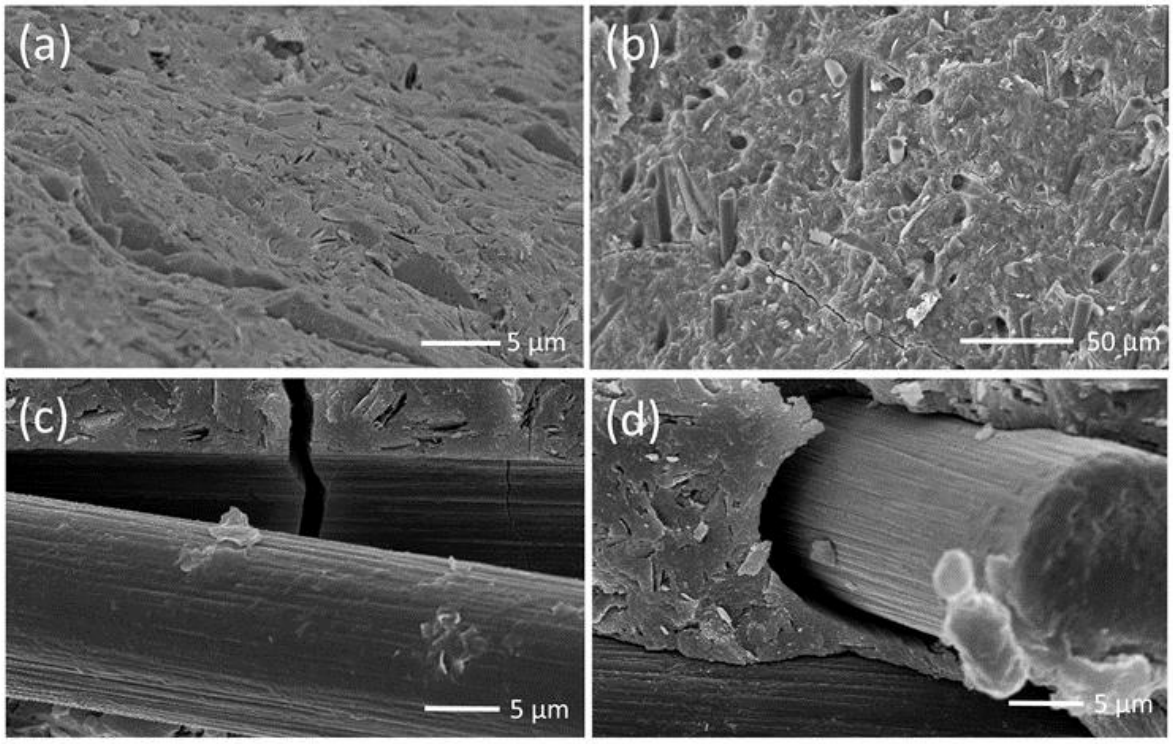

Fig. 2.2. SEM images of potassium geopolymer composites. (a) pure potassium geopolymer, (b) short carbon fiber reinforced, potassium geopolymer (c), (d) high magnifications of interface between a carbon fiber and geopolymer matrix.

Figs. 2.2 (a) and (b) show the microstructure of pure geopolymer with a fully reacted metakaolin phase and the fracture surface of C_f KGP, respectively. The carbon fibers were randomly oriented in geopolymer matrix according to Fig. 2.2 (b). The closer observation of a fiber and matrix was shown in Figs. 2.2 (c) and (d). The crack was deflected around the fiber during crack propagation rather than breaking the fibers. The striation of the carbon fiber was perfectly reproduced in the geopolymer matrix, which indicated that the geopolymers completely enclosed the carbon fibers by precipitating and polymerizing geopolymers on the surface of the carbon fibers. Moreover, Fig. 2.2 (d) shows the weak interfacial bonding between a carbon fiber and geopolymer matrix where the fiber was pulled out from the matrix. Thus, fiber pullout was concluded to be the main mechanisms of toughening of these composites in subsequent mechanical tests.

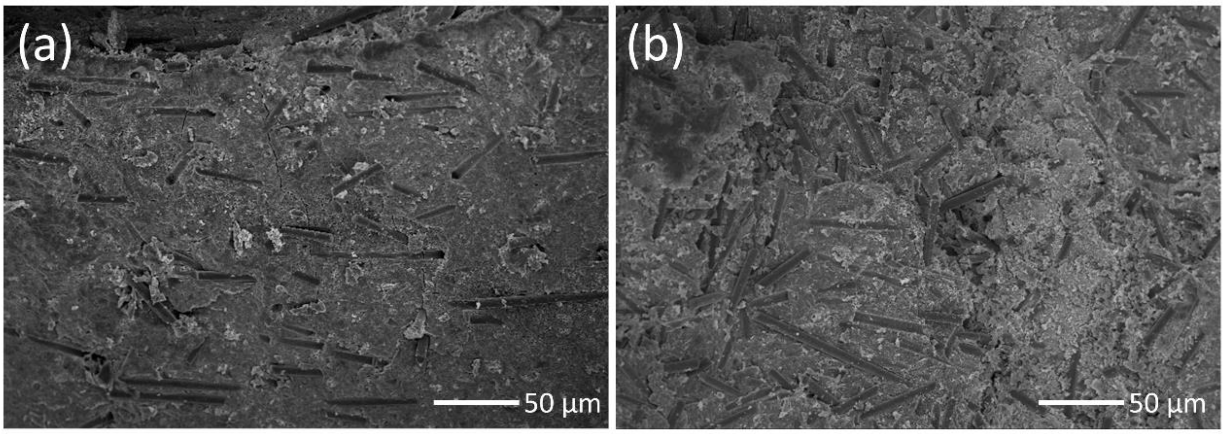

Fig. 2.3. SEM images of 5 (a) and 20 (b) wt% carbon fiber reinforced geopolymer composites.

The fracture surfaces of 5 and 20 wt% C_f KGP are seen in Figs. 2.3 (a) and (b), respectively. The short carbon fibers were randomly oriented in both 5 and 20 wt% fiber loadings. In the 5 wt% C_f KGP, the fibers were discrete and separately distributed. On the other hand, the fibers were agglomerated and entangled in 20 wt% C_f KGP as shown in Fig. 2.3 (b). Due to the lack of bonding between carbon fibers, the crack propagated along with the interface

of carbon fibers rather than between the carbon fiber and matrix. Therefore, the fiber pullout and crack deflection were not sufficiently established in the large of fiber content of 20 wt% in this case, which resulted in decreasing mechanical properties.

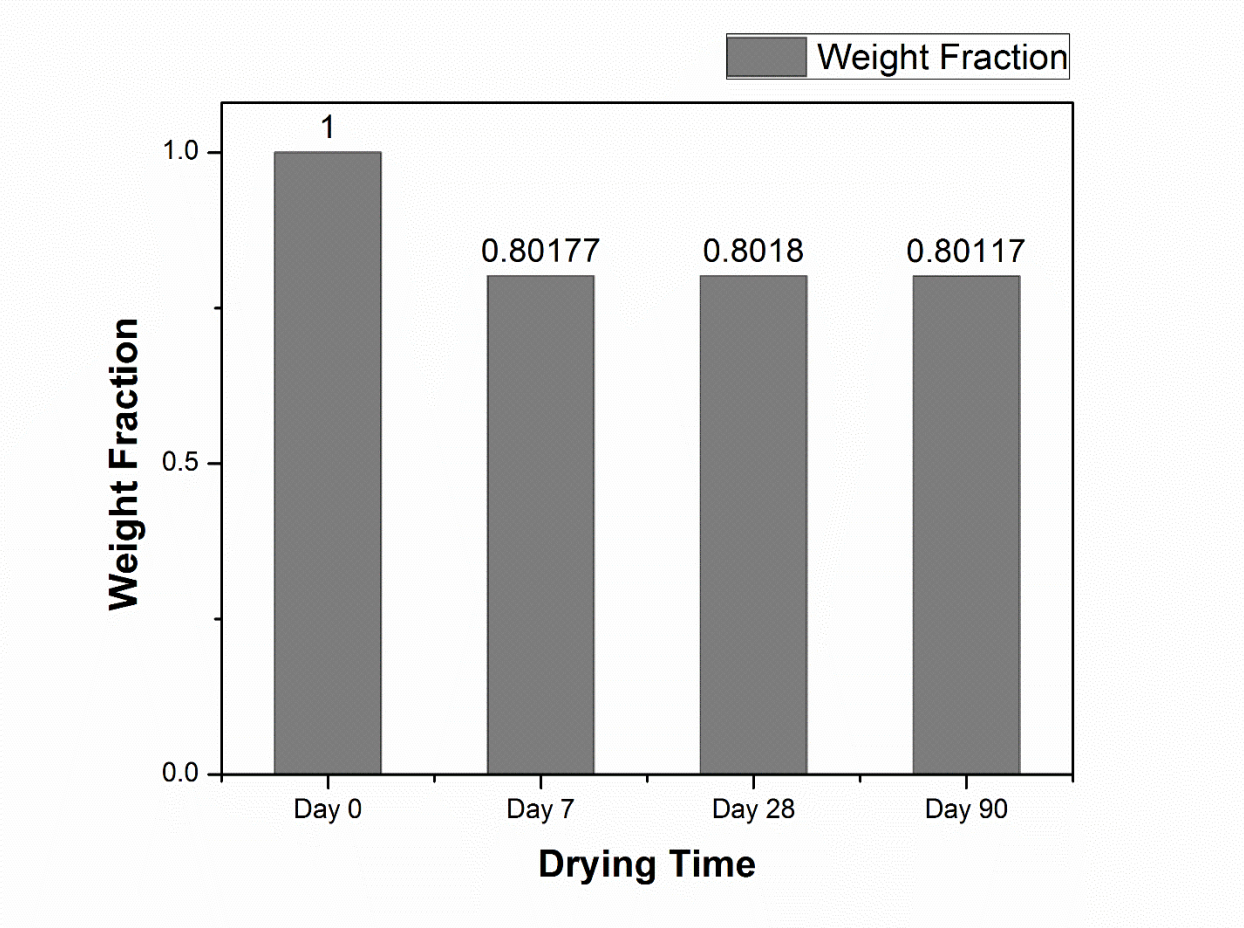

Fig. 2.4. Weight loss fraction of pure potassium geopolymer in a controlled humidity oven.

As shown in Fig. 2.4, the pure geopolymer lost weight over time upon exposure to air and it was fully dried to reach its steady state weight after 7 days. By drying samples under the same conditions, we could reduce the effect of remaining water in the geopolymer and measure consistent mechanical data.

b. Mechanical Properties

i. Flexural Testing

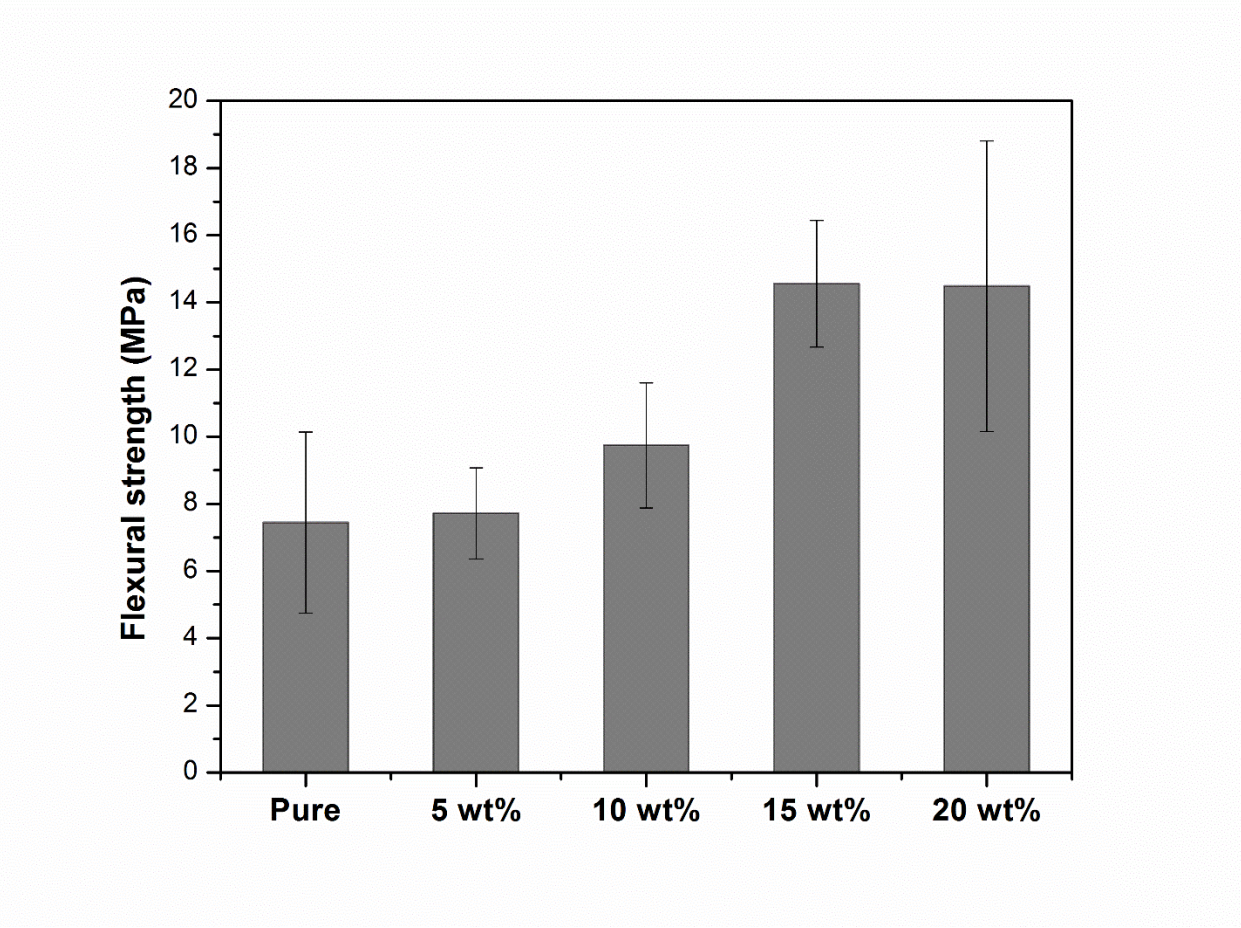

Fig. 2.5. Average four-point flexural strengths of geopolymer composites with different 60 µm carbon fiber loadings.

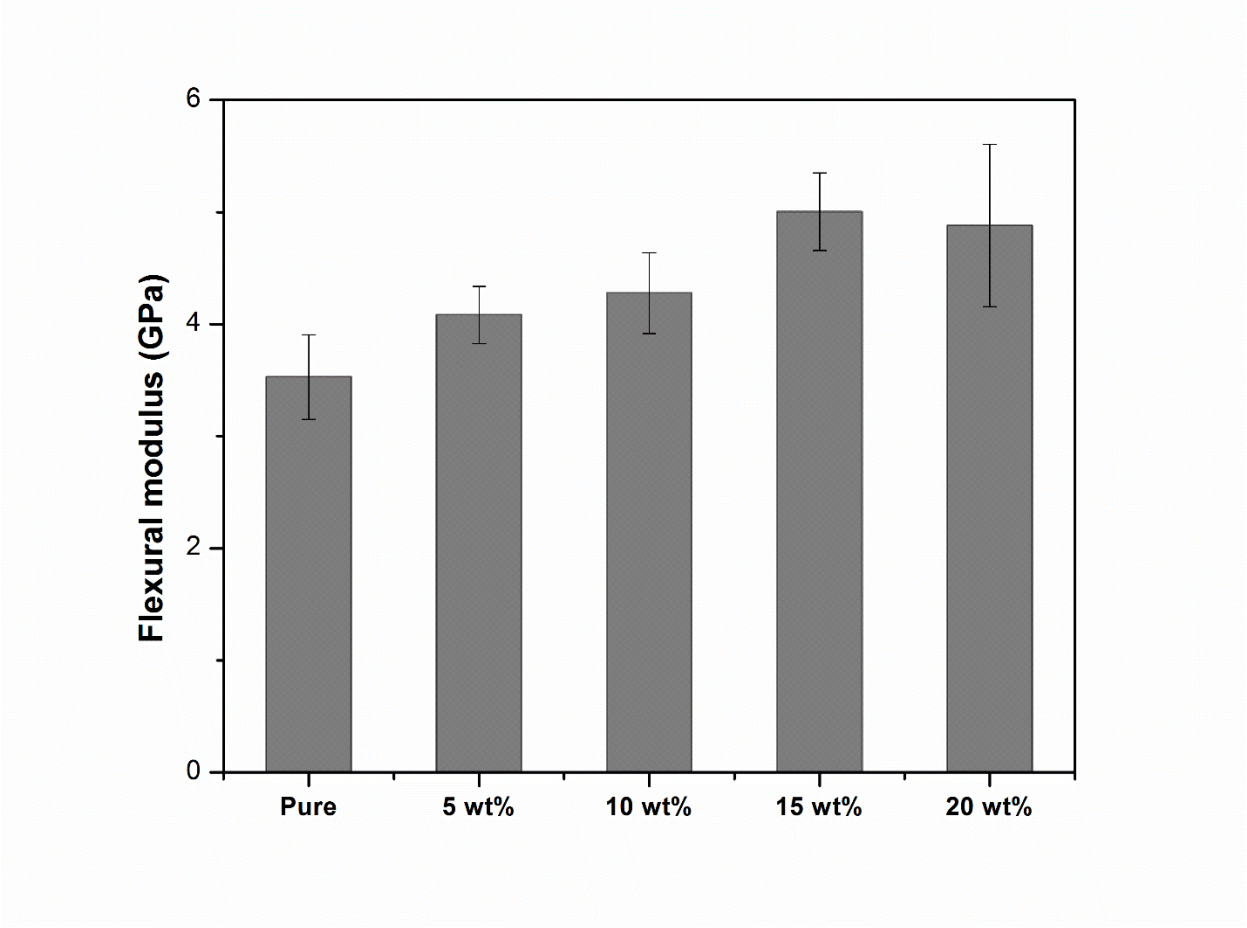

Fig. 2.6. Flexural modulus of geopolymer composites with 60 µm different carbon fiber loadings.

Both flexural strength and modulus increased as the fiber loading increased up to 15 wt% as shown in Figs. 2.5 and 2.6. Due to the lack of interfacial bonding, the main mechanism of strengthening in C_f KGP was fiber pullout. Thus, the greater the fiber concentration the more mechanical interfaces existed between the fiber and geopolymer matrix. This resulted in increasing the strength of composites. However, at a 20 wt% of carbon loading, both flexure strength and modulus decreased and the values scattered significantly, since too much carbon in the geopolymer slurry caused the following two problems. Firstly, a high loading of fiber had more chance of agglomeration with each other and slip would occur in between fibers rather than pulling out the fiber from the matrix. Secondly, the workability of a 20 wt% carbon loading

mixture decreased and the viscosity of the slurry increased significantly. This resulted in irremovable air traps inside the slurry during the molding process, thereby degrading the mechanical properties of C_f KGP.

ii. Weibull Statistics

Table 2.2. Weibull Moduli m and Characteristic Strengths α Measured from Four-Point Flexural Test

	Pure	5 wt%	10 wt%	15 wt%	20 wt%
m	10	30	18	23	17
σ_θ (MPa)	7.8	7.8	10	15	15

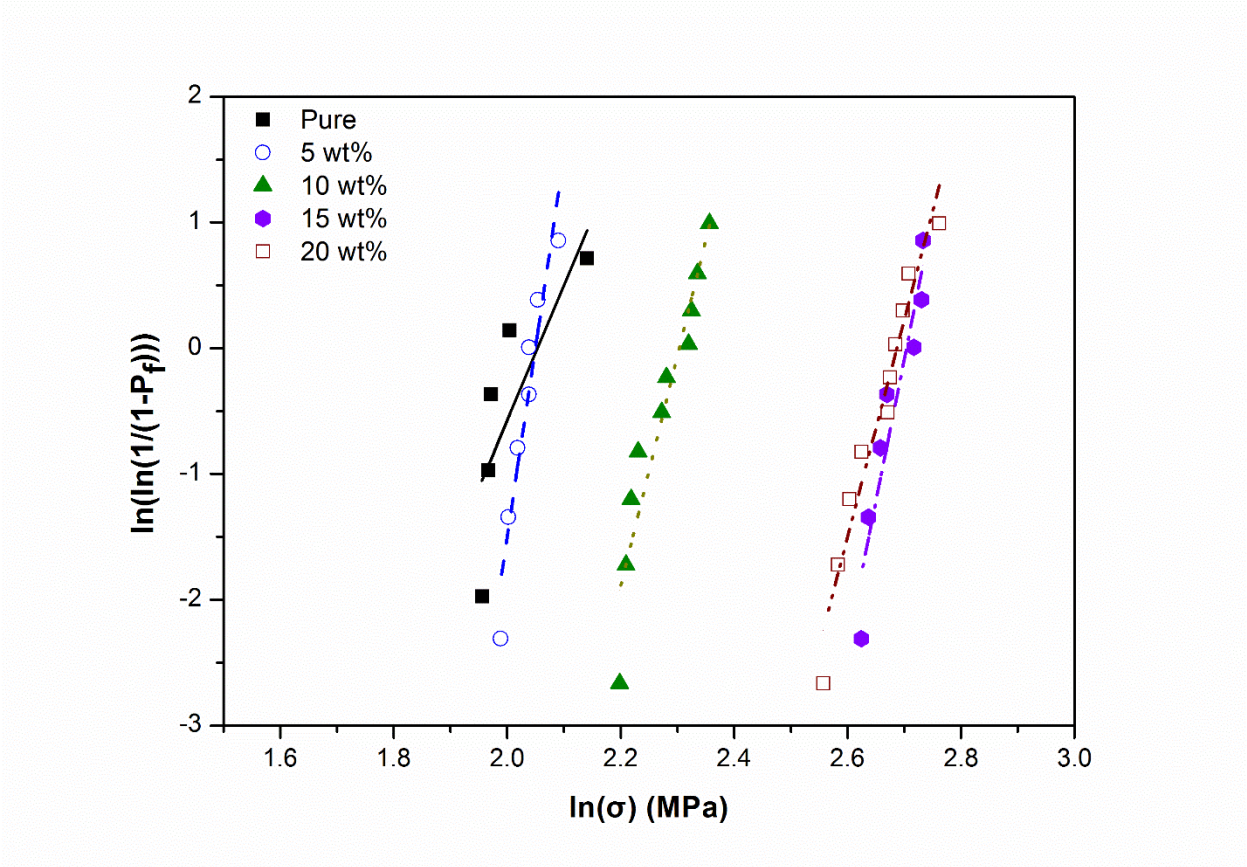

Fig. 2.7. Weibull moduli of 60 µm carbon fiber-reinforced geopolymer composites based on 4-point flexural strengths.

Fig. 2.7 and Table 2.2 summarize the Weibull moduli, m, and the characteristic flexure strengths, σ_θ, for 60 μm fiber-reinforced geopolymer composites. While Fig. 2.5 presents average flexural strengths of the composites, the characteristic strengths were based on Weibull statistics. The highest Weibull modulus, 30, was found at a 5 wt% of carbon loading with the same characteristic strength as pure potassium geopolymer, which indicated that the small addition of fibers significantly improved the Weibull modulus. The highest characteristic strength was 15 MPa at both 15 and 20 wt% C_f KGP but 15 wt% C_f KGP had a higher Weibull modulus, 23, than that of 20 wt% C_f KGP, 17. Considering both two-parameters, Weibull modulus and characteristic strength, the 15 wt% C_f KGP showed around twice higher Weibull modulus and characteristic strength than did pure KGP. As we expected from average flexural strengths, the Weibull modulus decreased at 20 wt% of carbon loading. In contrast to the average strength, the characteristic strength of 20 wt% C_f KGP remained the same as 15 wt%. However, the characteristic strength of 5 wt% of C_f KGP was slightly less (0.03) than the value for pure KGP. Such fracture behavior is usually observed as part of the rule of mixtures for unidirectional fiber-reinforced composites. Due to the buckling of fibers in compressive stress, the small amount of carbon fiber would behave as defects in the geopolymer matrix, so a lower strength was observed until the pullout mechanism dominated the entire facture behavior.

iii. Fracture Toughness

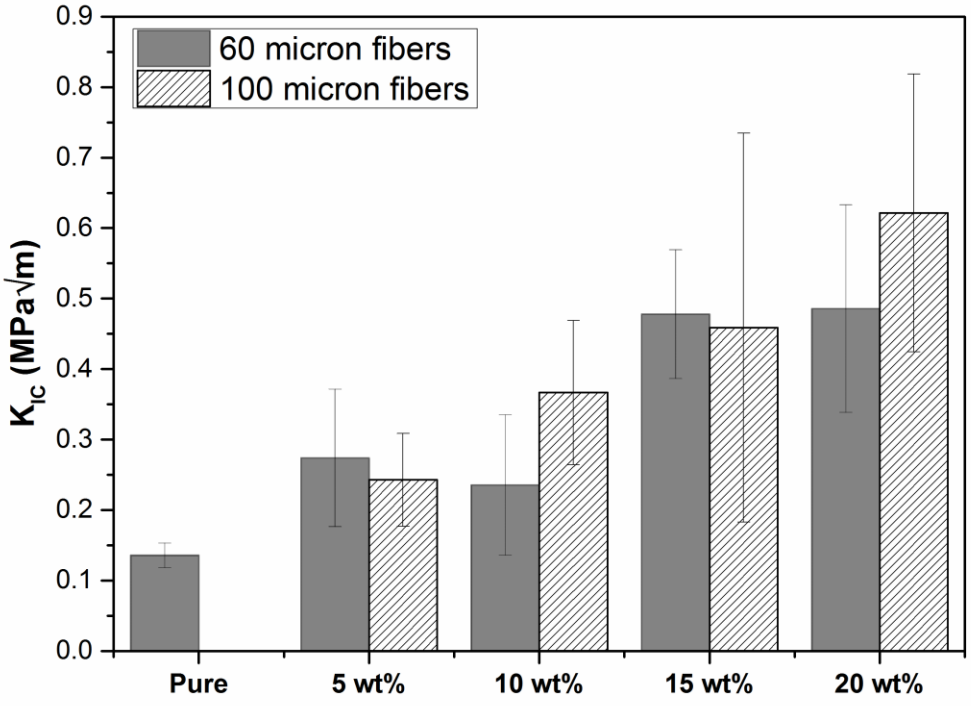

Fig. 2.8. The average SENB fracture toughness of two different fiber-reinforced geopolymer composites.

For the fracture toughness tests, we have used not only 60 µm long fibers but also 100 µm long milled fibers to investigate the effect of fiber length. As shown in Fig. 2.8, the toughness of C_f KGP increased with carbon loading, although 10 wt% of 60 µm fiber-reinforced C_f KGP had a 14.3% lower toughness than did the 5 wt%. More importantly, the toughness of 20 wt% of 60 µm C_f KGP did not improve and it scattered more than did the 15 wt% carbon fiber. As we discussed above, the high loading of carbon fibers resulted in decreased mechanical properties. Therefore, 15 wt% of 60 µm carbon fibers was the upper limit composition to achieve the highest and the most stable fracture toughness results. On the other hand, 15 and 20 wt% of

100 µm carbon fibers had significantly higher standard deviations which indicated a higher distribution of fracture toughness values. This could be attributed to the fact that longer fibers had more chance to agglomerate with each other than did the shorter fibers. In addition, at the same fiber loading, the viscosity of 100 µm carbon fiber reinforced geopolymer increased, so that the workability decreased significantly compared to the 60 µm long carbon fiber. The low workability of the slurry caused possible defects such as air entrapment and fiber agglomeration. Thus, the optimum carbon loading for 100 µm carbon fibers was 10 wt%, even though higher carbon loadings gave a higher fracture toughness. At the optimum carbon loadings for both 60 and 100 µm, the fracture toughness of C_f KGP increased by 3 and 2 times higher than for pure geopolymer, respectively.

iv. Hardness

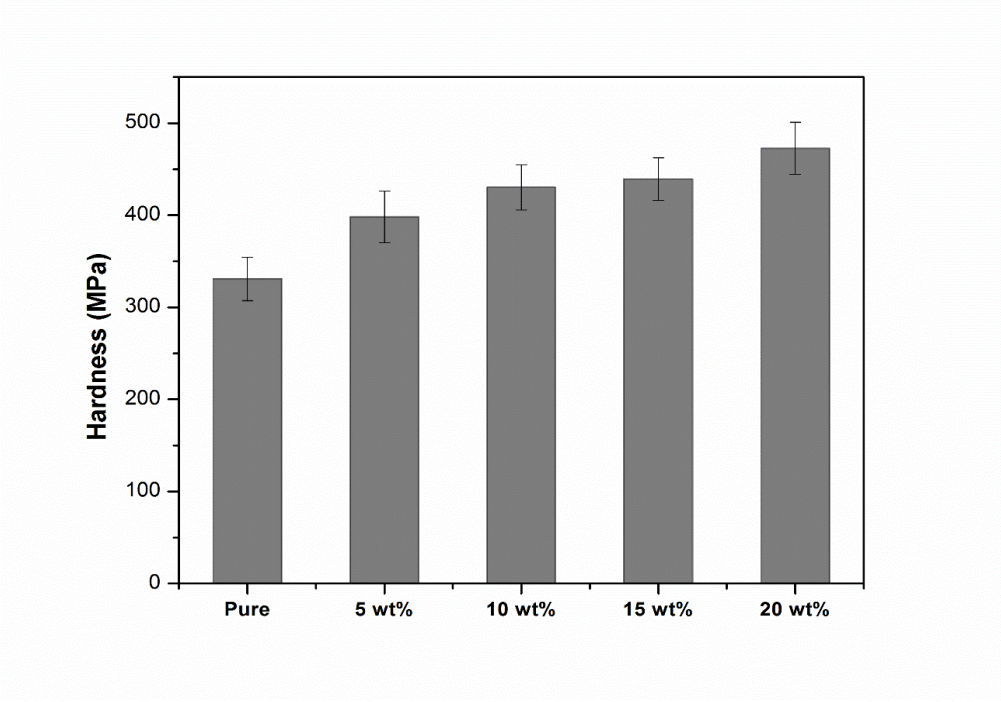

Fig. 2.9. The average hardness results of Vickers indentation of 60 µm milled carbon fiber-reinforced geopolymer.

The Vickers hardness increased as the carbon loading increased as shown in Fig. 2.9. The hardness of pure geopolymer was 331 ± 24 MPa and it increased up to 472 ± 28 MPa at 20 wt% carbon loading. This indicated that the hardness was improved by 44% when randomly oriented 20 wt% of carbon fibers were added to the geopolymer matrix.

2. 5 Conclusion and Discussion

This is benchmarking work to optimize the short carbon fiber loadings to geopolymer matrix in order to get the desired strength and toughness of composites. The micrographs of composites and several mechanical tests were conducted in this work. The details of stress-strain curves of C_f KGP in flexural test are shown in the supplementary information. The statistical analysis of flexure strengths was performed to calculate the Weibull moduli and characteristic strengths of C_f KGP.

The fracture mechanism of randomly-oriented, short carbon fiber-reinforced geopolymer occurred by fiber pullout due to the lack of fiber-matrix interfacial bonding. Increasing the amount of milled carbon fibers in potassium geopolymer matrix improved the mechanical properties. As a result, the flexure strength (15 ± 2 MPa), flexure modulus (5 ± 0.4 GPa), Weibull modulus (23), fracture toughness (0.5 ±0.1 MPa√m for 60 µm and 0.5 ± 0.3 MPa√m for 100 µm) and hardness (439 ± 23 MPa) increased with increasing fiber contents up to 15 wt%. However, 20 wt% carbon loading resulted in decreasing mechanical properties due to the air entrapments and fiber agglomerations. For 100 µm carbon fiber contents in the fracture toughness test, the optimum amount of fibers was 10 wt% which resulted in the most stable state and it still resulted in more than 2 times higher toughness (0.4 ± 0.1 MPa√m) than for pure geopolymer (0.1 ± 0.02 MPa√m) .

2. 6 Supplementary Information

This figure presents stress-strain curves of flexural tests. The stress-strain curves of pure potassium geopolymer and 15 wt% carbon fiber reinforced, potassium geopolymer were plotted in (a) and (b), respectively.

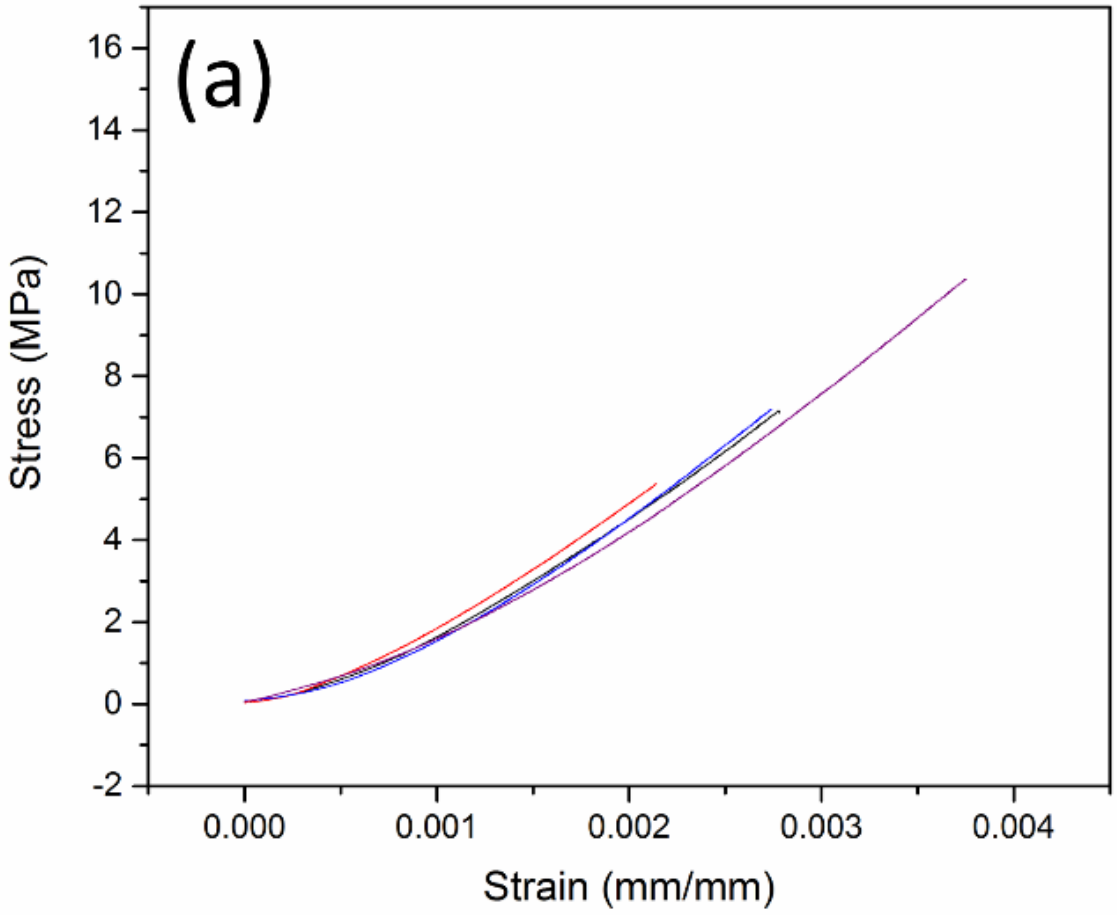

S.Fig. 2.1. Stress-strain curves of pure KGP (a) in flexural tests.

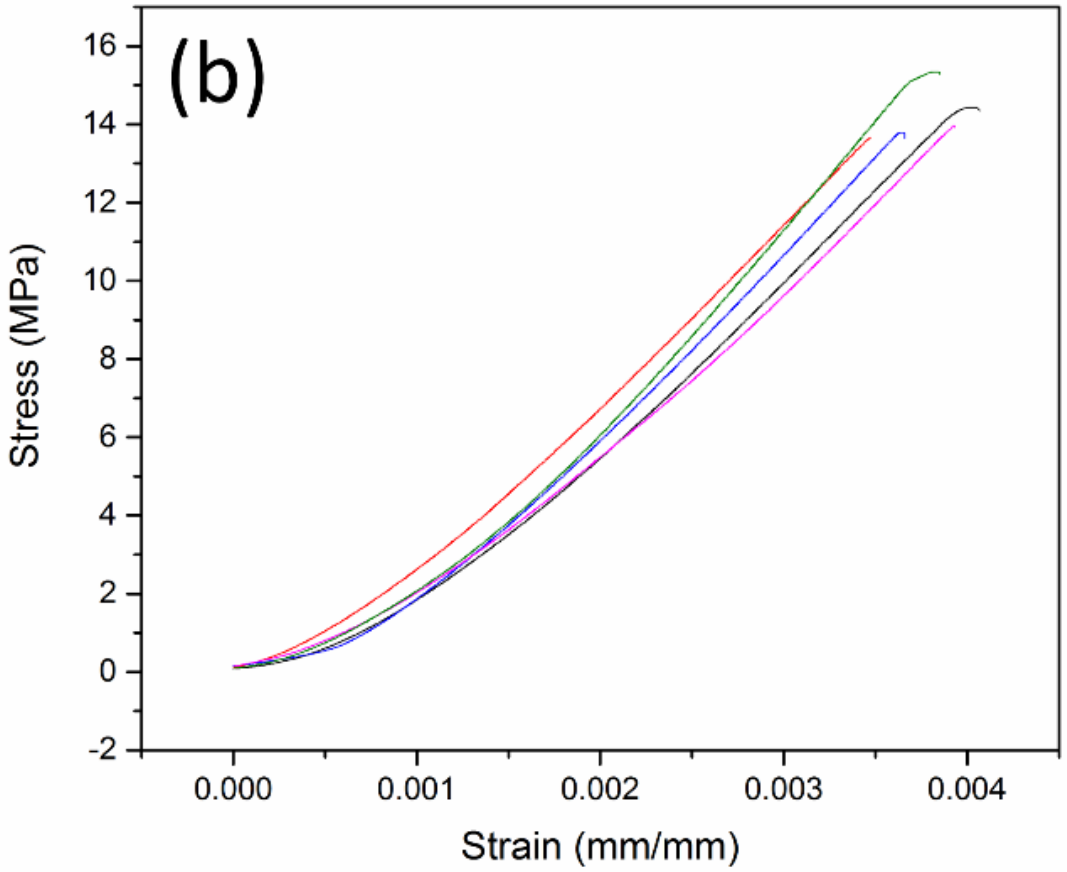

S.Fig. 2.1. (cont.) Stress-strain curves of 15 wt% C_f KGP (b) in flexural tests.

2. 7 References

1. J. Davidovits, "Geopolymers and Geopolymeric Materials," *J. Therm. Anal. Calorim.,* **35**[2] 429-41 (1989).

2. J. Davidovits, "Global Warming Impact on the Cement and Aggregates Industries," *World Resource Review,* **6**[2] 263-78 (1994).

3. P. Duxson, A. Fernández-Jiménez, J. L. Provis, G. C. Lukey, A. Palomo and J. Van Deventer, "Geopolymer Technology: The Current State of the Art," *J. Mater. Sci.,* **42**[9] 2917-33 (2007).

4. J. Davidovits, "Geopolymers - Inorganic Polymeric New Materials," *J. Therm. Anal.,* **37**[8] 1633-56 (1991).

5. J. G. S. Van Jaarsveld, J. S. J. Van Deventer and G. C. Lukey, "The Effect of Composition and Temperature on the Properties of Fly Ash- and Kaolinite-Based Geopolymers," *Chem. Eng. J.,* **89**[1-3] 63-73 (2002).

6. P. Duxson, J. L. Provis, G. C. Lukey, S. W. Mallicoat, W. M. Kriven and J. S. J. Van Deventer, "Understanding the Relationship between Geopolymer Composition, Microstructure and Mechanical Properties," *Colloids Surf., A,* **269**[1-3] 47-58 (2005).

7. W. M. Kriven, J. L. Bell and M. Gordon, "Microstructure and Nanoporosity of as-Set Geopolymers,*" CeramicTranscation* **27** 491-503 (2003).

8. S. Wallah and B. V. Rangan, "Low Calcium Fly Ash Based Geopolymer Concrete–Long Term Properties," *Res. Report-GC2, Curtin University, Australia. pp* 76-80 (2006).

9. P. Duxson, J. L. Provis, G. C. Lukey and J. S. J. van Deventer, "The Role of Inorganic Polymer Technology in the Development of 'Green Concrete'," *Cem. Concr. Res.,* **37**[12] 1590-97 (2007).

10. W. M. Kriven, J. L. Bell and M. Gordon, "Microstructure and Microchemistry of Fully-Reacted Geopolymers and Geopolymer Matrix Composites," *Advances in Ceramic Matrix Composites IX,* **153** 227-50 (2003).

11. J. L. Bell, P. Sarin, P. E. Driemeyer, R. P. Haggerty, P. J. Chupas and W. M. Kriven, "X-Ray Pair Distribution Function Analysis of a Metakaolin-Based, Kalsi 2 O 6· 5.5 H 2 O Inorganic Polymer (Geopolymer)," *J. Mater. Chem.,* **18**[48] 5974-81 (2008).

12. J. L. Bell, P. Sarin, J. L. Provis, R. P. Haggerty, P. E. Driemeyer, P. J. Chupas, J. S. van Deventer and W. M. Kriven, "Atomic Structure of a Cesium Aluminosilicate Geopolymer: A Pair Distribution Function Study," *Chem. Mater.,* **20**[14] 4768-76 (2008).

13. W. M. Kriven and J. L. Bell, "Effect of Alkali Choice on Geopolymer Properties," in 28th International Conference on Advanced Ceramics and Composites B: Ceramic Engineering and Science Proceedings. Vol. **25**.

14. J. L. Bell, P. E. Driemeyer and W. M. Kriven, "Formation of Ceramics from Metakaolin-Based Geopolymers: Part I—Cs-Based Geopolymer," *J. Am. Ceram. Soc.,* **92**[1] 1-8 (2009).

15. J. L. Bell, P. E. Driemeyer and W. M. Kriven, "Formation of Ceramics from Metakaolin-Based Geopolymers. Part II: K-Based Geopolymer," *J. Am. Ceram. Soc.,* **92**[3] 607-15 (2009).

16. D. P. Dias and C. Thaumaturgo, "Fracture Toughness of Geopolymeric Concretes Reinforced with Basalt Fibers," *Cem. Concr. Compos.,* **27**[1] 49-54 (2005).

17. W. Li and J. Xu, "Mechanical Properties of Basalt Fiber Reinforced Geopolymeric Concrete under Impact Loading," *Mater. Sci. Eng., A,* **505**[1-2] 178-86 (2009).

18. Z. Yunsheng, S. Wei and L. Zongjin, "Impact Behavior and Microstructural Characteristics of Pva Fiber Reinforced Fly Ash-Geopolymer Boards Prepared by Extrusion Technique," *J. Mater. Sci.,* **41**[10] 2787-94 (2006).

19. Z. H. Zhang, X. Yao, H. J. Zhu, S. D. Hua and Y. Chen, "Preparation and Mechanical Properties of Polypropylene Fiber Reinforced Calcined Kaolin-Fly Ash Based Geopolymer," *Journal of Central South University of Technology (English Edition),* **16**[1] 49-52 (2009).

20. S. S. Musil, P. F. Keane and W. M. Kriven, "Green Composite: Sodium-Based Geopolymer Reinforced with Chemically Extracted Corn Husk Fibers," *Cer. Sci. and Eng. Proc.,* **34**[10] 123-33 (2013).

21. K. Sankar and W. M. Kriven, "Sodium Geopolymer Reinforced with Jute Weave," *Cer. Sci. and Eng. Proc.,* **38**[10] 39-60 (2014).

22. K. Sankar and W. M. Kriven, "Potassium Geopolymer Reinforced with Alkali-Treated Fique," *Cer. Sci. and Eng. Proc.,* **38**[10] 61-78 (2014).

23. K. Sankar, R. K. Vieira and W. M. Kriven, "Green Composite: Sodium Geopolymer Reinforced with Malva Fibers," *J. Am. Ceram. Soc.* Submitted (2015).

24. U. Heo, K. Sankar, S. S. Musil and W. M. Kriven, "Rice Husk Ash as a Silica Source in Geopolymer Formulation," *Cer. Sci. and Eng. Proc.,* **38**[10] 87-102 (2014).

25. T. Alomayri, F. Shaikh and I. Low, "Characterisation of Cotton Fibre-Reinforced Geopolymer Composites," *Composites Part B,* **50** 1-6 (2013).

26. T. Lin, D. Jia, P. He, M. Wang and D. Liang, "Effects of Fiber Length on Mechanical Properties and Fracture Behavior of Short Carbon Fiber Reinforced Geopolymer Matrix Composites," *Materials Science and Engineering: A,* **497**[1] 181-85 (2008).

27. T. Lin, D. Jia, M. Wang, P. He and D. Liang, "Effects of Fibre Content on Mechanical Properties and Fracture Behaviour of Short Carbon Fibre Reinforced Geopolymer Matrix Composites," *Bull. Mater. Sci.,* **32**[1] 77-81 (2009).

28. ASTM, "Standard Test Methods for Flexural Strength of Concrete." in West Conshohocken: ASTM International, Vol. **C78-09** (2009).

29. ASTM, "Standard Test Methods for Plane-Strain Fracture Toughness and Strain Energy Release Rate of Plastic Materials." in West Conshohocken: ASTM International, Vol. **D5045-96** (1999).

30. ASTM, "Standard Practice for Reporting Uniaxial Strength Data Estimating Weibull Distribution Parameters for Advance Ceramics." in West Conshohocken: ASTM International, Vol. **C1239-13** (2001).

CHAPTER 3: SHORT CARBON FIBER-REINFORCED, GEOPOLYMER COMPOSITES

PART II. EFFECT OF FIBER LENGTH ON MECHANICAL PROPERTIES

3. 1 Abstract

Short carbon fiber (60 µm and 100 µm) reinforced potassium geopolymer, C_f KGP, with different fiber contents (5, 10, 15, and 20 wt%) were prepared and their various mechanical properties such as Young's modulus, shear modulus, Poisson's ratio, uniaxial compressive strength and biaxial tensile strength, were measured by impulse excitation (IE), resonant ultrasound spectroscopy (RUS), compression, and Ring on Ring (ROR) methods. The various theoretical models were compared to the measured moduli and the Weibull statistical analysis was applied to the results of compressive strengths. The results showed that the Young's and shear moduli increased as the fiber content increased. The 5 wt% of 60 µm C_f KGP and 10 wt% of 100 µm C_f KGP achieved the most reliable uniaxial compressive strengths of 90 and 80 MPa, respectively. Linear increments of biaxial tensile strength were observed for both fibers. The longer 100 µm fiber improved the biaxial strength by 30% at 20 wt% C_f KGP.

3. 2 Introduction

Fiber reinforced geopolymer composites could be used in structural applications, such as bridge and building blocks.[1] The use of fiber reinforced geopolymer composites can be extended to design various energy absorbers. The fracture mechanism of fiber reinforced composites, deflection of crack propagation, improved the energy absorption in quasi static fracture as shown in the previous paper.[2] Moreover, the geopolymer composites can be applied to absorb mechanical energy under high impact and high strain rates.[3] Basalt fiber reinforced geopolymer composites improved their deformation and energy absorption at high strain rates.[3]

Another rising field of energy absorption systems is granular media in an acoustic metamaterial. Due to the strongly nonlinear behavior of granular media, a stress wave consumes energy in propagating throughout individual grains.[4] This new class of acoustic metamaterials with ordered granular arrays has been studied by many researchers in one- and two- dimensional structures. Energy localization or redirection was designed by using strongly nonlinear granular media to mitigate and tailor energy propagation.[4, 5, 6, 7, 8, 9, 10] Unsupported granular media have been designed so far, in order to study their intrinsic dynamics in theory and experiments. However, for practical applications such as an acoustic metamaterial, a supporting medium or matrix is required in which to embed ordered granular bead arrays.

One of the significant advantages of short carbon fiber-reinforced geopolymer composites, unlike other ceramic composites, is that liquid based geopolymers can be formed at low temperatures into any complicated shape. Exploiting the advantage in processing of geopolymer composites broadens the possible applications to support granular acoustic metamaterials in one- two- and even three- dimensions. Polydimethylsiloxane (PDMS) was used as a matrix to hold 2D arrays of stainless beads which showed energy transfer between two

chains.[11] PDMS, polyethylene (PE) and geopolymer have been used as matrix materials for ordered granular media in order to investigate acoustic bands and propagating breathers.[12]

In order to extend the use of geopolymer composites and analyze the effect of a matrix as well as its dynamic behavior, the mechanical properties of carbon fiber-reinforced geopolymer composites should be investigated comprehensively. The effect of fiber length in random orientation on mechanical properties has been investigated in this study. The elastic modulus of geopolymer has not been fully understood since tensile testing of brittle geopolymer is limited. Researchers have used different techniques to measure the elastic modulus of brittle materials, including impulse excitation (IE) and resonant ultrasound spectroscopy (RUS).[13] Furthermore, various theoretical models have been established in past decades to predict the elastic modulus of fiber reinforced composites. In our study, the IE and RUS method were applied to measure the dynamic properties of geopolymer composites and to compare the experimental results with theoretical predictions. In addition to the mechanical properties, the uniaxial and biaxial tensile strengths have been studied by traditional compression and ring on ring tests, respectively. The effect of fiber length on strengths was investigated using statistical analysis and Weibull moduli.

3. 3 Experimental Procedures

a. Fiber Characteristics and Composite Processing

Milled, short carbon fibers from Toho Tenax® (Toho Tenax America, Inc., Rockwood, TN) were added to potassium geopolymer having the chemical formula $K_2O \cdot Al_2O_3 \cdot 4SiO_2 \cdot 11H_2O$. The properties of the fibers such as density, Young's modulus, tensile strength, and electrical resistivity were 1.82 g/cm^3, 225 GPa, 4.3 GPa, 1.4 mmΩ-cm, respectively. Moreover, the average fiber diameter was 7 µm, which resulted in the aspect ratios of 9:1 and 14:1 for 60 and 100 µm fibers, respectively. These high aspect ratios could provide sufficient mechanical reinforcement and electrical conductivity to produce a useful geopolymer composite material. In this study, we focused mainly on the effect of fiber lengths on the dynamic and static mechanical properties of carbon fiber-reinforced, potassium geopolymers, C_f KGP. The preparation of potassium geopolymer and fiber mixing procedures have been described in our previous work.[2] Once the mixtures of fibers and geopolymer were ready, we poured the mixtures into a Delrin® mold to make various samples for different tests. The C_f KGP was cured in 50℃ for 24 hours and then dried in a humidity controlled chamber (1000H Series Temperature/Humidity Chamber, Test Equity, Moorpark, CA) at 20℃ at 30% relative humidity for 7 days.[2]

b. Dynamic Mechanical Testing

i. Impulse Excitation

Elastic moduli and acoustic wave speeds of a specimen are a function of the specimen geometry, dimensions, mass density and the resonance frequencies.[14] The impulse excitation (IE) method (Buzz-o-Sonic, BuzzMac, WI) was used to investigate the dynamic properties of C_f KGP, by following the ASTM 1876-07 guideline.[15] The IE test is a nondestructive method to

measure the Young's modulus, shear modulus, wave speeds and Poisson's ratio of materials, based on the natural frequency, dimensions and mass of test pieces. The natural frequency was determined by measuring and analyzing the vibration response of the samples from impulse excitation, generated by tapping with a small hammer. A microphone was used to detect the vibrations in this study.

The dimensions of the specimen were determined to be a 25 (w) x 2.5 (t) x 100 (L) mm rectangular plate, satisfying the required dimensional constraints, $10 \geq w/t \geq 5$, $L/t \geq 20$, as specified in the ASTM standard (ASTM 1876-07), in order to simplify the mathematical equations and to reduce the possible errors during measurement. The elastic moduli, shear moduli, and sound velocities of C_f KGP were measured by IE and then compared to the resonant ultrasound spectroscopy (RUS) test results as well as with various theoretical models.

ii. Resonant Ultrasound Spectroscopy

In resonant ultrasound spectroscopy (RUS), a specimen of known geometry, dimensions and mass is excited across a range of frequencies, and the mechanical response is recorded. For the bar shaped specimens in this study, the specimens were excited from 1 kHz to 320 kHz in 29,999 steps. A resonance frequency is exhibited as a sharp peak in intensity of the mechanical response at the driven frequency. Commercial software (RPModel version 2.68b, Quasar International, Albuquerque, NM) was used to fit the measured resonance frequencies, mass and dimensions to determine the elastic moduli and the acoustic wave speeds for each specimen type. Additional details of the RUS technique[16, 17, 18] and error determination[16] have been published elsewhere.

The RUS specimens in this study were bar-shaped of nominal dimensions 25 mm × 12 mm × 3 mm. Due to difficulties in analysis of some specimens, possibly caused by edge flaws

such as large pores or chips, the specimens of geopolymer with additions of 10 wt%, 15 wt% and 20 wt% 100 µm carbon fiber additions were affixed to a right-angle-machined block and then cut down and sanded with 600 grit sand paper to final dimensions of approximately 12 mm × 10 mm × 3 mm.

iii. Theoretical Models

Many micromechanical theories and models have been studied to predict the stiffness and strength of fiber reinforced composites.[19, 20, 21, 22, 23, 24, 25] Most of the models have been investigated for unidirectional and continuous composites but not for our short carbon fibers. This study mainly focused on the theories and models for randomly oriented short fiber composites and compared them with the experimental results from IE and RUS testing. The applicable theories for randomness and three-dimensionality are shown in Table 3.1.[25]

Table 3.1. Various Theories of Randomly Oriented Short Fiber Reinforcements

Theory	Elastic modulus	Shear modulus
Christensen[20]	$\frac{V_f}{6}E_f + [1 + (1 + v_m)V_f]E_m$	N/A
Manera[22]	$\left(\frac{2}{15}E_f + \frac{3}{4}E_m\right)V_f + \frac{1}{3}E_m$	N/A
Curtis[23]	$x_1 x_2 E_f V_f + E_m V_m$	N/A
Pan[25]	$\frac{V_f}{2\pi}E_f + \left(1 - \frac{V_f}{2\pi}\right)E_m$	$\frac{E_c}{2(1+v_c)}, v_c = \frac{V_f}{2\pi}v_f + \left(1 - \frac{V_f}{2\pi}\right)v_m$
Modified Halpin-Tsai[26, 27] with constant shape factor	$E = \frac{1 + c\eta V_f}{1 - \eta V_f}E_m, \eta = \frac{\left(\frac{\alpha E_f}{E_m}\right) - 1}{\left(\frac{\alpha E_f}{E_m}\right) + c}$	N/A

where, V_f and V_m are the volume fraction of fiber and matrix,

E_f, E_m, and E_c are the elastic moduli of fiber, matrix and composite,

$x_1 = 0.2$, $x_2 = 1 - \tanh(ns) / ns$, s = the fiber aspect ratio,

$n^2 = 2E_m / [E_f (1+\nu_m) \ln(P_f / V_f)]$,

P_f = the fiber packing factor, 0.82

ν_f and ν_m are the Poisson's ratio of the fiber and matrix.

$\alpha = 1/6$, $c = 2(\lambda/d)$, λ = the length of fiber, d = the diameter of fiber

Since the original Halpin-Tsai[19, 21] model applied to unidirectional reinforced composites, the modified Halpin-Tsai[26, 27] model was used to predict the moduli. Three dimensional randomness of fiber orientations and aspect ratio of fibers were accounted in the modified Halpin-Tsai[26, 27] model. For the shear modulus, the three dimensional orientation of fibers was not considered in the Christensen[20], Manera[22], Curtis[23] and modified Halpin-Tsai[26, 27] models. However, the Pan[25] model estimated the Poisson's ratio in three dimensions and calculated the shear modulus based on the value of the Young's modulus.

c. Static Mechanical Testing

i. Compressive Test

Compression tests determine the behavior of materials under uniaxial compressive loads. According to ASTM C1424-10, the specimen should be of a 3 (D) x 6 (H) mm cylindrical shape.[28] For construction materials, compressive strength is the most common performance measurement to meet the design requirements of a structure. The compressive tests were performed on an Instron Universal Testing Frame, using a silicon carbide fixture mounted on an alumina push rod. Based on the specimen dimensions, the speed of the cross-head was

determined as 0.5 mm/min, in order to maintain the strain rate of 1 x 10^{-4} mm/mm. In order to study the Weibull distribution, more than 20 specimens were prepared for each composition and tested at room temperature.

ii. Ring on Ring Test

Fracture strength was measured by the ring on ring (ROR) method, as detailed in ASTM 1499-09 [C1499-09 2009].[29] The ROR fixture had a support ring diameter, D_S, of 20 mm and a loading ring diameter, D_L, of 10 mm. The specimens were disk-shaped, nominally of diameter D = 30 mm and thickness h = 3 mm. The specimen thickness, h, was chosen partly based on the support ring diameter, D_S, where $D_s/10 \geq h$, but due to the inherently weak materials in this study, a thicker specimen h was chosen.

The ROR test was performed in air on specimens produced by curing in a mold and having final specimen dimensions which were consistent with the customary practices for producing the materials for this study. Per the ASTM standard, a compliant layer of 1 mm sheet silicone was placed between the specimen and the support ring to limit line or point contact stresses or friction. To aid in fracture analysis, an adhesive-backed dot of polytetrafluoroethylene (PTFE) film of diameter 25.4 mm (15-2HD-D-1-TF, CS Hyde Co, Lake Villa, IL) was placed on the compressive face of each specimen. A displacement rate of 1 mm/min was used during testing. Fracture strength, σ_f, was calculated per the ASTM standard by Eq. (3.1).

$$\sigma_f = \frac{3F}{2\pi h^2}\left[(1-v)\frac{D_S^2 - D_L^2}{2D^2} + (1+v)\,ln\left(\frac{D_S}{D_L}\right)\right] \quad (3.1)$$

where, F is the breaking load, D is the specimen diameter, and v is the average Poisson's ratio from RUS analysis of 1 to 5 bar shaped samples of the same material. Additional details about the ROR fixture, testing methodology and equipment are available elsewhere.[30 31 32, 33]

iii. Statistical Analysis

Due to the presence of random defects, the average fracture strengths were insufficient to show the behavior of the brittle materials. Weibull statistical analyses of fracture results determined the reliability of geopolymer composites.[2] The Weibull modulus, m, is a dimensionless parameter of the Weibull distribution and it indicates the consistency of failure of brittle materials. In order to examine the Weibull moduli of compressive tests and ring on ring tests, more than 20 specimens were tested for each composition and a regression analysis was performed within 95% confidential interval of tested specimens.

3. 4 Results

a. Microstructures

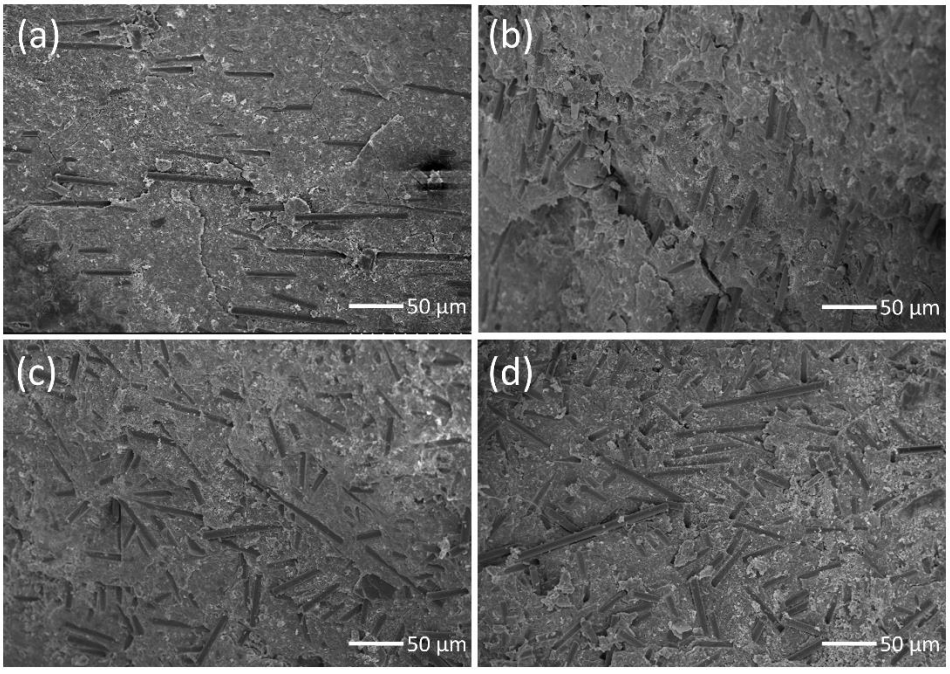

Fig. 3.1. Fracture surfaces of carbon fiber reinforced, potassium geopolymers.

The fully reacted metakaolin phase and the fracture surface of C_f KGP were studied in our previous work.[2] The short fibers were randomly oriented and no interfacial bonding was observed between the carbon fiber and potassium geopolymer matrix. Earlier work indicated that the main mechanisms of strengthening and toughening were fiber pullout. In addition, the SEM micrographs of facture surfaces are illustrated in the Fig. 3.1. The 5, 10, 15 and 20 wt% carbon fibers reinforced, potassium geopolymers were shown in Fig. 3.1 (a), (b), (c) and (d), respectively. Carbon fibers were randomly oriented and enclosed by geopolymer matrix. However, the various fiber loadings showed the different microstructures, particularly distribution of the fibers. More distributed fibers were observed in 5 wt% fiber loadings and fibers were agglomerated in 20 wt% fiber loadings, as shown in Figs. 3.1 (a) and (d), respectively.

b. Dynamics Mechanical Properties

The IE and RUS experimental results for the 60 and 100 µm C_f KGP specimens (Table 3.2) and a comparison to six theoretical models for the elastic moduli of composite systems (Table 3.1) are summarized in Figs. 3.2 and 3.3.

Table 3.2. The Measured Young's Modulus, Shear Modulus and Poisson's Ratio of Carbon Fiber Reinforced Geopolymer Composites

Volume Fraction	IE test						RUS test					
	E (GPa)		G (GPa)		ν		E (GPa)		G (GPa)		ν	
V_f	60 (µm)	100 (µm)	60 (µm)	100 (µm)	60 (µm)	100 (µm)	60 (µm)	100 (µm)	60 (µm)	100 (µm)	60 (µm)	100 (µm)
0	8.07	8.07	3.36	3.36	0.20	0.20	8.28	8.28	3.61	3.61	0.15	0.15
0.039	10.50	11.05	4.12	4.17	0.27	0.33	9.36	9.72	4.16	3.87	0.13	0.25
0.079	14.00	14.19	4.60	4.79	0.52	0.48	9.99	11.18	4.06	4.44	0.23	0.26
0.120	15.72	15.77	5.22	5.35	0.51	0.47	12.57	11.13	4.80	4.50	0.31	0.24
0.161	17.69	16.73	5.71	5.79	0.55	0.45	12.96	13.78	5.37	5.32	0.21	0.3

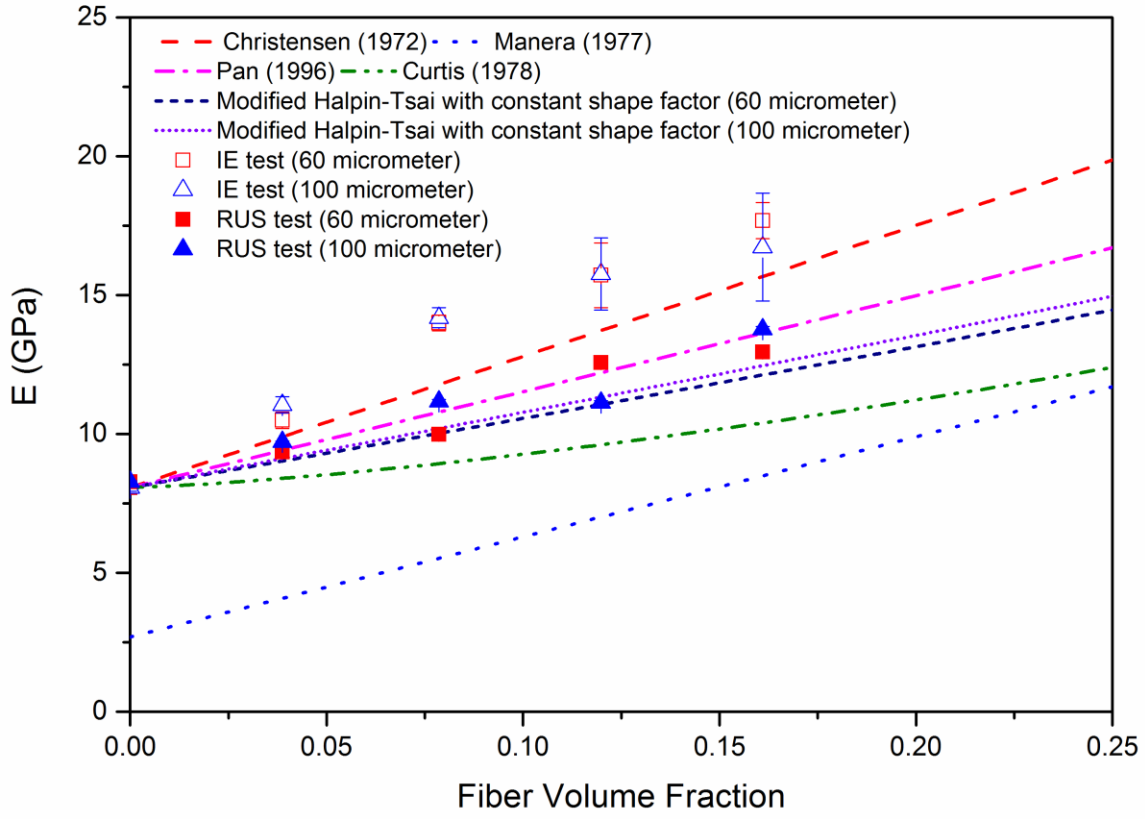

Fig. 3.2. Elastic moduli comparison between theories and experimental results of C_f KGP based on the IE and RUS tests.

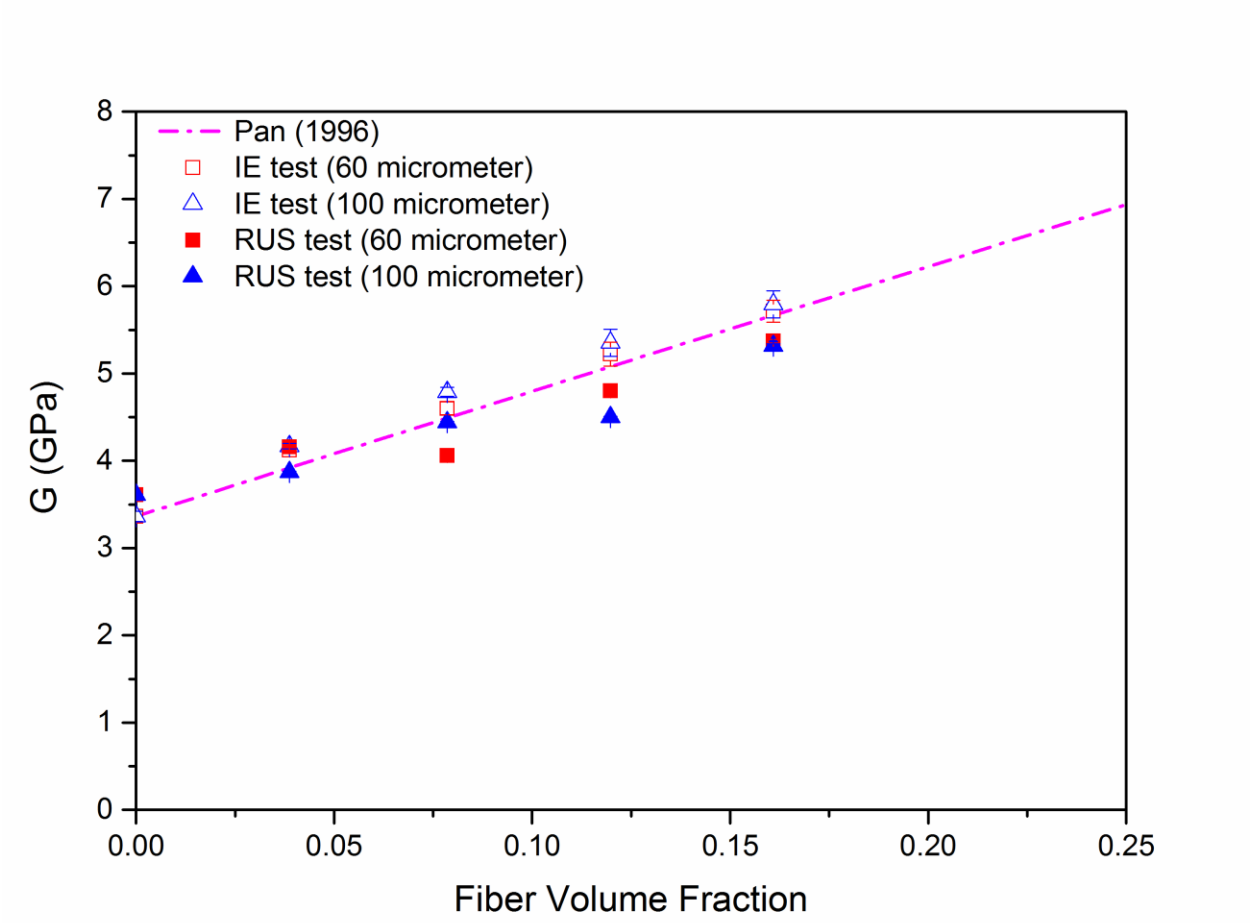

Fig. 3.3. Shear moduli comparison between theories and experimental results of C_f KGP based on the IE and RUS tests.

In order to compare the experimental results with the theoretically predicted elastic moduli, the fiber weight percentages were converted to volume percentages. Hence, the 5, 10, 15 and 20 wt% of fibers correspond to 0.039, 0.079, 0.120 and 0.161 volume factions of fibers, respectively. In Figs. 3.2 and 3.3, the square and triangular plotting symbols indicate the 60 and 100 µm C_f KGP specimens, respectively. For the two different experimental test techniques, the empty and filled symbols designate the IE and RUS tests results, respectively. With increasing fiber content the Young's and shear moduli of C_f KGP increased (Figs. 3.2 and 3.3) since the elastic modulus of carbon fibers (250 GPa) was much higher than that of the pure geopolymers

(7.74 GPa). For example, the Young's modulus the 60 μm specimens measured by the IE technique increased by more than a factor of two, from 8.07 to 17.69 GPa as the fiber volume fraction increased from 0 to 0.161 (Table 3.2).

For the Young's modulus, the predictions from the Manera[22] and Curtis[23] models (Table 3.1) fall well below the experimental data from both the IE and RUS measurements on all specimens included in this study (Fig. 3.2). For the RUS measurements, the experimental E values agreed well with the theoretically predicted E values from the Modified Halpin-Tsai[27, 28] and the Pan[25] models (Fig. 3.2). The theoretically predicted E values from the Christensen[20] model, steadily diverged from the experimental E results from RUS as the fiber volume fraction increased although for the experimentally determined E values from the IE technique exceed the theoretically predicted E from the Christensen[21] model (Fig. 3.2).

For the shear modulus, the theoretically predicted values from the Pan[25] model agreed well with the experimentally determined G values for each specimen in this study, including the measurements performed by the IE and RUS techniques as well as for both the 60 and 100 μm C_f KGP specimens (Fig. 3.3 and Table 3.1). Only the predictions for the Pan[25] model is shown in Fig. 3.3 since, the Pan[25] model does include predictions for G values (Table 3.1), while the Manera[22], Curtis[23], Christensen[20] and modified Halpin-Tsai models[27, 28] do not provide predictions for G (Fig. 3.3 and Table 3.1).

As observed by Lara-Curzio *et al.*[13], the IE and RUS techniques yielded very similar results for isotropic and homogeneous brittle materials such as Pyrex glass and polycrystalline alumina. (Polycrystalline alumina specimens are elastically isotropic if the crystallographic orientation of the grains is random). In this study, the pure KGP specimens were isotropic and homogeneous materials and the Young's and shear moduli obtained from the IE and RUS tests

agreed to within 2.6% and 7.0%, respectively. However, as the fiber loading increased, an increase was observed in both the (1) difference between the IE and RUS measurements of E as well as (2) the experimental uncertainties in the measurements (Fig. 3.2).

For the fiber volume fraction loadings of 0.079 or lower, the plotting symbols were larger than the error bars for the E measurements (Figs. 3.2 and 3.3). However, the uncertainties increased for specimens of both fibers lengths for both the IE and RUS tests (Fig. 3.2), with the increase in uncertainty being especially pronounced for the IE measurements (Fig. 3.2). For the G data, increases in the uncertainty also occurred for fiber loadings > 0.079 but the magnitude of the error bars remained comparable to the size of the plotting symbols (Fig 3.3). The increase in the experimental uncertainty might be related to the increase in viscosity of the slurries that occurs as additional fibers are added. In previous work on the same C_f KGP composite systems, increasing the slurry viscosity via fiber additions resulted in irremovable air traps inside the slurry which in turn increased the irregular porosity of the test pieces[2], where variations in porosity lead to corresponding changes in the elastic moduli.[13] Furthermore, with an increase in fiber loading, local agglomeration of fibers has been observed[2] and while the fiber bundles were still randomly oriented, the agglomeration caused localized shifts in the fiber distribution and thus an increase in specimen inhomogeneity. Therefore, as the fiber volume fraction increased, the effects of porosity and the fiber agglomeration/inhomogeneity may be linked to the scatter in the measured modulus values (Figs. 3.2 and 3.3). However, the reason for the systematic increase in the differences between the E values for the IE and RUS techniques with increasing fiber loading is not clear.

For the 60 and 100 μm C_f KGP specimens, both the Young's and shear moduli increase monotonically with fiber loading, which is in general agreement with each of the composite

models given in Table 3.2. In particular, for the RUS measurements, the experimental E values agreed well with the modified Halpin-Tsai[27, 28] and the Pan[25] models (Fig. 3.2) while the G values corresponded well to the theoretical values obtained from the Pan[25] model (Fig. 3.3). Thus, all of the E and G values for the RUS measurements can be described relatively well by the Pan[25] model (Figs. 3.2 and 3.3). For the IE measurements, the G results agreed with the Pan[25] model (Fig. 3.3) while the E data increasing diverges from the Christensen[20] model with increasing fiber loading (Fig. 3.2). However, the Curtis[23] and modified Halpin-Tsai[27, 28] models also included the fiber aspect ratio (Table 3.1). In this study, since the fiber diameter was essentially constant, the aspect ratio was expected to change in proportion to the fiber length so one might expect the elastic moduli to be functions of fiber length. However, for a given volume fraction loading of fibers, the measured shear moduli were essentially independent of the fiber length (Fig. 3.3 and Table 3.2). In addition, for the Young's modulus measurements by both IE and RUS, the differences in the E values between the 60 and 100 μm fiber lengths were comparable to the magnitude of the error bars (Fig. 3.2). Thus, in this study there were no clear effects of fiber length on the measured elastic moduli. The lack of a definitive link between elastic moduli and fiber length is in contrast to the fracture testing conducted in this study where the deflection of cracks around longer fibers improved the flexure strength of the materials. Further studies should be carried out with a greater range of fiber lengths and/or aspect ratios to clarify the effect of the fiber length and fiber aspect ratio on the elastic moduli.

c. Static Mechanical Properties

i. Uniaxial Compressive Strength, Compressive Modulus and Weibull Modulus

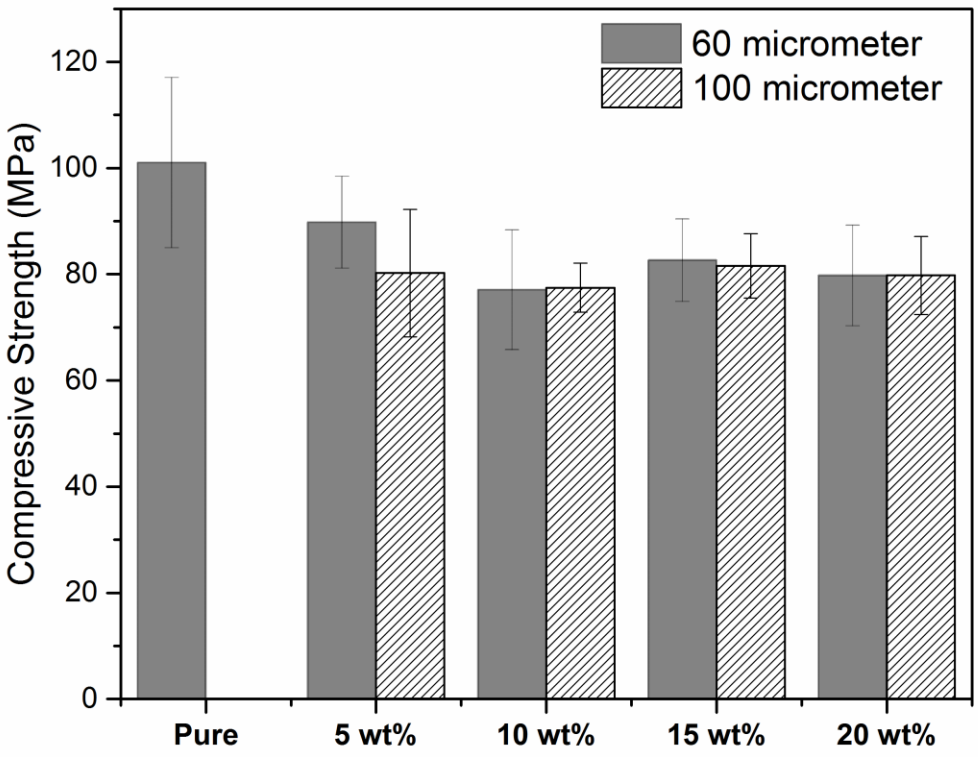

Fig. 3.4. Average uniaxial compressive strengths of carbon fiber-reinforced, potassium geopolymer composites.

Fig. 3.4 summarizes the compressive strengths of C_f KGP for 60 and 100 μm fibers. Pure potassium geopolymer had the highest compressive strength of 101 ± 16 MPa. With increasing carbon fiber loading, the compressive strength tended to decrease, because the fibers could be considered as defects in the compressive test. However, above 10 wt% carbon loading, the compressive strengths started to increase and reached around 80 MPa, regardless of the fiber lengths. Since the fibers were short and randomly oriented in the composite, a certain amount of fibers behaved as reinforcements in compression, although a small amount of fiber decreased the

initial compressive strength. In this study, the 10 wt% of fiber loading was the threshold for fibers to reinforce the composite in compression.

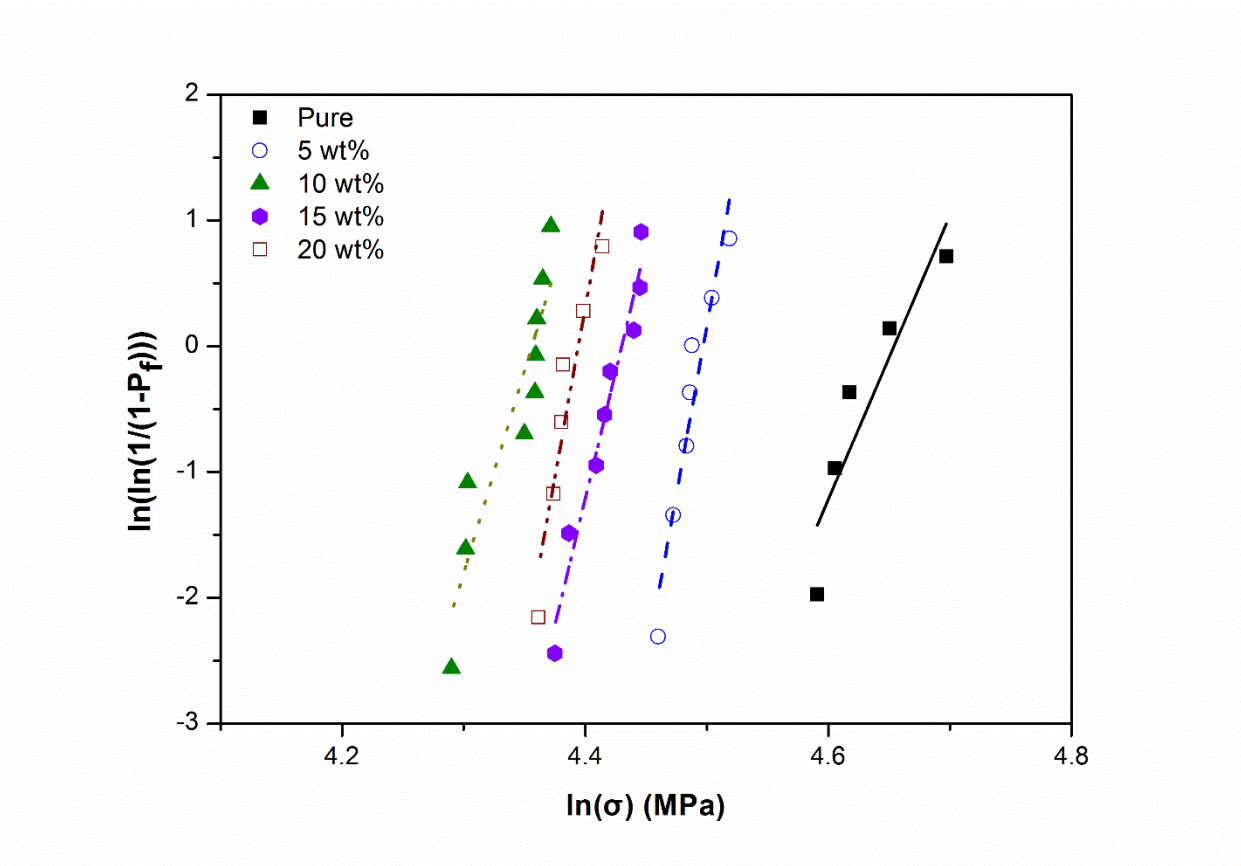

Fig. 3.5. Weibull plots of 60 µm C_f KGP based on uniaxial compressive strengths.

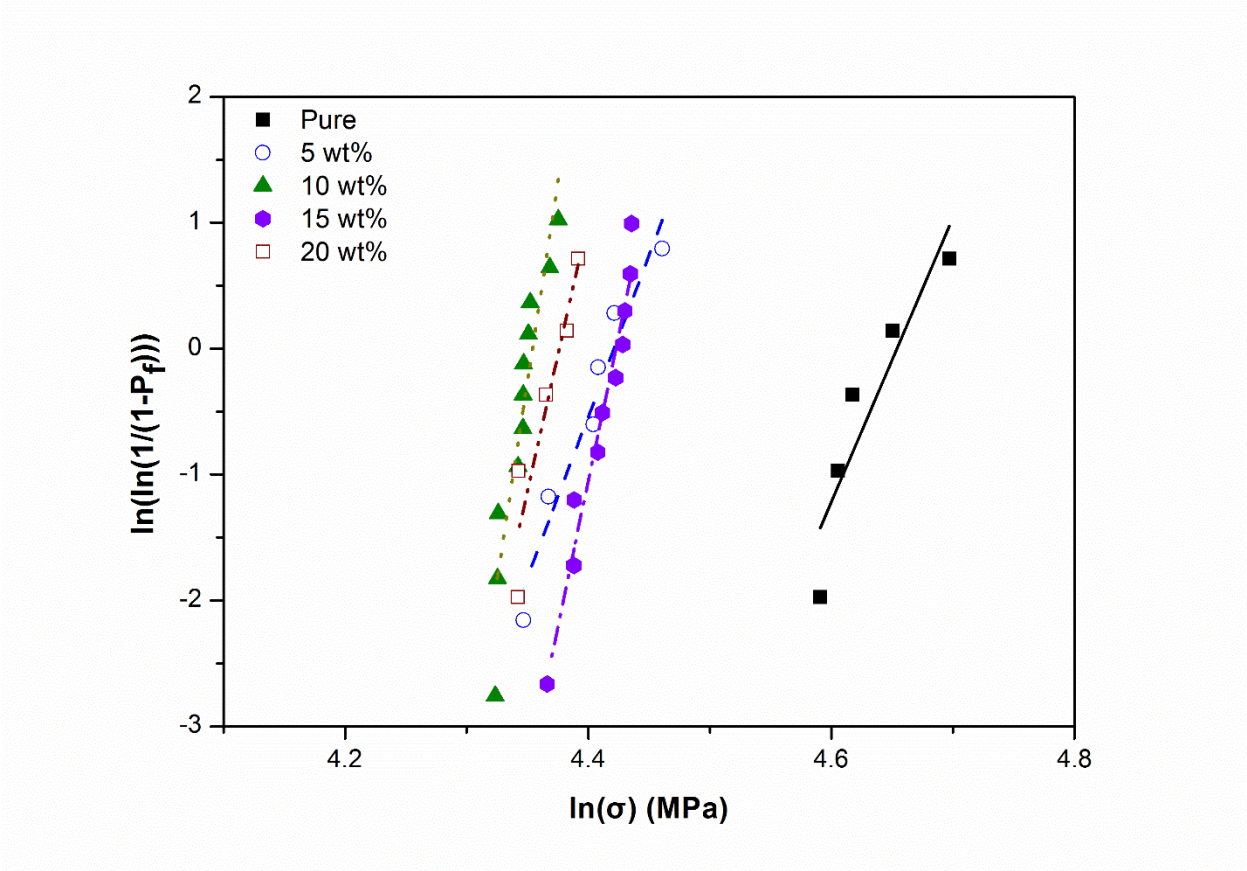

Fig. 3.6. Weibull plots of 100 µm C_f KGP based on uniaxial compressive strengths.

Table 3.3. Weibull Moduli m and Characteristic Strength α Measured from Uniaxial Compressive Testing

	Pure	60 µm carbon fiber				100 µm carbon fiber			
		5 wt%	10 wt%	15 wt%	20 wt%	5 wt%	10 wt%	15 wt%	20 wt%
m	23	54	32	41	54	26	63	46	43
σ_θ (MPa)	105	90	78	84	81	83	78	83	80

The Weibull plots are presented in Figs. 3.5 and 3.6 and Table 3.3, where the slopes of the plots are proportional to the Weibull moduli. The black line and dots were measured for pure potassium geopolymer and plotted in both Figs. 3.5 and 3.6. Similar to the average values, a maximum characteristic strength, σ_θ, of 105 MPa was obtained with pure geopolymer and increasing the fiber loading decreased the strength to around 80 MPa. In order to meet the design

requirement as a structural material, not only the maximum compressive strength but also the consistency of failure should be considered. The maximum values of Weibull moduli, 54 and 63, were achieved with 5 wt% and 10 wt% of 60 and 100 µm C_f KGP, respectively. It was noted that the Weibull moduli of C_f KGP were always higher than that of the pure geopolymer, although the strengths were lower. Particularly, the 5 wt% 60 µm C_f KGP had twice as high a Weibull modulus (54) than that of pure KGP (21) and the highest characteristic strength (90 MPa) among the C_f KGP. Therefore, by considering both Weibull modulus and characteristic strengths of composites, 5 wt% 60 µm C_f KGP was determined to be the most reliable composite in compressive testing.

ii. Biaxial Tensile Strength, Compressive Modulus and Weibull Modulus

The average biaxial tensile strengths from ROR tests are shown in Fig. 3.7. Increased fiber loading resulted in improved biaxial tensile strength. The average strength of 13.2 ± 3.1 MPa was observed for pure potassium geopolymer and the maximum average strength was 28.3 ± 3.9 MPa for 20 wt% of 100 µm C_f KGP. By adding short carbon fibers up to 20 wt%, the biaxial strength was improved by more than two-fold. Moreover, the effect of fiber length significantly improved the strength of composites in this test. The 5, 10, 15 and 20 wt% of C_f KGP produced 1, 14, 7 and 25 % increments, respectively.

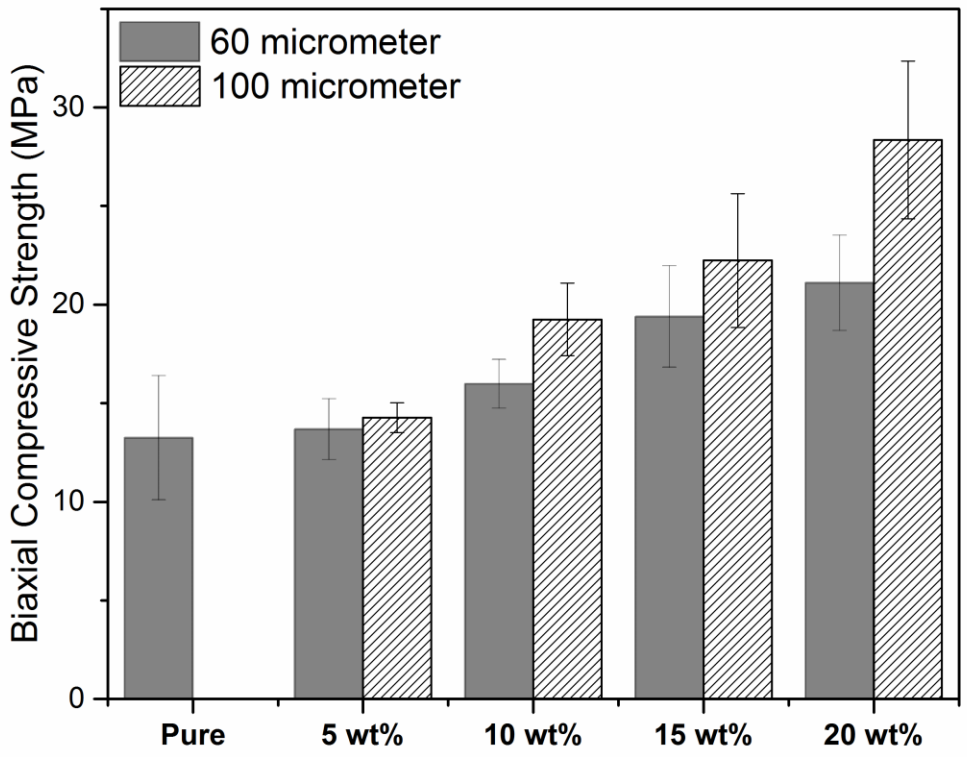

Fig. 3.7. Average biaxial tensile strengths of carbon fiber-reinforced geopolymer composites.

The resulting fracture strength, σ_f in Fig. 3.8 increased linearly with loading of carbon fiber, as fit by least squares to the following linear equation.

$$\sigma_f(x) = \sigma_{f,0} + x b_\sigma \tag{3.2}$$

where $\sigma_{f,0}$ is the fracture at the 0 wt% carbon fiber intercept, x is the wt% of fiber in the sample, b_σ is the linear rate of change of σ_f with x, and $\sigma_f(x)$ is the fracture strength as a function of x. The fracture strength increase with 100 µm fiber addition was greater than that with 60 µm additions. For the 60 µm carbon fiber, b was 0.43 ± 0.06 GPa/(wt% 60 µm fiber), while for the 100 µm C_f,

b was 0.76 ± 0.09 GPa/(wt% 100 µm fiber. The values for zero fiber intercept, $\sigma_{f,0}$, were 12.4 ± 0.7 MPa and 11.8 ± 1.1 MPa for 60 and 100 µm fibers, respectively.

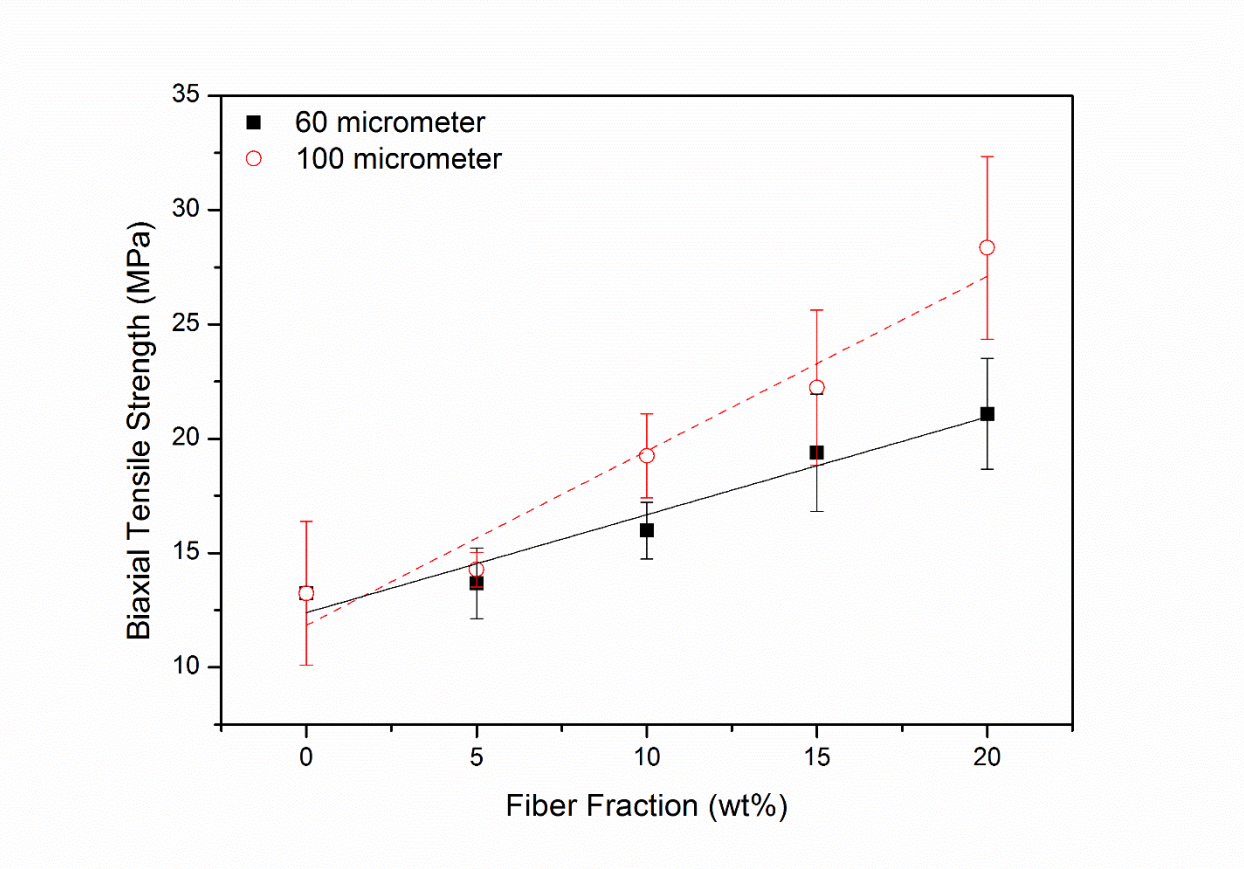

Fig. 3.8. Linear fitted biaxial tensile strengths of 60 and 100 µm C_f KGP.

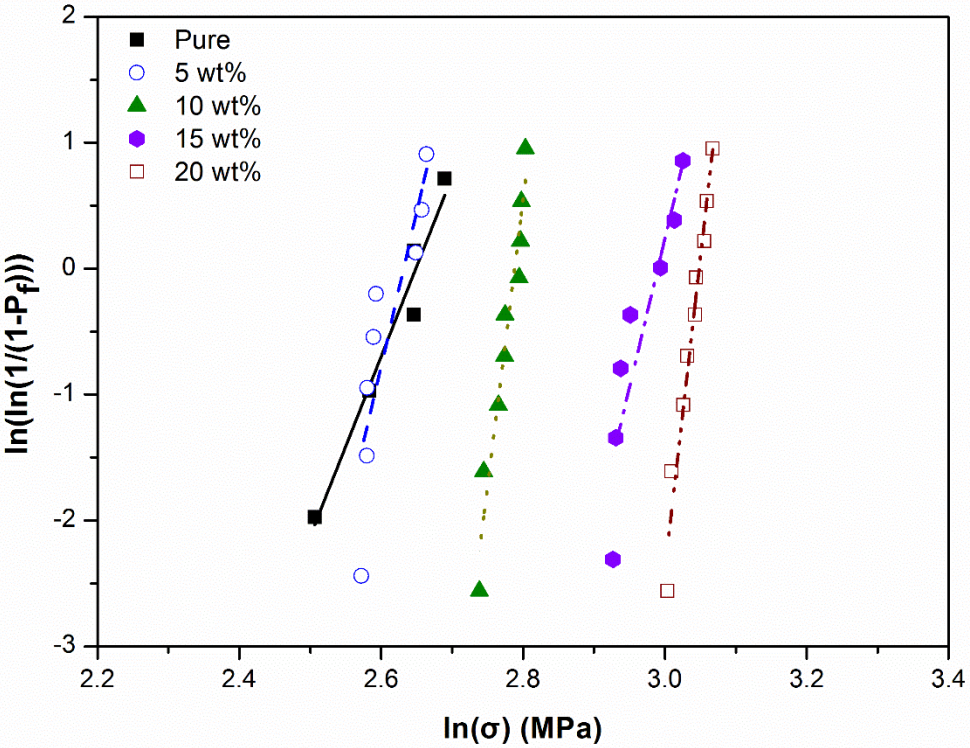

Fig. 3.9. Weibull plots of 60 µm C_f KGP based on biaxial tensile strengths.

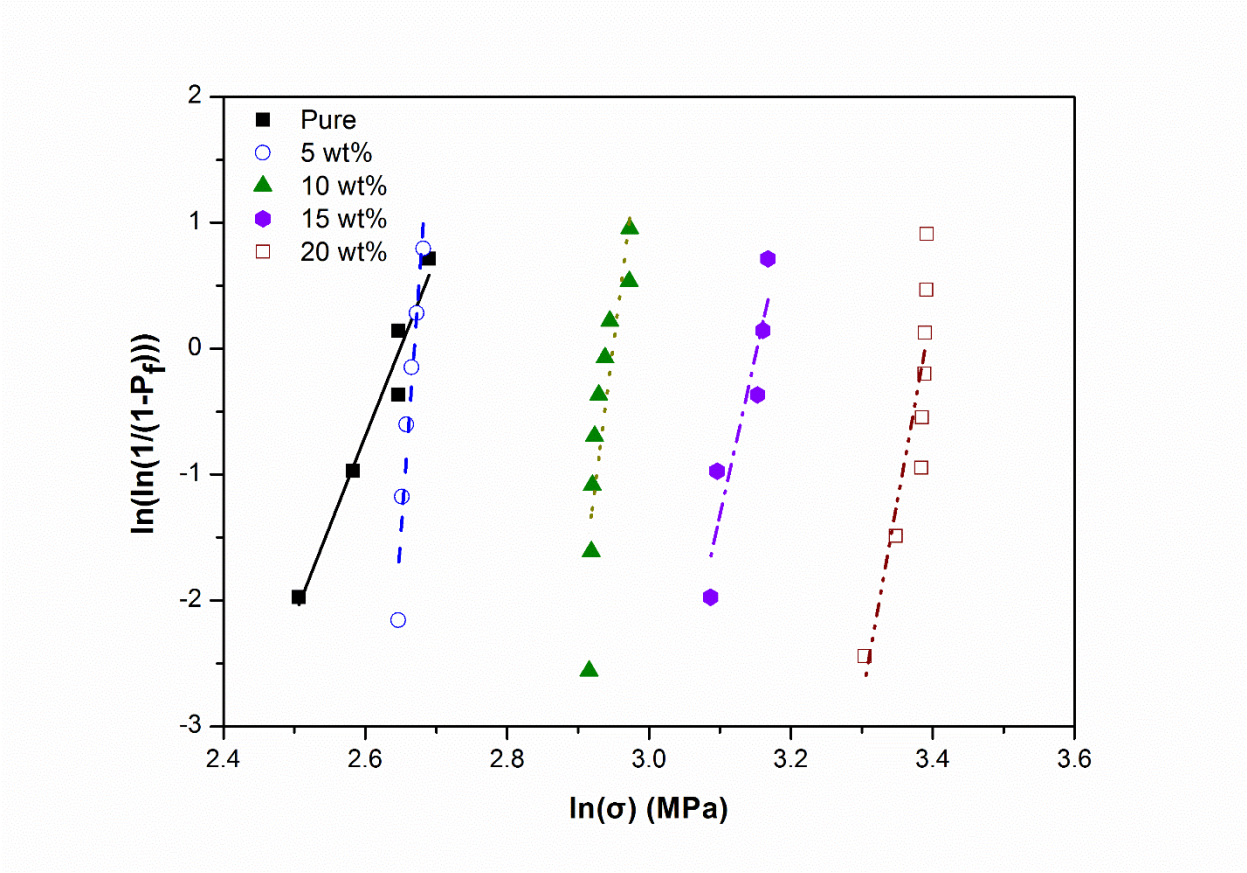

Fig. 3.10. Weibull plots of 100 µm C_f KGP based on biaxial tensile strengths.

Table 3.4. Weibull Moduli m and Characteristic Strength α Measured from Biaxial Tensile Testing

	Pure	60 µm carbon fiber				100 µm carbon fiber			
		5 wt%	10 wt%	15 wt%	20 wt%	5 wt%	10 wt%	15 wt%	20 wt%
m	14	24	45	24	50	78	44	25	31
σ_θ (MPa)	14	14	16	20	21	14	19	23	29

Figs. 3.9 and 3.10 and Table 3.4 summarize the Weibull moduli, m and the characteristic values of biaxial fracture strength for both 60 and 100 µm C_f KGP. The pure potassium geopolymer had a Weibull modulus of 14 indicating relatively high scatter in failure. By adding

60 µm fibers, the highest Weibull modulus of 50 was observed at 20 wt% C_f KGP. The characteristic strength improved up to 21 MPa from 14 MPa. For 100 µm C_f KGP, 5 wt% increased the Weibull modulus by 5 times, although the characteristic strength was the same. The strength also increased by more than two times at 20 wt% with a doubling of the Weibull modulus compare to pure KGP. The longer fiber improved the biaxial tensile strengths by 18, 15, and 38 % for 10, 15, and 20 wt% C_f KGP, respectively. It is worth noting that the Weibull modulus of 5 wt% 100 µm C_f KGP was increased by 325% compared to that of 5 wt% 60 µm C_f KGP. On the other hand, at 20 wt% fiber loading, the 100 µm C_f KGP significantly reduced the Weibull modulus by 38 % as compared to that of 60 µm C_f KGP. This indicated that while crack deflection by longer fibers resulted in an increase in strength, the lower workability of longer and higher fiber loaded slurries reduced the Weibull modulus, i.e. the consistency of failure.

3. 5 Conclusion and Discussion

Taking advantage of geopolymers as a liquid precursor of ceramics, the use of geopolymer can be explored in many disciplines. With short carbon fibers, the strengths of geopolymers were enhanced and manipulated without deteriorating the easy manufacturing process of geopolymer composites. In this study, the 60 and 100 µm carbon fibers were added to potassium geopolymers and the mechanical properties were investigated by various tests.

Randomly oriented short carbon fiber-reinforced, potassium geopolymer composites were tested to measure various mechanical properties by different methods. The impulse excitation (IE) and resonance ultrasound spectroscopy (RUS) techniques measured the Young's moduli and shear moduli of composites based on their frequency responses and were compared to various theoretical predictions. The Young's moduli of C_f KGP from IE tests were placed

above the Christensen[20] model and the results from RUS followed the Pan[25] and modified Halpin-Tsai[26, 27] models. For the shear modulus, both IE and RUS followed the Pan[25] model which considered the three dimensional orientation of short fibers. As the amount of both 60 and 100 μm fibers increased, the overall Young's moduli and shear moduli increased. The IE test showed higher values of moduli than did the RUS and the effects of fiber length on Young's and shear moduli were determined empirically.

In uniaxial compressive strengths, the 15 wt% of 60 μm C_f KGP and 10 wt% of 100 μm C_f KGP were the most reliable composites having strengths of 80 MPa. Although the compressive strength decreased as the fiber content increased, the biaxial tensile strength showed linear increments of strength for both 60 and 100 μm C_f KGP. At 5 wt% of 100 μm C_f KGP, the Weibull modulus of the KGP composite increased by six times that of pure potassium geopolymer. Moreover, the biaxial tensile strength increased twice at 20 wt% of 100 μm C_f KGP with twice the Weibull modulus. The effect of fiber length was noticeable in ROR tests by improving 37% of strength at 20 wt% fiber loadings. The details of stress-strain curves of uniaxial compressive tests and load-displacement curves of biaxial tensile tests were shown in the supplementary information.

In the microstructures of C_f KGP, the carbon fibers were randomly oriented in the geopolymer matrix in which we could preserve the assumption of isotropy but the distributions of fibers were varied as shown in micrographs of fracture surfaces, which caused the material to be inhomogeneous. As we described above, the inhomogeneity of C_f KGP resulted in the discrepancy of the elastic values between IE and RUS tests. Moreover, the existence of porosity in the geopolymer matrix should be addressed here in order to understand the microstructural detail of geopolymer composites. The volume fraction of potassium geopolymer was 40 vol%

and average closed pore size of 6.8 nm in diameter was measured by gas adsorption porosimetry[34]. The porosity was homogeneously distributed closed nanoporosity, so that the material was impervious.

In the Weibull moduli, the m value was highest for 5 wt% at 100 µm fibers but 10 wt% at 60 µm fibers since the two fiber loadings are approximately equivalent and in this easy of discrete fibers longer fibers are more effective in crack deflection than shorter fibers. Thus, smaller amount of longer fiber loadings corresponded to higher fiber loading of shorter fibers. Moreover, the Weibull moduli of compression and ROR tests were different since those tests were performed to measure two different mechanical properties of the composites. Pure compression test consists of compressive force applied uniaxially, while ROR involves biaxial tensile components.

Using different carbon sources such as carbon nanotubes[35, 36] or graphene[37], the fly ash based geopolymers[35, 36] or other types of ceramics[37] were reinforced to enhance their mechanical, thermal and electrical properties. The strength of composites were significantly improved by adding small amounts of reinforcements due to the high strength of CNT and graphene.

3. 6 Supplementary Information

S.Figs. 3.1, 3.2 and 3.3 are stress-strain curves of uniaxial compressive tests containing different carbon loadings. The 5 wt% of 60 µm C_f KGP was denoted 60_5 in the figure. All other fiber loadings followed the same notation. (e.g., 100_20 indicated 20 wt% 100 µm C_f KGP)

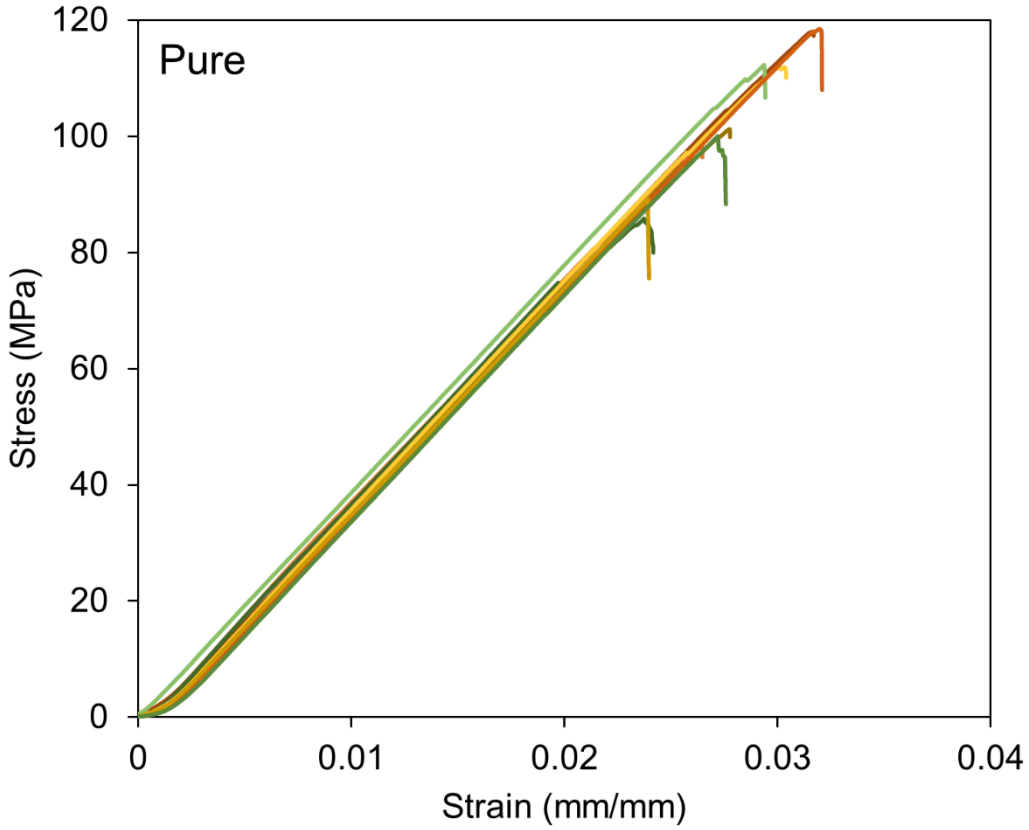

S.Fig. 3.1. Stress-strain curves of pure KGP under uniaxial compression.

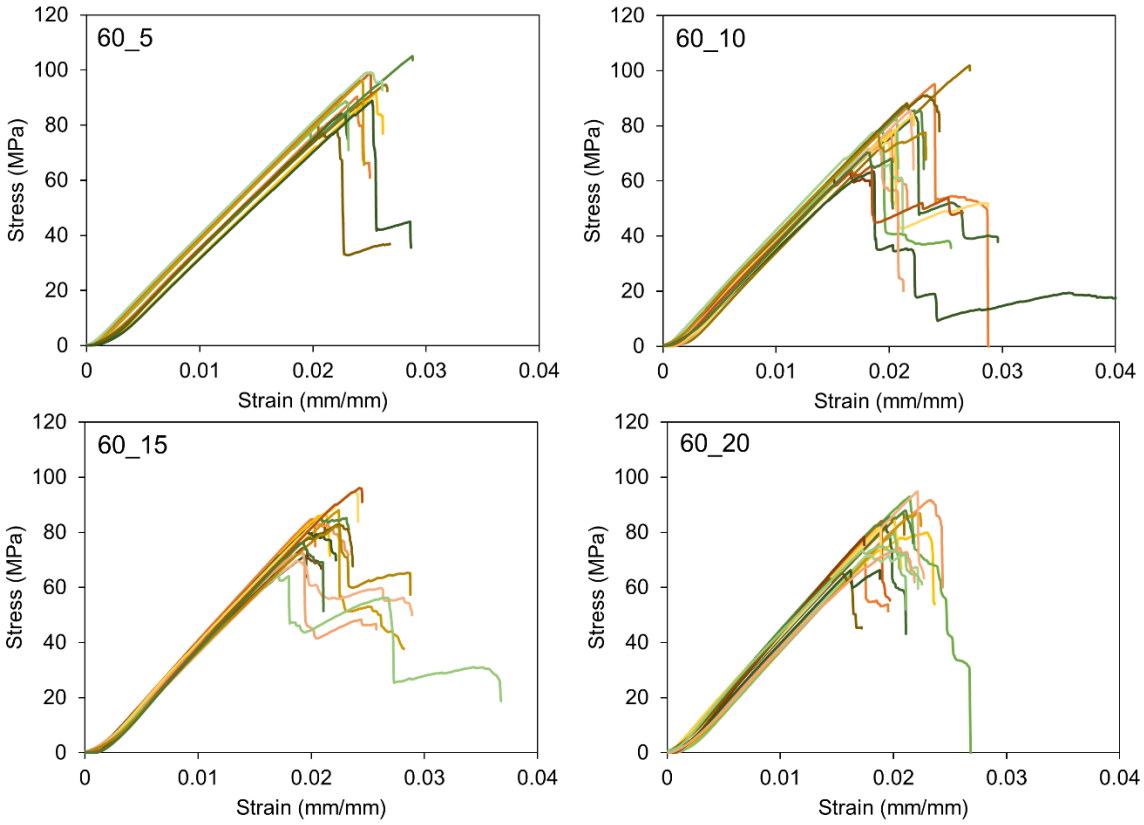

S.Fig. 3.2. Stress-strain curves of 60 µm C_f KGP under uniaxial compression.

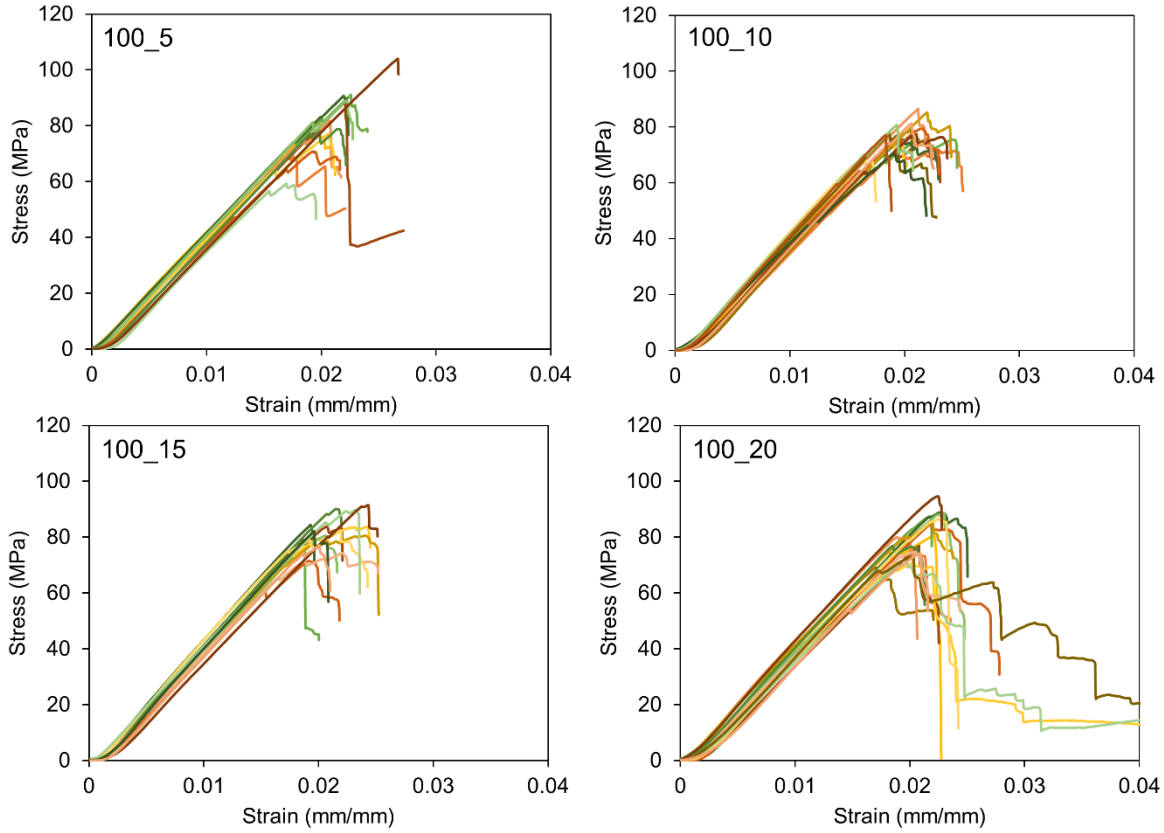

S.Fig. 3.3. Stress-strain curves of 100 µm C_f KGP under uniaxial compression.

S.Figs. 3.4 and 3.5 are load-displacement curves of biaxial tensile tests for different carbon loadings. The curves plotted in S.Figs. 3.4 and 3.5 are fairly typical in most cases of what has been seen in ROR on alumina. The first part of the curve is loading up primarily the compliant sheet material, which was allowed in the standard for materials that are not a smooth, polished surface to prevent point loading rather than ring loading. The offset differences were due to manual positioning differences between specimens before starting the loading, and are not significant.

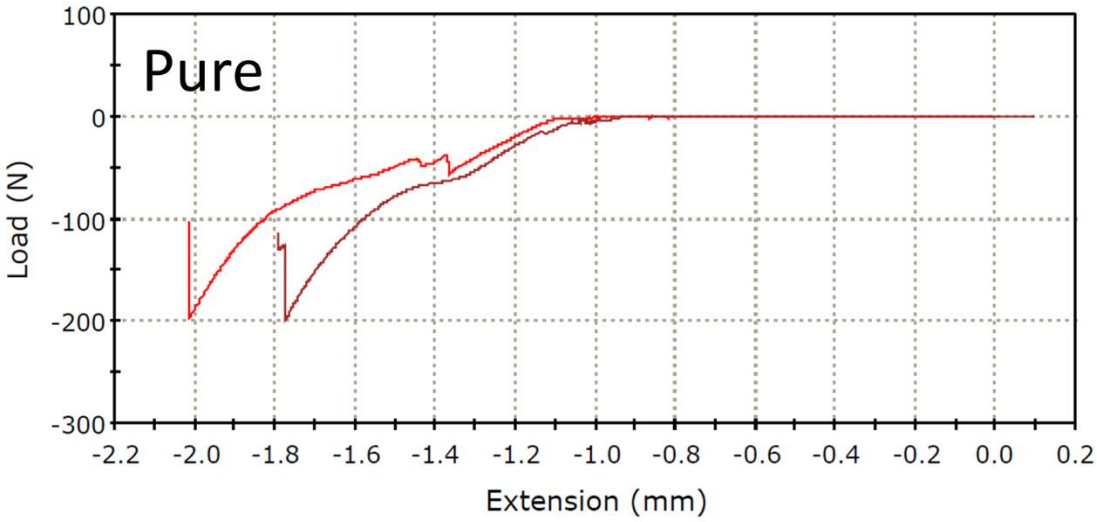

S.Fig. 3.4. Load-displacement curve of pure KGP in biaxial tensile test.

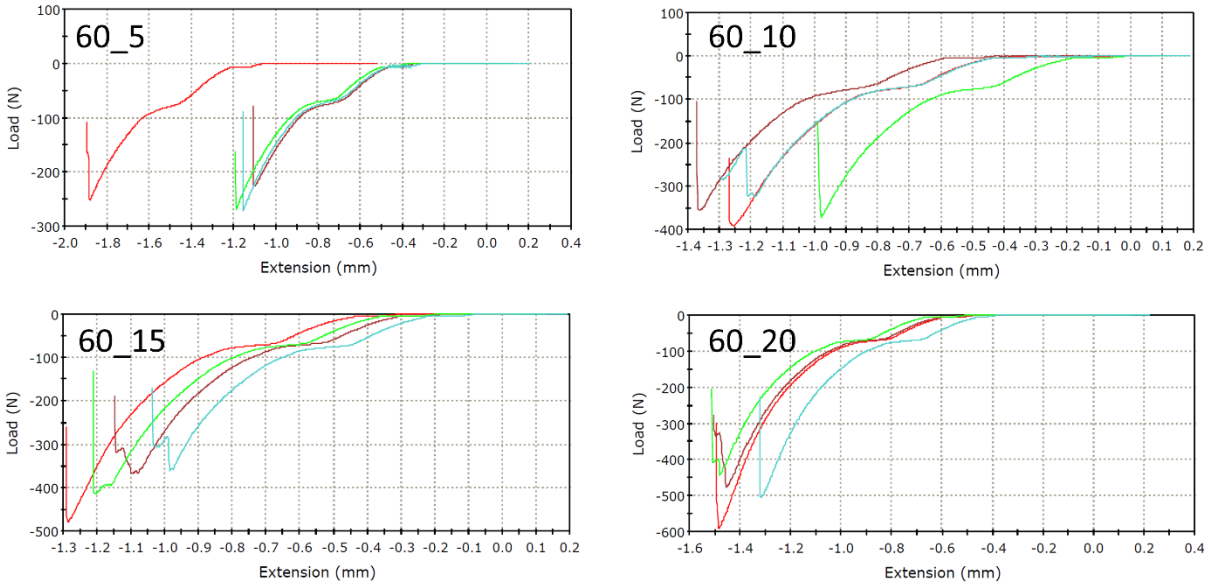

S.Fig. 3.5. Load-displacement curve of 60 µm C_f KGP in biaxial tensile test.

3. 7 References

1. F. U. A. Shaikh, "Review of Mechanical Properties of Short Fibre Reinforced Geopolymer Composites," *Constr. Build. Mater.,* **43**[0] 37-49 (2013).

2. S. Cho and W. M. Kriven, "Short Carbon Fiber-Reinforced, Geopolymer Composites. Part I. Intrinsic Mechanical Properties," *Submitted ; Ceramics International.* (2015).

3. W. Li and J. Xu, "Mechanical Properties of Basalt Fiber Reinforced Geopolymeric Concrete under Impact Loading," *Mater. Sci. Eng., A,* **505**[1-2] 178-86 (2009).

4. V. F. Nesterenko, "Dynamics of Heterogeneous Materials.*"* Springer, (2001).

5. C. Daraio, V. Nesterenko, E. Herbold and S. Jin, "Tunability of Solitary Wave Properties in One-Dimensional Strongly Nonlinear Phononic Crystals," *Phys. Rev. E,* **73**[2] 026610 (2006).

6. M. Nishida, K. Tanaka and T. Ishida, "Dem Simulation of Wave Propagation in Two-Dimensional Ordered Array of Particles," pp. 815-20. in Shock Waves**.** Springer, 2009.

7. K. Jayaprakash, Y. Starosvetsky, A. F. Vakakis, M. Peeters and G. Kerschen, "Nonlinear Normal Modes and Band Zones in Granular Chains with No Pre-Compression," *Nonlinear Dyn.,* **63**[3] 359-85 (2011).

8. A. Leonard and C. Daraio, "Stress Wave Anisotropy in Centered Square Highly Nonlinear Granular Systems," *Phys. Rev. Lett.,* **108**[21] 214301 (2012).

9. A. Leonard, F. Fraternali and C. Daraio, "Directional Wave Propagation in a Highly Nonlinear Square Packing of Spheres," *Exp. Mech.,* **53**[3] 327-37 (2013).

10. M. Hasan, Y. Starosvetsky, A. Vakakis and L. Manevitch, "Nonlinear Targeted Energy Transfer and Macroscopic Analog of the Quantum Landau–Zener Effect in Coupled Granular Chains," *Physica D,* **252** 46-58 2013).

11. M. A. Hasan, S. Cho, K. Remick, A. F. Vakakis, D. M. McFarland and W. M. Kriven, "Primary Pulse Transmission in Coupled Steel Granular Chains Embedded in Pdms Matrix: Experiment and Modeling," *Int. J. Solids Struct.*, **50**[20] 3207-24 (2013).

12. M. A. Hasan, S. Cho, K. Remick, A. F. Vakakis, D. M. McFarland and W. M. Kriven, "Experimental Study of Acoustic Bands and Propagating Breathers in Ordered Granular Media Embedded in Matrix," *Granular Matter*, **17**[1] 49-72 (2015).

13. M. Radovic, E. Lara-Curzio and L. Riester, "Comparison of Different Experimental Techniques for Determination of Elastic Properties of Solids," *Mater. Sci. Eng., A*, **368**[1-2] 56-70 (2004).

14. A. Migliori, Sarrao, J.L., "Resonant Ultrasound Spectroscopy: Applications to Physics, Materials Measurements, and Nondestructive Evaluation.." Wiley: New York, (1997).

15. ASTM, "Standard Test Method for Dynamic Young's Modulus, Shear Modulus, and Poisson's Ratio by Impulse Excitation of Vibration.." in West Conshohocken: ASTM International, Vol. **ASTM 1876-07** (2007).

16. F. Ren, E. D. Case, J. E. Ni, E. J. Timm, E. Lara-Curzio, R. M. Trejo, C. H. Lin and M. G. Kanatzidis, "Temperature-Dependent Elastic Moduli of Lead Telluride-Based Thermoelectric Materials," *Philos. Mag.*, **89**[2] 143-67 (2009).

17. J. E. Ni, E. D. Case, K. N. Khabir, R. C. Stewart, C.-I. Wu, T. P. Hogan, E. J. Timm, S. N. Girard and M. G. Kanatzidis, "Room Temperature Young's Modulus, Shear Modulus, Poisson's Ratio and Hardness of PbTe–Pbs Thermoelectric Materials," *Mater. Sci. Eng., B*, **170**[1–3] 58-66 (2010).

18. R. D. Schmidt, E. D. Case, J. E. Ni, R. M. Trejo, E. Lara-Curzio, R. J. Korkosz and M. G. Kanatzidis, "High-Temperature Elastic Moduli of Thermoelectric $SnTe_{1\pm x}$ – y SiC Nanoparticulate Composites," *J. Mater. Sci.,* **48**[23] 8244-58 (2013).

19. J. C. Halpin, "Effects of Environmental Factors on Composite Materials." in. DTIC Document, 1969.

20. R. Christensen and F. Waals, "Effective Stiffness of Randomly Oriented Fibre Composites," *J. Compos. Mater.,* **6**[3] 518-35 (1972).

21. J. Halpin and J. Kardos, "The Halpin-Tsai Equations: A Review," *Polym. Eng. Sci.,* **16**[5] 344-52 (1976).

22. M. Manera, "Elastic Properties of Randomly Oriented Short Fiber-Glass Composites," *J. Compos. Mater.,* **11**[2] 235-47 (1977).

23. P. Curtis, M. Bader and J. Bailey, "The Stiffness and Strength of a Polyamide Thermoplastic Reinforced with Glass and Carbon Fibres," *J. Mater. Sci.,* **13**[2] 377-90 (1978).

24. K. Evans and A. Gibson, "Prediction of the Maximum Packing Fraction Achievable in Randomly Oriented Short-Fibre Composites," *Compos. Sci. Technol.,* **25**[2] 149-62 (1986).

25. N. Pan, "The Elastic Constants of Randomly Oriented Fiber Composites: A New Approach to Prediction," *Science and Engineering of composite materials,* **5**[2] 63-72 (1996).

26. M.-K. Yeh, N.-H. Tai and J.-H. Liu, "Mechanical Behavior of Phenolic-Based Composites Reinforced with Multi-Walled Carbon Nanotubes," *Carbon,* **44**[1] 1-9 (2006).

27. N.-H. Tai, M.-K. Yeh and T.-H. Peng, "Experimental Study and Theoretical Analysis on the Mechanical Properties of SWNTs/Phenolic Composites," *Composites Part B,* **39**[6] 926-32 (2008).

28. ASTM, "Standard Test Method for Monotonic Compressive Strength of Advanced Ceramics at Ambient Temperature." in West Conshohocken: ASTM International, Vol. **C1424-10 (**1996).

29. ASTM, "Standard Test Method for Monotonic Equibiaxial Flexural Strength of Advanced Ceramics at Ambient Temperature." in West Conshohocken: ASTM International, Vol. **C1499-09 2009** (2009).

30. D. K. Shetty, A. R. Rosenfield, P. McGuire, G. Bansal and W. H. Duckworth, "Biaxial Flexure Tests for Ceramics," *Am. Ceram. Soc. Bull.,* **59**[12] 1193-97 (1980).

31. J. Ritter Jr, K. Jakus, A. Batakis and N. Bandyopadhyay, "Appraisal of Biaxial Strength Testing," *Journal of Non-Crystalline Solids,* **38** 419-24 (1980).

32. X. Fan, E. Case, F. Ren, Y. Shu and M. Baumann, "Part I: Porosity Dependence of the Weibull Modulus for Hydroxyapatite and Other Brittle Materials," *J. Mech. Behav. Biomed. Mater.,* **8** 21-36 (2012).

33. X. Fan, E. Case, I. Gheorghita and M. Baumann, "Weibull Modulus and Fracture Strength of Highly Porous Hydroxyapatite," *J. Mech. Behav. Biomed. Mater.,* **20** 283-95 (2013).

34. W. M. Kriven, "Inorganic Polysialates or "Geopolymers," *Am. Ceram. Soc. Bull.,,* **89**[4] 31-34 (2010). 33

35. K. J. D. MacKenzie and M. J. Bolton, "Electrical and Mechanical Properties of Aluminosilicate Inorganic Polymer Composites with Carbon Nanotubes," *J. Mater. Sci.,* **44**[11] 2851-57 (2009).

36. M. Saafi, K. Andrew, P. L. Tang, D. McGhon, S. Taylor, M. Rahman, S. Yang and X. Zhou, "Multifunctional Properties of Carbon Nanotube/Fly Ash Geopolymeric Nanocomposites," *Constr. Build. Mater.,* **49** 46-55 (2013).

37. X. Huang, X. Qi, F. Boey and H. Zhang, "Graphene-Based Composites," *Chemical Society Reviews*, **41**[2] 666-86 (2012).

CHAPTER 4: MECHANICAL, THERMAL AND ELECTRICAL PROPERTIES OF POTASSIUM GEOPOLYMER CONTAINING GRAPHENE NANOPLATELETS

4. 1 Abstract

Graphene nanoplatelets have high mechanical, electrical and thermal properties that can significantly improve the desired properties of composites at even low contents. 1, 2 and 3 wt% of graphene nanoplatelet-reinforced, potassium geopolymers (GNP KGP) were prepared and their microstructures were investigated by SEM, XRD and Raman spectroscopy. The mechanical properties such as flexure strength, Weibull modulus and Young's modulus were measured by four-point flexure and impulse excitation (IE) testing. Moreover, silicon functionalized graphene nanoplatelets (sGNP) were prepared in order to enhance interfacial bonding between GNP and geopolymer matrix. The flexural mechanical properties of sGNP KGP were measured and compared with GNP KGP, in order to investigate the effect of silicon functionalization. In addition to mechanical properties, the electrical and thermal conductivities of GNP KGP were investigated by measuring electric resistances and heat flow of the materials.

4. 2 Introduction

Environmentally friendly materials were studied as a replacement for Ordinary Portland Cement (OPC) which emits about 6% of the carbon dioxide in the atmosphere. Geopolymer (inorganic aluminosilicate polymers) emits 80% less carbon dioxide than does OPC while maintaining the desirable properties of a structural material (higher strength and faster setting time compared to OPC). Various properties of geopolymer such as chemical, mechanical, electrical and thermal properties, are still under investigation. [1, 2, 3] Exceptional properties of geopolymer opens up many application in various disciplines such as high fire resistant coatings, adhesives, high temperature ceramics, and radioactive waste encapsulation.[4, 5, 6] Chemical compositions of geopolymer are alumina, silica and alkali metal oxides (Na, K, Cs) and the fluid mixture of geopolymer allows them to be cast in any desired shapes.

However, geopolymer is still a brittle material and catastrophic failures have been observed although it has high strengths.[7, 8] In order to improve the strength of geopolymers, fiber reinforcements such as polyvinyl alcohol (PVA), chopped basalt fibers, cotton, polypropylene, and carbon have been used to enhance the mechanical properties. High aspect ratio, strength and adhesion properties of fibers to geopolymer matrix play a role in increasing its strength. Not only fibers but also platelets and particulates have been incorporated to reinforce geopolymers.[7, 8, 9]

Carbon based fillers has been used to achieve desired properties in composites due to their exceptional mechanical, electrical and thermal properties. For carbon fiber reinforced geopolymer, the research reported the flexural strength increased 4.4 times with 7 mm long fibers.[10, 11] Those carbon preform based fibers provided high strength but it also increased the difficulty of composite synthesis and limited the creation of simple shapes. While conserving the effect of reinforcements, short carbon fibers of 60 and 100 μm enabled the simple processing of

geopolymers and fabricated any complicated shapes by simple mold-cast process.[12, 13] Nano- or micro-carbon platelets such as graphene, graphene nanoplatelet and graphite also increased mechanical, electrical and thermal properties of composites without raising the processing difficulty. The high electrical and thermal conductivities of carbon based platelets could improve the electrical and thermal properties of composites while the high aspect ratio of the platelets would most likely improve their strength.

In 2004, the single atomic layer of carbon, graphene, was first fabricated and recorded as the strongest material. Graphene has been utilized in many applications due to its exceptional mechanical, electrical and thermal properties. However, the process of creating pure graphene where by sophisticated instruments are required and low yields resulted in high cost of graphene and subsequently limited its applications. Commercial graphene can be obtained in the form of several layers, known as graphene nanoplatelets (GNP). Graphene nanoplatelets are ideally used for composites that have specific properties: high fracture toughness, electromagnetic shielding, electrical conductivity, high thermal conductivity, low flammability and gas barrier resistance.[14] Moreover, the graphene nanoplatelets were functionalized with specific groups to enhance further mechanical properties which were attributed to the increase of interfacial bonding between graphene nanoplatelets and a matrix.[15]

Graphene nanoplatelets has been incorporated into various materials such as polymers, ceramics and concretes. However, graphene nanoplatelet reinforced potassium geopolymer (GNP KGP) has not been reported yet. In this study, the synthesis process of GNP KGP is described and the composites were characterized for different GNP contents. Moreover, the flexural strength, Young's modulus derived from different theoretical models, electrical conductivity as well as

thermal conductivity of GNP KGP were investigated and analyzed by various measurement techniques.

4. 3 Experimental Procedures

a. Materials

i. Graphene Nanoplatelets (GNP)

Table 4.1. Properties of Graphene Nanoplatelets[14]

Average Diameter (μm)	Average Thickness (nm)	Density (g/cm^3)		Young's Modulus (GPa)	Tensile Strength (GPa)	Electrical Conductivity (S/m)	Thermal Conductivity (W/mK)
5 ~ 25	6	2.2	Parallel to Surface	1000	5	10^7	3000
			Perpendicular to Surface	N/A	N/A	10^2	6

The graphite nanoplatelets (GNP) (XG Sciences, East Lansing, Michigan, USA) were used to enhance the mechanical, electrical and thermal properties of a geopolymer matrix. The GNP has an average diameter of 5 μm (Grade M-5) and thickness of 6 nm as shown in Table 4.1. The mechanical, electrical and thermal properties of GNP were provided by the supplier and are listed in Table 4.1.[14] The platelets consisted of 10 to 15 layers of graphene, which were kept close together by Van der Waals forces, and the weakly bonded platelets can easily slip with respect to each other by shear loads. The GNP is highly crystalline with a large surface area of 60 m^2/g and is a nontoxic material. By incorporating the exceptional properties of GNP, the geopolymer composites could open up new applications where high fracture toughness, electrical conductivity and high thermal conductivity are required.

ii. Silicon Functionalized Graphene Nanoplatelet (sGNP)

Functionalization of xGnP-M-5 graphene nanoplatelets (XG-Sciences, Lansing, MI, USA) was carried out by similar procedures as described by Li et al. 25mg of GNPs were under plasma treated by a plasma cleaner (PDC-32G Plasma Cleaner, Harrick Plasma, Ithaca, NY) for 3 minutes to modify the surface, incorporating the OH group to the edge of GNP and then sonicating in ethanol for 5 minutes prior to adding 4000 µl of 28% NH_3 (Aldrich, St. Louis, MO) and 1000 µl of TEOS (Aldrich, St. Louis, MO, USA). The mixture was stirred at 135℃ for 4 hours, while minimizing evaporation. The solution was then vacuum assisted filtered through a cellulose acetate membrane filter (Sartorius Stedim, Bohemia, NY, USA) containing 0.45 µm pores. The filtered material was dried in a vacuum for 12 hours to remove all solvent.

b. Composite Fabrication

Mixing with potassium silicate solution, waterglass, and metakaolin (Metamax HRM, BASF Corp., Florham Park, NJ, USA) resulted in the chemical formula for potassium geopolymer of $K_2O \cdot Al_2O_3 \cdot 4SiO_2 \cdot 11H_2O$. The high shear mixer (Model RW20DZM, IKA. Wilmington, NC, USA) was applied for 5 minutes at 2000 rpm to exfoliate the metakaolin powder to avoid unreacted metakaolins. The mixture underwent planetary mixing (Thinky ARE-250, Intertronics, Kidlington, Oxfordshire, UK) for 3 minutes at 1200 rpm and degassing for 3 minutes at 1400 rpm. Once the geopolymer slurry was prepared, the graphene nanoplatelets were added into the slurry and mixed by the shear and Thinky mixer again. The graphene nanoplatelet reinforced potassium geopolymer (GNP KGP) was cured at 50℃ for 24 hours followed by drying for 7 days in a humidity controlled chamber (1000H Series Temperature/Humidity Chamber, TestEquity, Moorpark, CA, USA) at 20℃ and 30% relative humidity.

c. Microscopic Characterization

Scanning electron microscopy (SEM) was conducted on the Hitachi S4800 high resolution SEM (Tokyo, Japan) and JEOL JSM 6060LV SEM (JEOL USA, Inc., Peabody, MA, USA) in order to observe the dispersion, orientation and interfaces of GNP in KGP. The fracture surface of GNP KGP was sputter coated with Au/Pd alloy to enable SEM imaging as shown in Fig. 4.1.

XRD patterns were collected using a Siemens-Bruker D5000 diffractometer (Madison, WI, USA) with CuKα radiation generated at 30 mA and 40 kV. The specimens were scanned from Bragg angles (2θ) of 5 to 70°. Fig. 4.2 presents the X-ray diffraction results for GNP KGP as well as silicon functionalized graphene nanoplatelets reinforced potassium geopolymer (sGNP KGP).

Raman spectroscopy (ranging from 1000 to 3000 cm^{-1}) was used to investigate the layers of GNP and sGNP. In addition, the exfoliation or dispersion of GNP KGP and sGNP KGP was observed at different processing stages, as-received powder, slurry, solidified geopolymer composites.

Powder samples were analyzed using an FTIR-4100 (Jasco, Inc., Easton, MD, USA) having a scan range of 350-4000 cm^{-1}. A background scan was taken before each powder sample analysis. The scan time was 4 minutes. The resolution of the instrument was 4.0 cm^{-1}. The resulting spectral data under 575 cm^{-1} was truncated to limit irrelevant peaks, baseline corrected, and smoothed using a means-movement algorithm with convolution width of 25 cm^{-1}.

d. Mechanical Characterization

The 4-point bending test[12] was performed to determine the flexural strength of GNP KGP and sGNP KGP. Based on the flexural tests, the Weibull modulus (m) and characteristic strengths (σ_θ) were analyzed in order to investigate the reliability of brittle fracture of geopolymer composites.[12, 16] The Young's modulus of GNP KGP was investigated by the impulsive excitation method. The moduli were calculated based on the dimensions and the frequency responses of specimens under impulse input.[16]

Several theoretical models (Christensen[17], Pan[18], Curtis[19] and Modified Halpin-Tsai[20, 21]) were compared with experimental results of impulse excitation testing.[22] In addition to the modified Halpin-Tsai model, there were two shape factors, constant and exponential. In order to explain and model the nonlinear behavior of nano reinforced composite, the exponential shape factor should be considered similar to that of other polymeric composites.[20, 21]

The Eq. (4.1) is the modified Halpin-Tsai equation with exponential shape factors (ξ).

$$E_c = \frac{1+\xi\eta V_f}{1-\eta V_f} E_m \, , \eta = \frac{\left(\frac{\alpha E_f}{E_m}\right)-1}{\left(\frac{\alpha E_f}{E_m}\right)+\xi} \qquad (4.1)$$

where, V_f is the volume fraction of GNP in geopolymer matrix. E_f, E_m, and E_c are the elastic moduli of GNP, KGP and GNP KGP, respectively. Moreover, α is 1/6 and ξ is $2(\lambda/d)*e^{-a*V_f-b}$. The λ and d are the length and the thickness of GNP, respectively.

e. Electrical and Thermal Conductivities

For both electrical and thermal properties, bulk conductivities were considered in this study rather than the local or surface measurements such as thin films or nano/micro devices, in order to investigate the overall effects of incorporating graphene nanoplatelets in geopolymer matrix. Therefore, the size of specimens and methods of measurement were different from those used in traditional ceramics.

The electrical conductivity was calculated by measuring the electrical resistance and dimensions of specimens. The multimeter was used to measure the bulk electrical resistance of GNP KGP of nominal dimensions 3 x 4 x 13 mm. For the thermal conductivity measurements, disc shaped specimens were prepared having a diameter of 50.8 mm and thickness of 11.2 mm. The bulk heat conductivity at room temperature was measured by a heat flow meter from TA instrument (DTC-300, TA instrument, New Castle, DE, USA) based on the ASTM E1530 standard.[23]

4. 4 Results

a. Microstructure

i. SEM

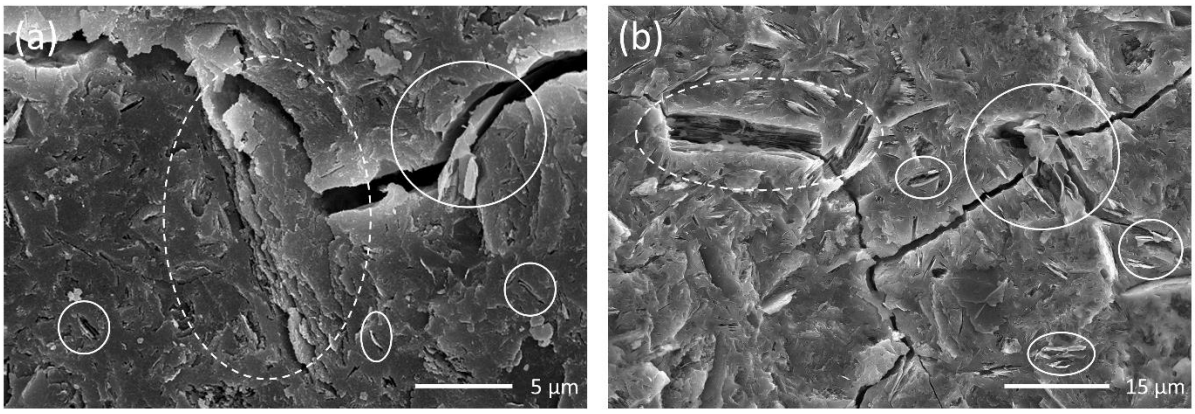

Fig. 4.1. SEM image of (a) GNP KGP and (b) sGNP KGP.

The morphology, topography and composition of GNP KGP and sGNP KGP were characterized by scanning electron microscopy (SEM). Investigating orientation, dispersion and graphene-geopolymer interactions helped to understand the fracture mechanism of the nanocomposites. The fracture surfaces of 1 wt% GNP and sGNP KGP are shown in the Fig. 4.1(a) and (b), respectively. The unreacted metakaolin phase (dashed lines) and the randomly

oriented GNP and sGNP platelets (solid lines) in Fig. 4.1 were observed in both micrographs. At low platelets loadings, the GNP and sGNP were randomly oriented and dispersed in the geopolymer matrix. Thus, any distinguishable differences between GNP and sGNP were not observed in SEM images. Moreover, the silicon functionalized group of sGNP could not be visualized and any interfacial bonding of sGNP to geopolymer matrix were not observed by SEM. However, Fig. 4.1 still showed the distinguished GNP and sGNP in the presence of an unreacted metakaolin. Crack diffraction around platelets was observed in both GNP KGP and sGNP KGP as shown in the large solid circles.

ii. X-ray Diffraction

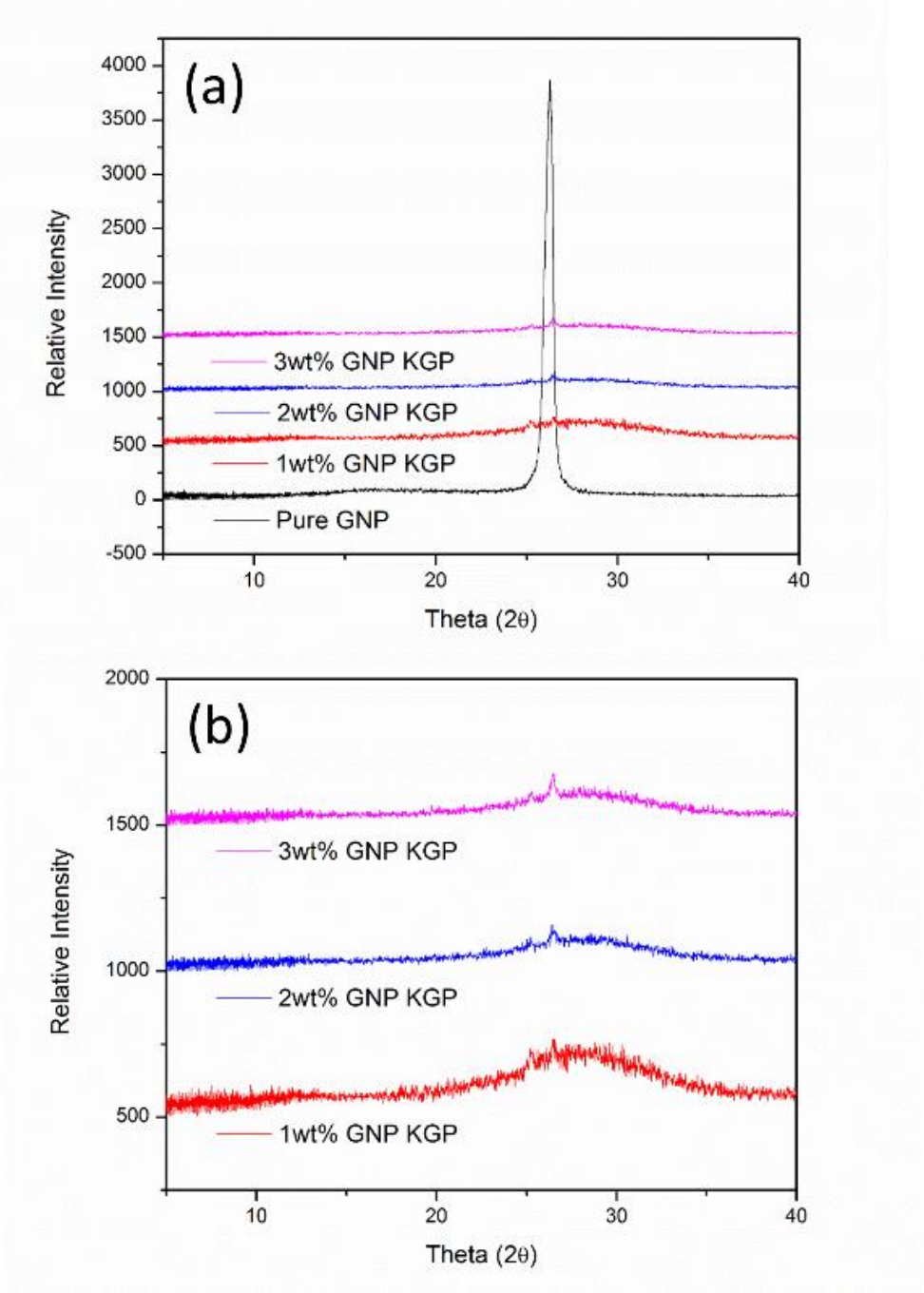

Fig. 4.2. X-ray diffraction of (a), (b) GNP KGP with different GNP contents

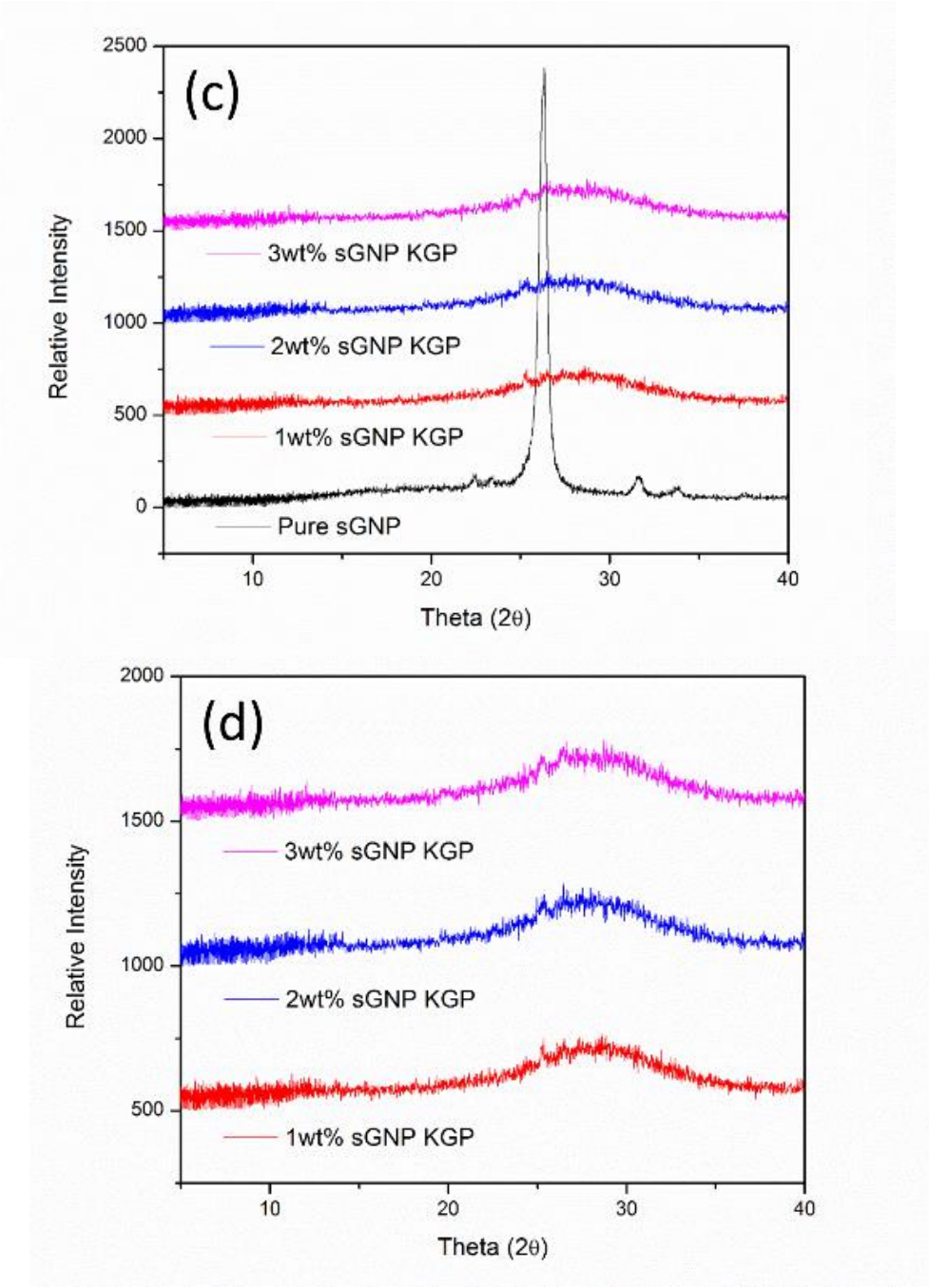

Fig. 4.2. (cont.) X-ray diffraction of (c), (d) sGNP KGP with different sGNP contents

Fig. 4.2 shows the XRD peaks for pure GNP, pure sGNP, GNP KGP and sGNP KGP. The wide diffraction peak from 25° to 35° indicated the general amorphous diffraction pattern of metakaolin-based geopolymer. A sharp peak was observed at 26.6° in Fig. 4.2 (a) and (c) which is related to the graphitic (002) plane having interlayer spacing of 0.34 nm. This graphitic diffraction peak was observed in GNP KGP composites as shown in Fig. 4.2 (b). As the GNP loading increased, the peak at 26.6° started emerging at 2 wt% since the chunk of GNP was not fully exfoliated in the geopolymer matrix. However, the (002) diffraction peak was not observed in any of sGNP KGP composites although the pure sGNP showed the graphitic diffraction peak. This indicated that the silicon functionalization played a role in exfoliating and randomly distributing the platelets within the geopolymer slurry by increasing the space within the graphite layers. In addition, the functionalized silicon group of sGNP attached to the geopolymer matrix during polymerization process which resulted in further exfoliation of sGNP.

iii. Raman Spectroscopy

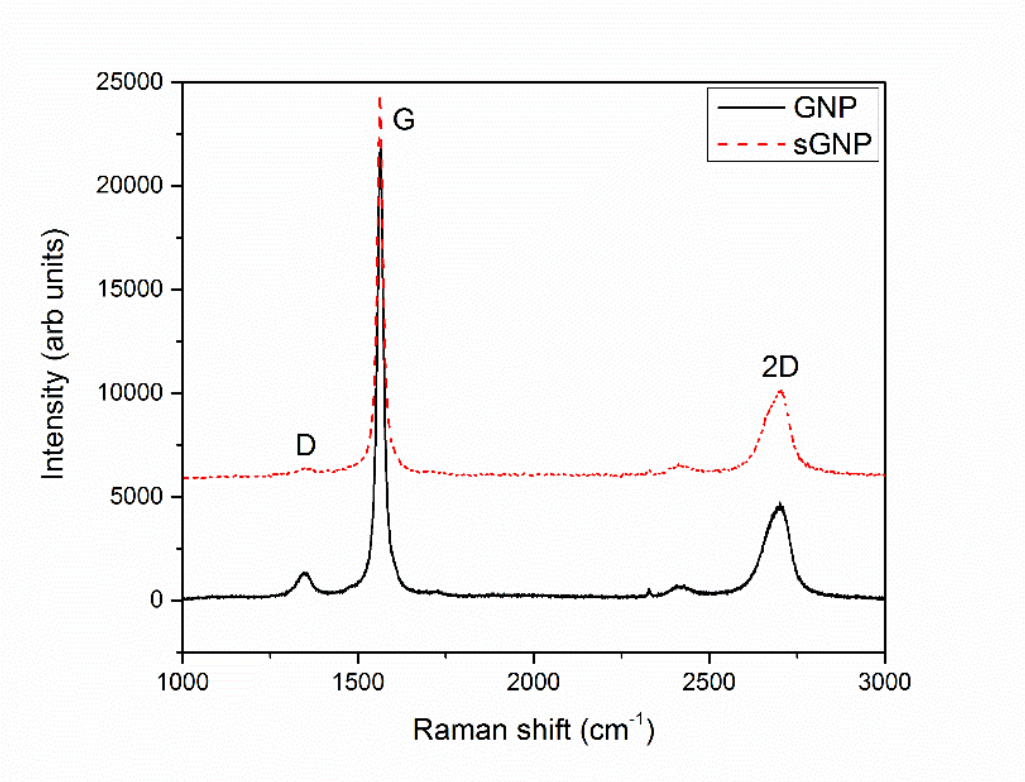

Fig. 4.3. Raman spectroscopy of as-received GNP and sGNP.

Table 4.2. G/2D Peak Comparison in Raman Spectroscopy

	GNP	sGNP	GNP KGP Slurry	sGNP KGP Slurry	GNP KGP	sGNP KGP
G/2D	4.78	4.74	3.57	4.14	4.50	4.50

As-received GNP and silicon functionalized GNP were characterized by Raman spectroscopy as shown in Fig. 4.3 and Table 4.2. Three peaks were distinguished at ~1338, ~1564, and 2693 cm^{-1} and are indicated as D, G and 2D bands in graphene, respectively. It is known that the intensity ratio of G and 2D bands is sensitive to the number of layers of graphene.[24] For the pristine graphene, the 2D band is much higher than the G band.[24] Therefore, the decrease of G/2D ratio corresponded to the separation of graphene nanoplatelets. It is

interesting to know the exfoliation of GNP and sGNP during material processing by observing the change of G/2D ratio, as shown in Table 4.2.

Since the starting material, GNP, was multi-layered graphene, the G/2D ratio was 4.78. Despite the intercalation of silicon groups into the GNP, the ratio of G/2D bands of sGNP (4.74) was not significantly improved compare with that of GNP. In the form of slurry mixture, high shear and planetary mixing prompted GNP and sGNP to become mechanically exfoliated in geopolymer matrix. Thus, the ratios of G/2D of GNP KGP slurry and sGNP KGP slurry were noticeably decreased to 3.57 and 4.14, respectively. After the curing process, the ratios of both GNP KGP and sGNP KGP increased to 4.5, possibly implying that the GNP and sGNP were re-agglomerated during the polymerization and precipitation processes of the geopolymer matrix.

iv. FTIR analysis

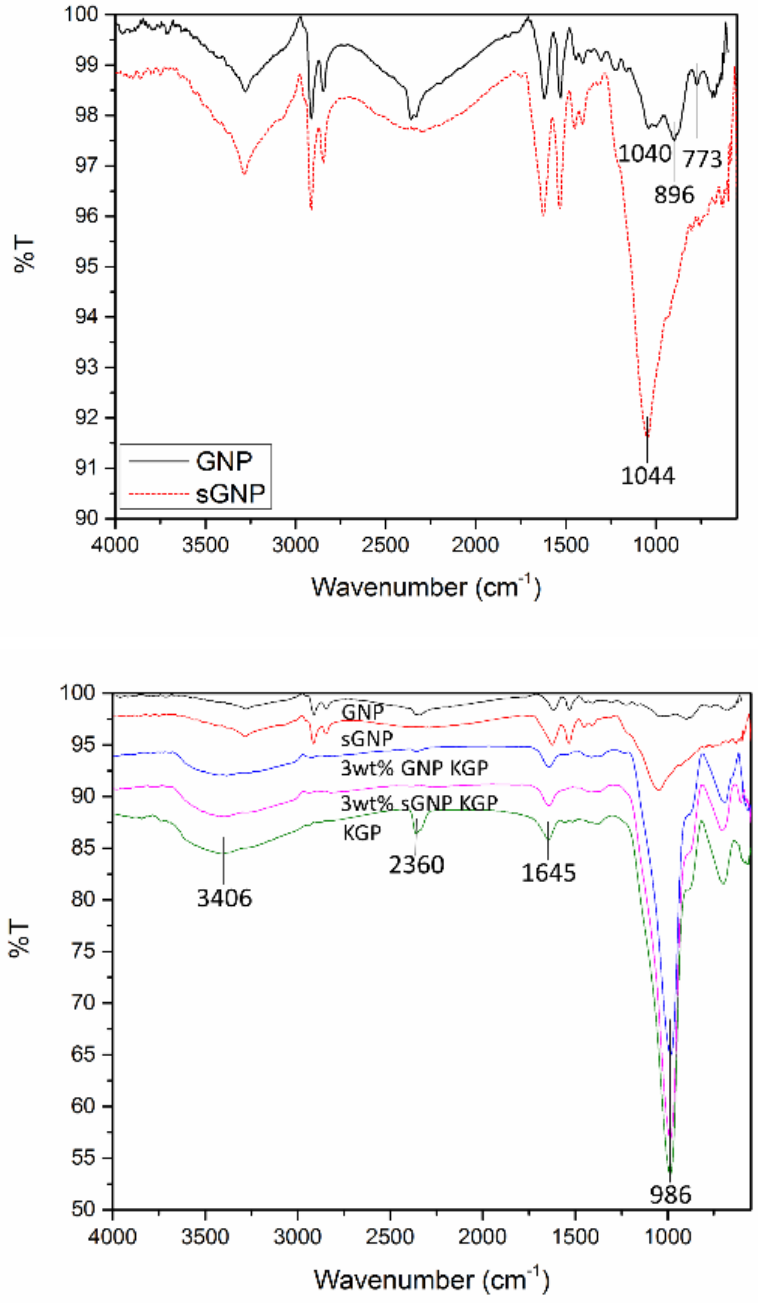

Fig. 4.4. FTIR spectra of GNP, sGNP, 3 wt% GNP KGP, 3 wt% sGNP KGP and KGP.

Fig.4.4 presents IR spectra of as-received GNP and silicon functionalized GNP. The absorption bands on the IR spectrum of the GNP at 1040, 896 and 773 cm^{-1} corresponded to the C-H, C-O and C-C vibration modes, respectively.[25] For the sGNP, the most characteristic IR absorption band around 1044 cm^{-1} was assigned to the Si-O stretching mode and it was superimposed on the other C-H, C-O and C-C bonding peaks. The silicon group of sGNP was clearly observed in this FTIR analysis and it was verified that the functionalization proceeded successfully to form sGNP from GNP.

Moreover, once the GNP or sGNP were embedded into the geopolymer matrix, the IR spectra were dominated by the geopolymer matrix, although the GNP or sGNP were added to the maximum 3 wt%. The dominant FTIR peak of KGP appeared at 986 cm-1 and was attributed to the asymmetric stretching vibration of Si-O-Si or Al-O-Si. Several other peaks at 3406, 2360 and 1645 of KGP corresponded the stretching and deformation vibrations of OH and H-O-H groups from weakly bound water molecules.[26]

b. Mechanical Properties

i. 4 Point Flexure Test with Weibull Statistics

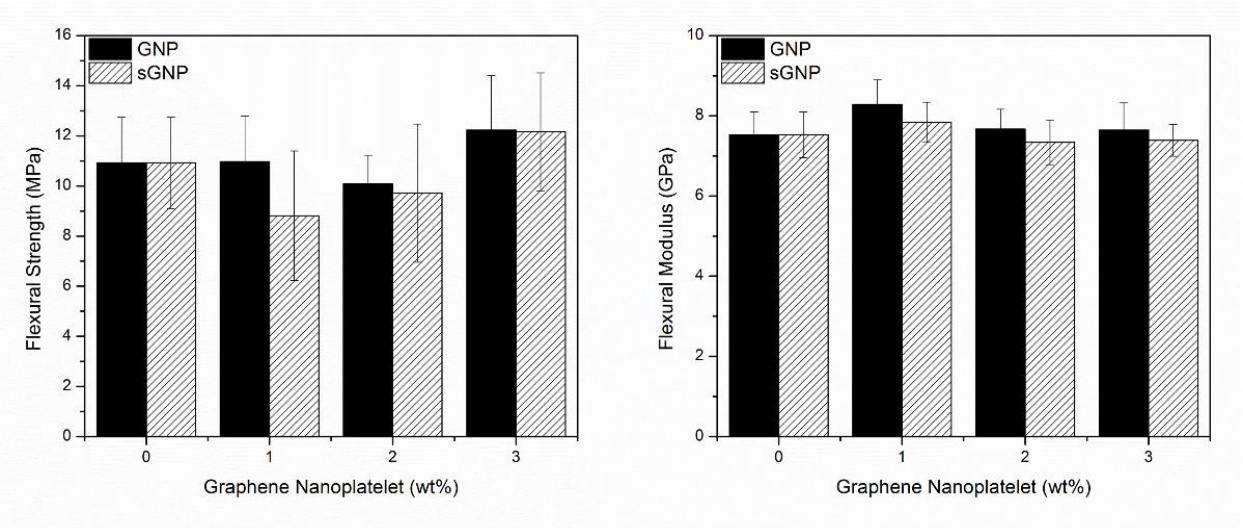

Fig. 4.5. Average flexural strength and moduli of GNP KGP and sGNP KGP

Fig. 4.5 summarizes the average flexural strengths and moduli of GNP KGP and sGNP KGP for the three platelets contents. The error bars were calculated from the standard deviations of more than 20 fracture tests. The pure KGP had a strength of 11 MPa and modulus of 7.5 GPa. The flexural strengths decreased up to 2 wt% of both GNP and sGNP loadings but the 3 wt% of GNP or sGNP enhanced the strengths (12 MPa) again, which followed the typical rule of mixtures. The initial decrease of strength with lower GNP was observed since the small amount of reinforcements behaved like small defects in the geopolymer matrix. The graphene nanoplatelets contents reinforced the composites again and the flexural strengths reached 12 MPa at 3 wt% of platelets contents. The flexural moduli of GNP KGP (8.3 GPa) and sGNP KGP (7.8 GPa) increased by at most 10 % and 4% at 1 wt% loading, compared to the pure KGP. An increase in GNP loadings had no significant effect on the average flexural strengths and moduli of geopolymer composites.

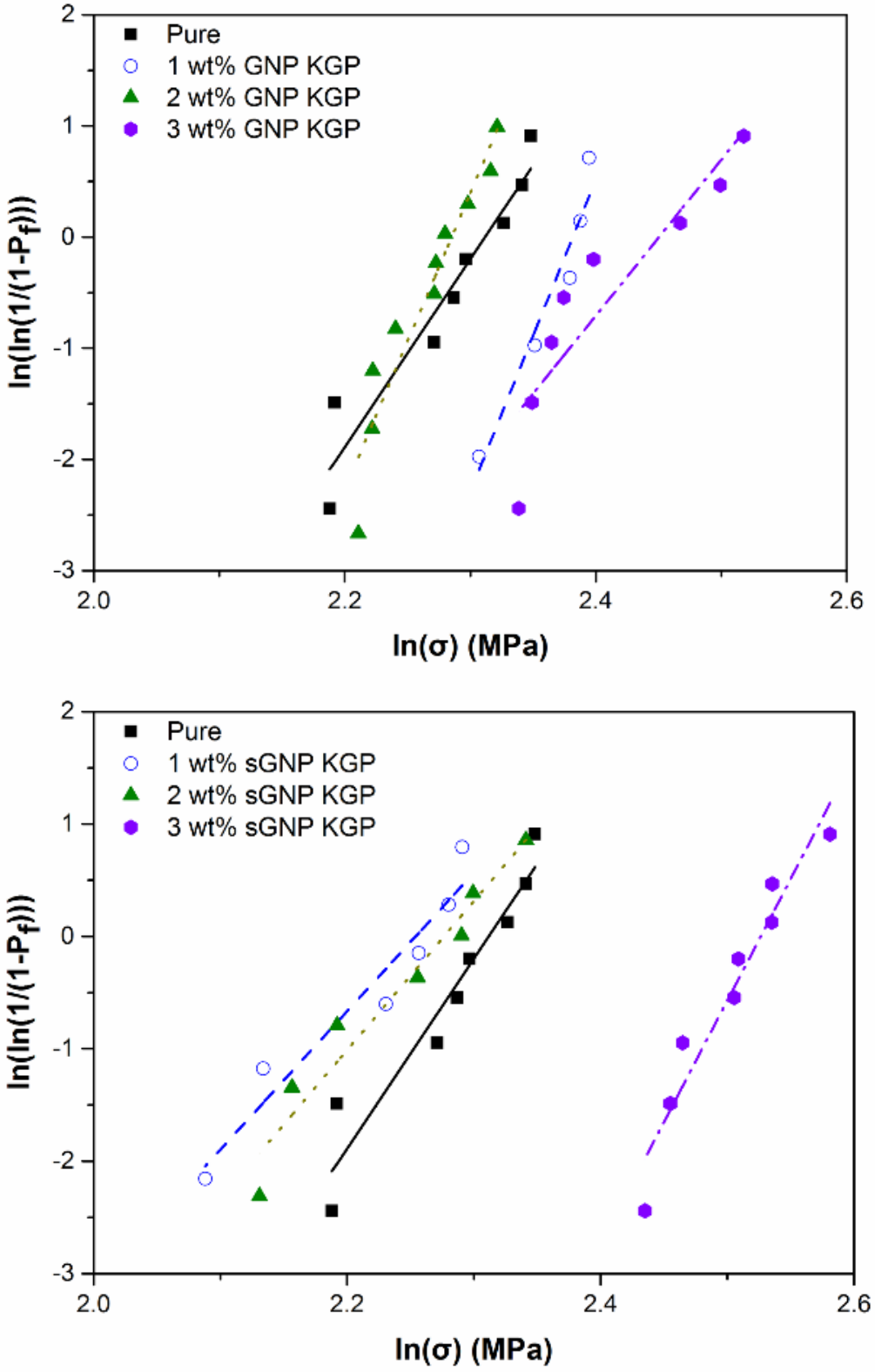

Fig. 4.6. Weibull moduli of GNP KGP and sGNP KGP based on 4-point flexural strengths

Table 4.3. Weibull Moduli m and Characteristic Strength α Measured from Four-point Flexure Testing

	Pure	GNP KGP			sGNP KGP		
		1 wt%	2 wt%	3 wt%	1 wt%	2 wt%	3 wt%
m	17	28	27	14	12	13	22
α (MPa)	10	11	10	12	10	10	13

However, the statistical analyses, Weibull distribution, based on flexure tests gave more information of the effect on the flexural strengths as shown in Fig. 4.6 and Table 4.3. The highest Weibull modulus of 28 and 22 were observed at 1 wt% GNP KGP and 3 wt% sGNP KGP, respectively. Only 1 wt% GNP loading enhanced 10 % of the characteristic strength and 65% of Weibull modulus compared to pure KGP. In addition, the 3 wt% sGNP loading increased the Weibull modulus (29%) and characteristic strength (30%). The Weibull modulus and strengths were determined by the following three factors, the number of platelets, interfacial bonding between platelets and geopolymer matrix, and dispersion of platelets in geopolymer. Since the sGNP were twice heavier than GNP, the number of platelets of sGNP was half of that of GNP at the same weight percent loading. The number of platelets in 3 wt% of sGNP corresponded to the number of platelets between 1 and 2 wt% of GNP loadings and the characteristic strength of 3 wt% sGNP KGP was around 30% higher than 1 and 2 wt% GNP KGP. This indicated that the silicon functionalization enhanced the interfacial boding between GNP and geopolymer and resulted in higher characteristic strength at the same number of platelets. Note that relatively higher number of platelets in 3 wt% GNP KGP showed the lower Weibull modulus due to the nonuniform dispersion of GNP in higher loading which subsequently introduced unremovable voids.

ii. IE test with Halpin-Tsai Modeling

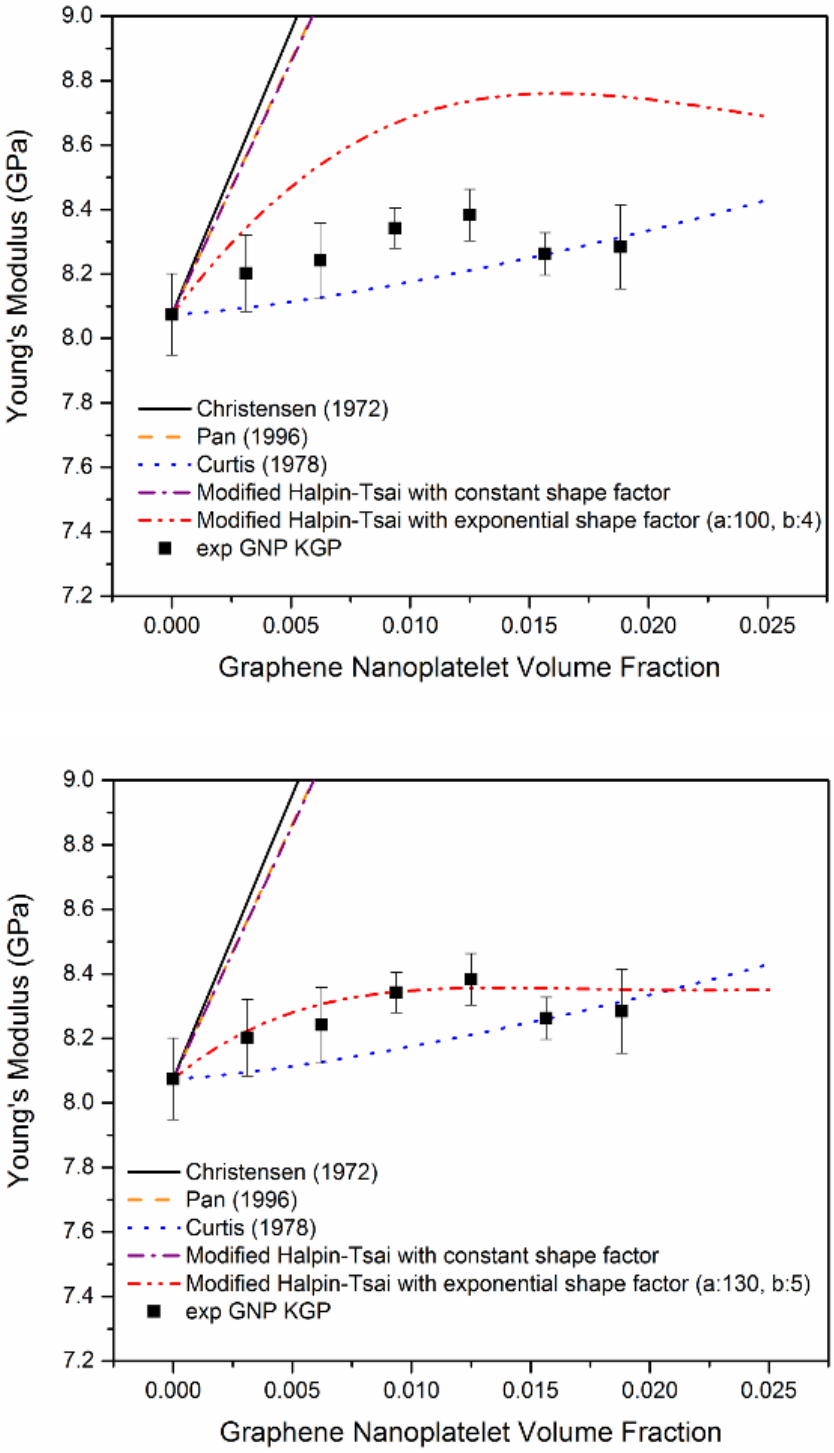

Fig. 4.7. Elastic moduli comparison between theories and experimental results of GNP KGP based on IE test.

The Young's moduli of GNP KGP having different GNP loadings were measured by the impulsive excitation method and theoretical models were compared with experimental results as shown in Fig. 4.7. Since the theoretical models assumed fiber reinforcements, the diameter and length of the fiber corresponded to the thickness and length of platelets in this study. The 0, 0.5, 1, 1.5, 2, 2.5 and 3 wt% GNP loadings were converted to the volume fractions, 0, 0.003, 0.006, 0.009, 0.012, 0.016 and 0.019, respectively. The black dots and error bars corresponded to the average values and the standard deviations of each experimental data sets, respectively. Although the fiber orientation and aspect ratio were considered in various theoretical models, Christensen, Pan, Curtis and modified Halpin-Tsai with constant factor, the nonlinear behavior of experimental results could not be explained by any of those models. However, the exponential shape factor modified the straight line of the Halpin-Tsai model to give a nonlinear expression in the GNP volume fraction considered.[20, 21] In the exponential shape factor, the degree of GNP aggregation, which accounted for the nonlinear behavior of GNP KGP, was related to the constants a and b. Fig. 4.7 shows that the modified Halpin-Tsai equation could model the Young's modulus of GNP KGP composites by varying the aggregation-related constant a, 130, and b, 5, systematically. The Young's modulus decreased above 2 wt% GNP loading due to the aggregation of GNP, which agreed with the decrease in Weibull modulus at 3wt% GNP in the statistical analysis.

c. Electrical and Thermal Properties

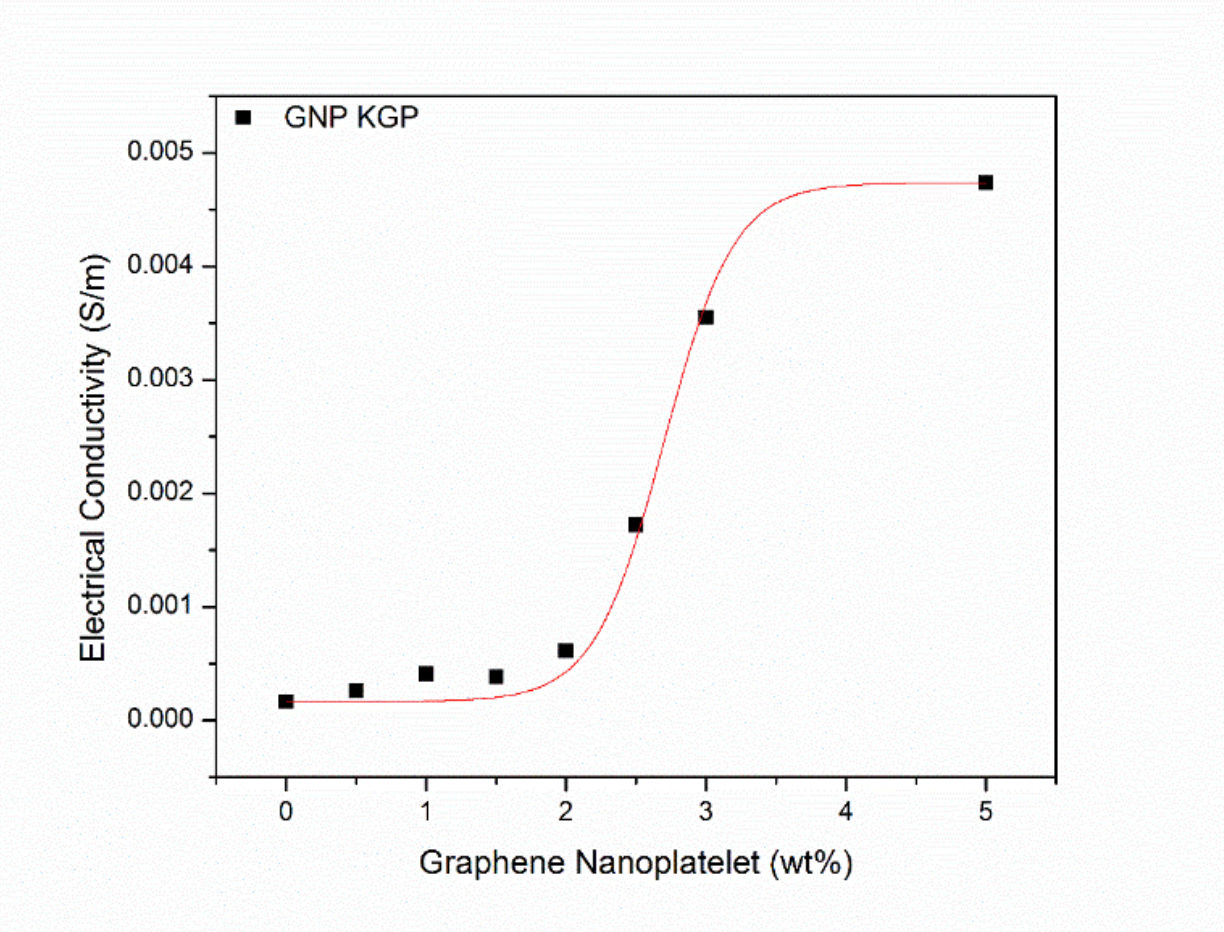

Fig. 4.8. Electrical conductivity of GNP KGP. The electrical threshold was observed from 2 to 3 wt% GNP contents.

Table 4.4. Electrical and Thermal Conductivities of GNP KGP

	Pure	GNP KGP			
		1 wt%	2 wt%	3 wt%	5 wt%
Electrical Conductivity (S/m)	1.66×10^{-4}	4.11×10^{-4}	6.14×10^{-4}	3.55×10^{-3}	4.74×10^{-3}
Thermal Conductivity (W/(m·K))	0.32	0.34	0.37	0.39	N/A

The electrical and thermal conductivities of GNP KGP were measured as a function of GNP contents and are shown in Fig. 4.8 and Table 4.4. The incorporation of GNP into geopolymer matrix continuously increased the electrical and thermal conductivities of GNP KGP

composites. It indicated the GNP was served as a good filler to modify the electrical and thermal conductivities of the geopolymer matrix.

As shown in Fig. 4.8, the electrical conductivity of GNP KGP increased slowly between pure, 1.66 x 10^{-4} S/m, and 2 wt% GNP KGP, 6.14 x 10^{-4} S/m, since the platelets in the geopolymer matrix were not enough to form an effective electrical conductive network. Above 2 wt% GNP loading, the electrical conductivities were significantly increased by more than 20 times compared with that of pure KGP. The percolation threshold is where the electrical conductivity changed suddenly by a few orders of magnitude. Thus, the electrical percolation threshold of GNP KGP lay at around 3 wt% GNP loading. Note that the electrical conductivity of the composite was determined by the following factors, orientation, aspect ratio and dispersion of fillers. The random orientation and aspect ratio of GNP were the same among GNP KGP composites, but the dispersion of GNP in different GNP loadings varied because of the formation of agglomeration at higher GNP loadings. As we have seen the effect of agglomeration in the mechanical properties section, the electrical conductivity at 3 wt% GNP, at the electrical percolation threshold, should have been several orders of magnitude higher rather than 20. In addition, the 5 wt% GNP KGP was prepared by using a different mixing technique, resonant acoustic mixing[27], since the shear and Thinky mixer could mix up to only 3 wt% GNP contents. However, the increase in electrical conductivity at 5 wt% GNP KGP turned slowly again, which was attributed to the formation of defects caused by platelet agglomeration despite the application of resonance acoustic mixing.

The thermal conductivity increased gradually with increasing GNP loadings. The thermal conductivity of 3 wt% GNP KGP, 0.39 W/m·K, increased by 22% compared with that of pure KGP, 0.32 W/m·K. While the electrical conductivity showed a percolation threshold at 3 wt%

GNP loading, the thermal conductivity was not significantly improved at 3 wt% GNP KGP. This could be attributed to the fact that the thermal conductivity of GNP in the perpendicular orientation to the surface, 6 W/m·K was comparable to that of pure KGP. On the other hand, the electrical conductivity of GNP in perpendicular orientation, 10^2 S/m, was still 10^6 times higher than that of pure KGP. Therefore, the heat conductivity improved much less than did the electrical conductivity at 3 wt% GNP loading, where not only the effective conductive network, but also the GNP agglomeration formed.

4. 5 Conclusion and Discussion

The inclusion of graphene nanoplatelets improved the mechanical, electrical and thermal properties of potassium geopolymer. The flexural strengths and their Weibull moduli indicated that the 1 wt% GNP KGP was the optimal composition to achieve the highest Weibull modulus, 28, which was 65% higher than that of pure KGP. The silicon functionalized GNP was also incorporated with KGP to enhance the interfacial bonding and resulted in the highest characteristic flexural strength, 13 MPa, at 3 wt% sGNP KGP with a relatively high Weibull modulus, 22. The elastic modulus of GNP KGP was well fitted by the modified Halpin-Tsai equation having exponential factors (a = 130 and b = 5). The electrical conductivities of GNP KGP were significantly improved at 3 wt% GNP loading, where the electrical threshold was observed. The maximum electrical conductivity was 4.74×10^{-3} S/m at 5 wt% GNP, which was 29 times higher than that of pure KGP. The electrical conductivities of GNP KGP composites remained in the region of a semiconductor. Thermal conductivities of GNP KGP showed a linear increase of up to 0.39 W/mK at 3 wt% GNP contents.

4. 6 References

1. J. Davidovits, "Geopolymers and Geopolymeric Materials," *Journal of Thermal Analysis and Calorimetry*, **35[2]** 429-41 (1989).

2. P. Duxson, A. Fernández-Jiménez, J. Provis, G. Lukey, A. Palomo and J. Van Deventer, "Geopolymer Technology: The Current State of the Art," *Journal of Materials Science*, **42[9]** 2917-33 (2007).

3. A. R. Sakulich, "Reinforced Geopolymer Composites for Enhanced Material Greenness and Durability," *Sustainable Cities and Society*, **1[4]** 195-210 (2011).

4. T. Cheng and J. Chiu, "Fire-Resistant Geopolymer Produced by Granulated Blast Furnace Slag," *Minerals Engineering*, **16[3]** 205-10 (2003).

5. J. Davidovits, "Recent Progresses in Concretes for Nuclear Waste and Uranium Waste Containment," *Concrete International*, **16[12]** 53-58 (1994).

6. B. Latella, D. Perera, T. Escott and D. Cassidy, "Adhesion of Glass to Steel Using a Geopolymer," *Journal of Materials Science*, **41[4]** 1261-64 (2006).

7. W. Kriven, J. Bell and M. Gordon, "Microstructure and Nanoporosity of as-Set Geopolymers," *Mechanical Properties and Performance of Engineering Ceramics II: Ceramic Engineering and Science Proceedings, Volume 27, Issue 2* 491-503 (2008).

8. S. S. Musil and W. M. Kriven, "In Situ Mechanical Properties of Chamotte Particulate Reinforced, Potassium Geopolymer," *Journal of the American Ceramic Society*, **97[3]** 907-15 (2014).

9. V. A. Estani, A. D. Mazzoni and E. F. Aglietti, "Vibrocast Refractories-Influence of Chamotte Grains on Thermochemical Properties," *Refractories Applications and News*, **10[4]** 10-13 (2005).

10. T. Lin, D. Jia, P. He, M. Wang and D. Liang, "Effects of Fiber Length on Mechanical Properties and Fracture Behavior of Short Carbon Fiber Reinforced Geopolymer Matrix Composites," *Materials Science and Engineering: A,* **497[1]** 181-85 (2008).

11. T. Lin, D. Jia, M. Wang, P. He and D. Liang, "Effects of Fibre Content on Mechanical Properties and Fracture Behaviour of Short Carbon Fibre Reinforced Geopolymer Matrix Composites," *Bulletin of Materials Science,* **32[1]** 77-81 (2009).

12. S. Cho and W. M. Kriven , "Short Carbon Fiber-Reinforced, Geopolymer Composites. Part I. Intrinsic Mechanical Properties," *Sumitted; Ceramics International* (2015).

13. M. A. Hasan, S. Cho, K. Remick, A. F. Vakakis, D. M. McFarland and W. M. Kriven, "Primary Pulse Transmission in Coupled Steel Granular Chains Embedded in PDMS Matrix: Experiment and Modeling," *International Journal of Solids and Structures,* **50[20]** 3207-24 (2013).

14. "Granphene Nanoplatelet Data Sheet," *http://xgsciences.com/wp-content/uploads/2012/10/10-15-13_xGnP-M_Data-Sheet.pdf, accessed April 2015*.

15. H. Alkhateb, A. Al-Ostaz, A. H.-D. Cheng and X. Li, "Materials Genome for Graphene-Cement Nanocomposites," *Journal of Nanomechanics and Micromechanics,* **3[3]** 67-77 (2013).

16. S. Cho, R. D. Schmidt, E. D. Case and W. M. Kriven, "Short Carbon Fiber-Reinforced, Geopolymer Composites. Part II. Effect of Fiber Length on Mechanical Properties," *Sumitted; Ceramics International* (2015).

17. R. Christensen and F. Waals, "Effective Stiffness of Randomly Oriented Fibre Composites," *Journal of Composite Materials,* **6[3]** 518-35 (1972).

18. N. Pan, "The Elastic Constants of Randomly Oriented Fiber Composites: A New Approach to Prediction," *Science and Engineering of Composite Mmaterials,* **5[2]** 63-72 (1996).

19. P. Curtis, M. Bader and J. Bailey, "The Stiffness and Strength of a Polyamide Thermoplastic Reinforced with Glass and Carbon Fibres," *Journal of Materials Science,* **13[2]** 377-90 (1978).

20. M.-K. Yeh, N.-H. Tai and J.-H. Liu, "Mechanical Behavior of Phenolic-Based Composites Reinforced with Multi-Walled Carbon Nanotubes," *Carbon,* **44[1]** 1-9 (2006).

21. N.-H. Tai, M.-K. Yeh and T.-H. Peng, "Experimental Study and Theoretical Analysis on the Mechanical Properties of Swnts/Phenolic Composites," *Composites Part B: Engineering,* **39[6]** 926-32 (2008).

22. ASTM, "Standard Test Method for Dynamic Young's Modulus, Shear Modulus, and Poisson's Ratio by Impulse Excitation of Vibration." in West Conshohocken: ASTM International, Vol. **E1876-09** (2003).

23. ASTM, "Standard Test Method for Evaluating the Resistance to Thermal Transmission of Materials by the Guarded Heat Flow Meter Technique." in West Conshohocken: ASTM International, Vol. **E1530-11** (2011).

24. A. Ferrari, J. Meyer, V. Scardaci, C. Casiraghi, M. Lazzeri, F. Mauri, S. Piscanec, D. Jiang, K. Novoselov and S. Roth, "Raman Spectrum of Graphene and Graphene Layers," *Physical Review Letters,* **97[18]** 187401 (2006).

25. G. Chen, W. Weng, D. Wu, C. Wu, J. Lu, P. Wang and X. Chen, "Preparation and Characterization of Graphite Nanosheets from Ultrasonic Powdering Technique," *Carbon,* **42[4]** 753-59 (2004).

26. M. Catauro, F. Bollino, I. Kansal, E. Kamseu, I. Lancellotti and C. Leonelli, "Mechanical and Biological Characterization of Geopolymers for Potential Application as Biomaterials," *AZojomo* (2012).

27. "Reosonant Acoustic Mixer (RAM)," *http://www.resodynmixers.com/technologies/, accessed April 2015*.

CHAPTER 5: LIGHTWEIGHT GRANULAR ACOUSTIC METAMATERIALS FOR STRESS WAVE MITIGATION

5.1 Abstract

Due to their similarity with concrete, geopolymers have been mainly used as structural materials. With documented chemical and mechanical properties of geopolymers, their use could be expanded to applications in many disciplines. In this presentation, geopolymers were used as granular media and displayed interesting dynamic behavior for stress wave mitigation and as acoustic metamaterials. The fabrication of geopolymer beads was achieved by simple injection into a PDMS polymer mold. Based on the mechanical properties of geopolymers, the dynamic responses of homogeneous and dimer chains were theoretically predicted and experimentally investigated under impulse excitation. By substituting metal beads for geopolymer beads which were 6 times lighter, a linear array of lightweight granular media was created to mitigate the effects of a stress wave.

5.2 Introduction

Ordered granular metamaterial was first studied by Nesterenko in 2001 and the use of its dynamics has been extended to diverse fields and applications. Tunable acoustic metamaterials[1, 2] , stress wave trapping[3] , shock mitigation[4] , acoustic filtering[5, 6] , nonlinear acoustic lensing[7, 8] and stress wave tailoring[9, 10, 11] are some of the fields where the strongly nonlinear granular media have been applied. The unique shock mitigation properties has been studied in homogeneous granular metamaterials due to their zero (nearly zero) speed of sound, 'sonic vacua'.[12, 13] These shock absorption properties of granular media has the capability to be applied in protecting electronic devices, acoustic filters, vibration isolation and stress wave mitigation. The theoretical studies of granular metamaterials has been conducted by many researchers in the field of nonlinear dynamics.[12, 14, 15, 16] Granular media is strongly nonlinear due to Hertzian interactions between beads. The zero velocity of granular media, which defined in linear acoustics, is developed during collisions between beads in the absence of compression after initial excitation of a granular chain where the separation of beads took place. Such complete nonlinear properties of granular media can be utilized in novel designs of acoustic granular metamaterials.

The form of granular media has been considered in various configurations such as one dimensional homogeneous chains with[17] or without a matrix[13] , two dimensional chains with[17] or without a matrix[18] , dimer chains with the same material but different sizes of beads[19] and dimer chains with different types of beads with or without matrix.[20] From the homogenous one dimensional chain, the theoretical analysis has been developed to account for the nonlinear dynamics of granular media. Based on nonlinear modeling, the dynamics of two dimensional granular media has been studied by numerical simulations and verified by experiments.[18] For real material formation of granular media, the bead chains were embedded in a certain matrix while

the point contacts of adjacent beads were preserved. The effect of energy absorption of granular media with a surrounding matrix has been studied analytically and experimentally.[17] For further enhance of attenuation in a granular chain, a dimer chain (different mass ratio by different sizes of stainless steel beads) was proposed and verified higher energy dissipation took place in dimer chain compared to that of a homogeneous chain.[19] However, the different size of beads in the dimer required a complicated manufacturing process and limited the use of dimer chains in other applications. Therefore, a dimer chain composed of the same size of different types of beads were proposed and incorporated in to the matrix to construct a more practical granular metamaterial. The effect of mass ratio on the transmitted forces was investigated by experiment and numerical simulation.[20] In the previous study, the de-convolution method was developed to get the real response of chains by extracting the dynamics of a force transducer itself. Taking this advantage of the de-convolution process, the further systematic study of intrinsic nonlinear dynamics of dimer chains composed of different materials, especially geopolymer (6 times lighter than stainless steel), can be carried out. In this work, we used five different beads (aluminum, zirconia, alumina, geopolymer and polyethylene) as light beads in a dimer chain and fixed the heavy beads to be stainless steel beads.

The geopolymer beads were created by a simple injection method into polymer mold and substituted for stainless steel beads to construct granular media. The wave propagation of geopolymer chain was verified by measuring the transmitted forces of a one dimensional homogeneous geopolymer chain and by comparing the force profile with an aluminum bead chain which is well known material which forms a solitary wave under impulse excitation. The absorption or dissipation behavior of different types of dimer chains under same input force and velocity were investigated experimentally and further analyzed by considering the weight of beads

in order to achieve lightweight granular metamaterials where the strongly nonlinear dynamics are conserved.

5.3 Experimental Procedures

a. Sample Preparation

i. Stainless Steel Beads Chain Embedded in a Matrix

Fig. 5.1. Stainless steel granular chain embedded in PDMS matrix with a fixed later gap, 1.5 mm.

Two sets of bead chains were fabricated, one being the excited chain and the other the absorbing chain. Poly-di-methyl-siloxane (PDMS, Sylgard 184) matrix was used to embed Type 302 stainless steel beads (McMaster Carr, 9291K31). The PDMS was used as a matrix material since its mechanical properties have been well studied.[21, 22] Dow Corning® Sylgard® 184 silicon elastomer came in a two-part kit, consisting of a base and a curing agent, in a weight ratio of 10:1. Since a varying ratio of the two components changes the mechanical properties of PDMS, the 10:1 ratio was fixed for all of the samples.[22] The base and curing agent were mixed for 5 minutes during which air bubbles were created inside the PDMS. Hence the PDMS were placed in a desiccator under 508 torr vacuum for 20 minutes in order to degas the PDMS before pouring it into the mold. For each chain, 11 stainless beads were aligned and fixed in the one-dimensional mold. As the stainless steel beads were conductive, contact between all the beads in the mold was verified by

measuring the resistance of each chain with a digital multimeter. Degased PDMS was poured into the mold and cured at room temperature for 48 hours. Higher curing temperatures were avoided as stainless steel beads expanded at high temperature and resulted in subsequent misalignment within the mold.

After the exciting and absorbing chains were fabricated separately, they were joined laterally leaving gaps between the two chains of 0.5, 1.5 or 2.5 mm, respectively. The uncured PDMS adhesive method was used to fill the lateral gaps between the cured PDMS chains and give the highest bond strength without recourse to any special surface treatments.[23, 24] The PDMS adhesive layer filling the separation gap was also cured at room temperature for 48 hours, again in order to avoid thermal expansion and misalignment of stainless steel beads. Finally, multi-meter measurements of both the excited and absorbing chains again verified that the beads remained in contact with their neighbors in a row throughout the whole manufacturing process.

ii. Geopolymer Beads

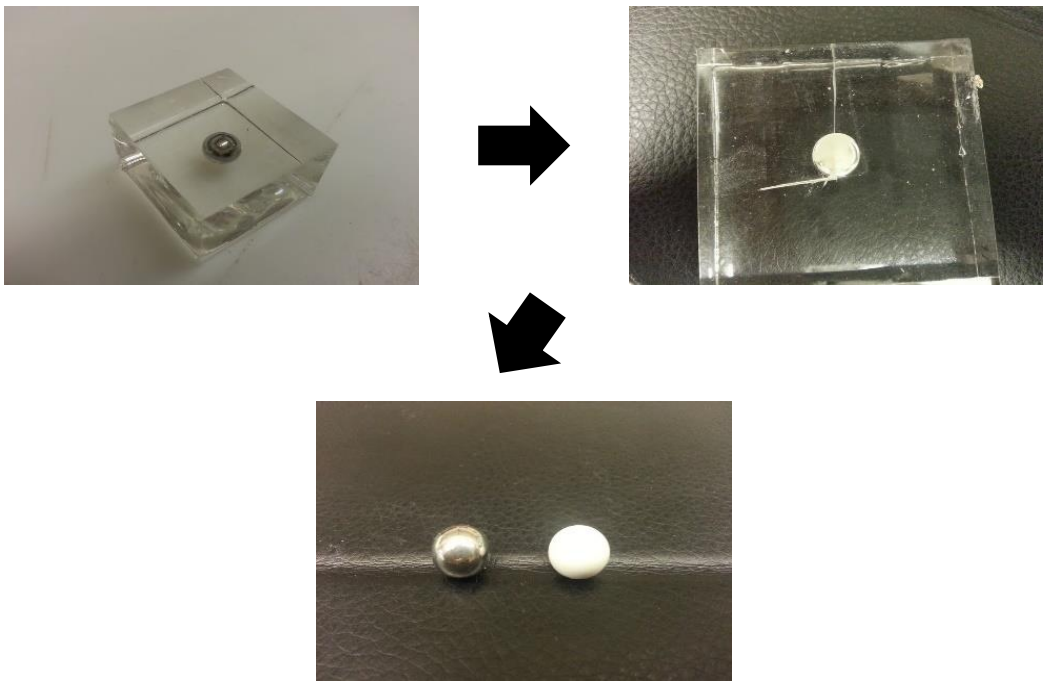

Fig. 5.2. Fabrication process of geopolymer beads by simple injection molding in a PDMS mold.

The process of making a geopolymer bead was described in Fig. 5.2. The stainless steel bead was enclosed by the PDMS and it was placed in an oven at 100 ℃ for 1 hour to harden the PDMS. After curing the PDMS, the stainless steel was removed by cutting the PDMS mold in half and geopolymer slurry was injected through a syringe while the mold was held by a clamp. During injection, the slurry should be injected slowly so as not to introduce any bubbles inside the beads. The mold was sealed by tapes and wraps to protect any air diffusion into the beads and it was placed in the oven at 50 ℃ for 24 hours in order to cure geopolymer during this time. After the curing, the geopolymer bead was taken out from the PDMS mold and dried for 7 days. The PDMS mold could be re-used to make more geopolymer beads. As shown in Fig. 5.2, the size of the beads were the same as the original size of the stainless steel bead and the surface of the geopolymer bead was smooth and clean. This explains why the geopolymer could be easily

detached from the PDMS surface since the PDMS is inherently a hydrophobic material which could not make a bond with the geopolymer slurry (11 moles of water). Sometimes, craters were observed at the surface of beads due to the diffusion of water during curing and drying. PDMS had a lot of advantages as a mold for geopolymer due to its flexibility, repeatability, hydrophobicity and less curing time. Therefore, combining the ease of the geopolymer process with a PDMS mold significantly improves the manufacturing process of complex shapes not only beads.

The purpose of creating geopolymer beads was to substitute the heavy metal beads in a granular chain in order to reduce the weight of the material while the dynamics of granular media was preserved using geopolymer. Thus, the transmitted forces through geopolymer granular media were experimentally measured and will be described later in this paper. Moreover, the granular effect was modeled and simulated based on the theoretical model. In order to model and predict the response of granular media, the material properties of density, Young's modulus, and Poisson's ratio, should be provided. Our previous work[25] indicated that the density, elastic modulus and Poisson's ratio of potassium geopolymer were 1.36 g/cc, 8 GPa and 0.2, respectively.

iii. Other Beads (except Geopolymer beads)

The same size (9.5 mm) but different types of beads beside stainless steel (S.S) were used to change the density ratio of dimer chains (heavy-light-heavy-light) in order to investigate the effect of dimers in energy absorption. For the metal, aluminum beads (A.L) were used as a light bead in the dimer chain. For the ceramic, commercially available zirconia (zirconium oxide, Z.O) and alumina (Al_2O_3) were substituted for the stainless steel beads. As we mentioned above,

the geopolymer beads were used as a light bead and polyethylene (P.E) bead was also used as a polymer bead. The properties and mass ratios to stainless steel are listed in Table 5.1.

Table 5.1. Properties of Beads

Material	Density (g/cc)	Young's modulus (GPa)	Poisson's ratio	Mass ratio (ε)
Stainless steel	8.06	193	0.30	1
Aluminum	2.7	69	0.32	0.33
Zirconia	5.68	205	0.30	0.70
Alumina	3.95	215	0.21	0.49
Geopolymer	1.36	8	0.20	0.17
Polyethylene	0.96	0.8	0.50	0.12

b. Test Method

i. Displacement Measurement by Laser

1. Double Chains for Energy Transfer

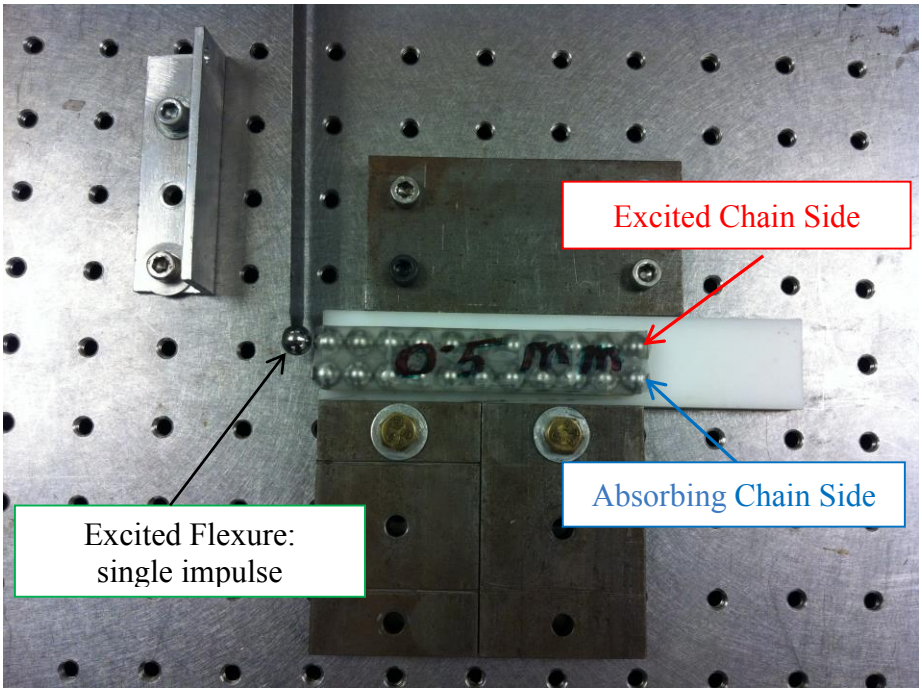

Fig. 5.3. Experimental set up of double stainless steel beads chains embedded in PDMS matrix.

The experimental set up for double chains is shown in Fig. 5.3. The double chains, stainless steel embedded in PDMS matrix, were placed on the top of a Teflon sheet and free on both sides to have free boundary conditions. An impulse excitation was applied to the first bead of the excited chain and two laser vibrometers were focused at the end beads of each chains to measure the displacement under the impact. Two different levels of small inputs, 0.29 m/s and 0.41 m/s, were applied to the excited chain without inducing the rigid body motion of the sample. In order to ensure the repeatability of the experimented results, more than 10 experimental trials were performed for each input level of excitation. The granular chains embedded in the PDMS matrix showed the nonlinear energy exchange phenomenon and the energy transfer in the embedded double chains was analyzed by directly measuring the velocities of the last beads of both in the excited as well as in the absorbing chains. In addition, the amount of energy transferred between chains was measured in three different lateral gap specimens.

ii. Force Measurement by a Force Transducer

1. Sliding Bead Input

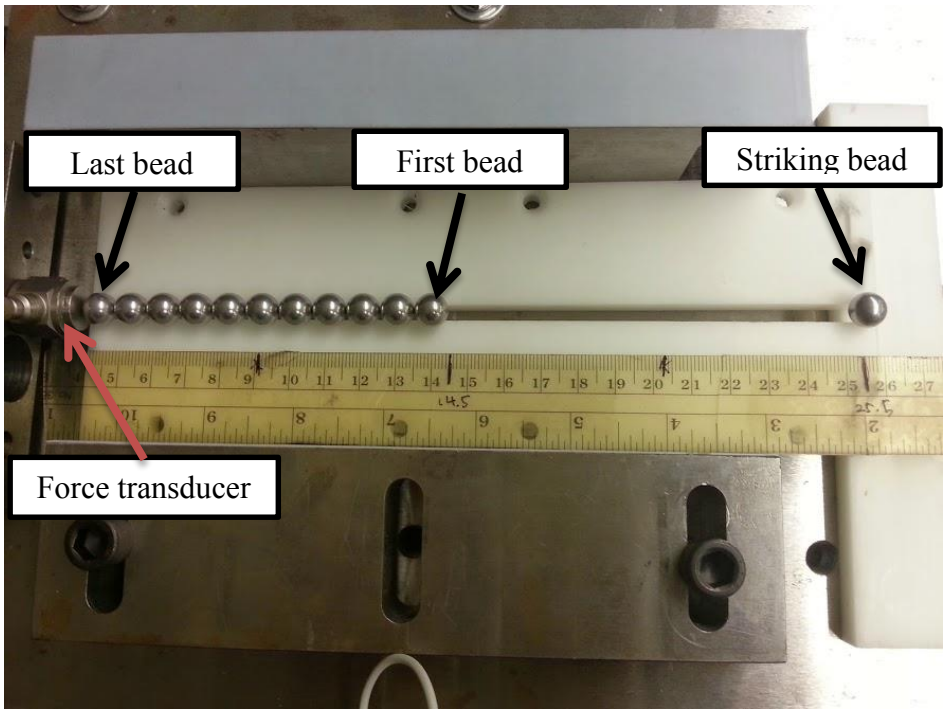

Fig. 5.4. Experimental set up of a sliding bead test.

Fig. 5.4 shows the configuration of the sliding beads test. The 11 beads were placed on leaning Teflon plates and the striking beads were slid down to the end of bead chain. The minimum contacts between beads and Teflon were considered to reduce the friction effect. The striking bead slid down with a speed of 0.22 m/s and hit the first (right-most) bead in the chain thus providing an impulse excitation. The other end (left-most) bead was placed at the force transducer to measure the transmitted force of the granular chain. The force signal was sent to a 24-bit m+p international VibPilot data acquisition system in order to visualize the transmitted force. The force sensor was attached to a rigid body which was fixed on the table. The velocity of the striking beads was calculated by assuming no friction between beads and Teflon plates.

Moreover, no energy loss from the imparting bead to the first bead was assumed. Therefore, the velocity of the first bead was the same as the velocity of the striking bead as calculated based on its travel length (vertical height: 2.5 mm).

2. Free Drop Input

The vertical chain of 11 beads was studied in this work in order to investigate the nonlinear granular effect for stress wave mitigation as shown in Fig. 5.5. The diameter of beads (D), the height of channel (h_2) and the gap between channel and transducer (h_1) were 9.525, 152.5 and 4.5 mm, respectively. From its dimension, the travel length of the striking bead (L) was determined as 42.7 mm which corresponded to a velocity of 0.92 m/s. The gap between Teflon channels to beads was less than 100 micrometers, so that the beads were the well aligned and the striking beads dropped freely. Therefore, with no energy losses from striking bead, the initial velocity of the first bead (top) was relatively more accurate than that attained from the sliding bead setup. In this study, the striking bead was fixed as a stainless steel bead and the main beads (top and bottom) of the dimer chain was also stainless steel. With five different beads described in Table 5.1, dimer chains based on stainless steel beads were constructed and tested as shown in Fig. 5.5.

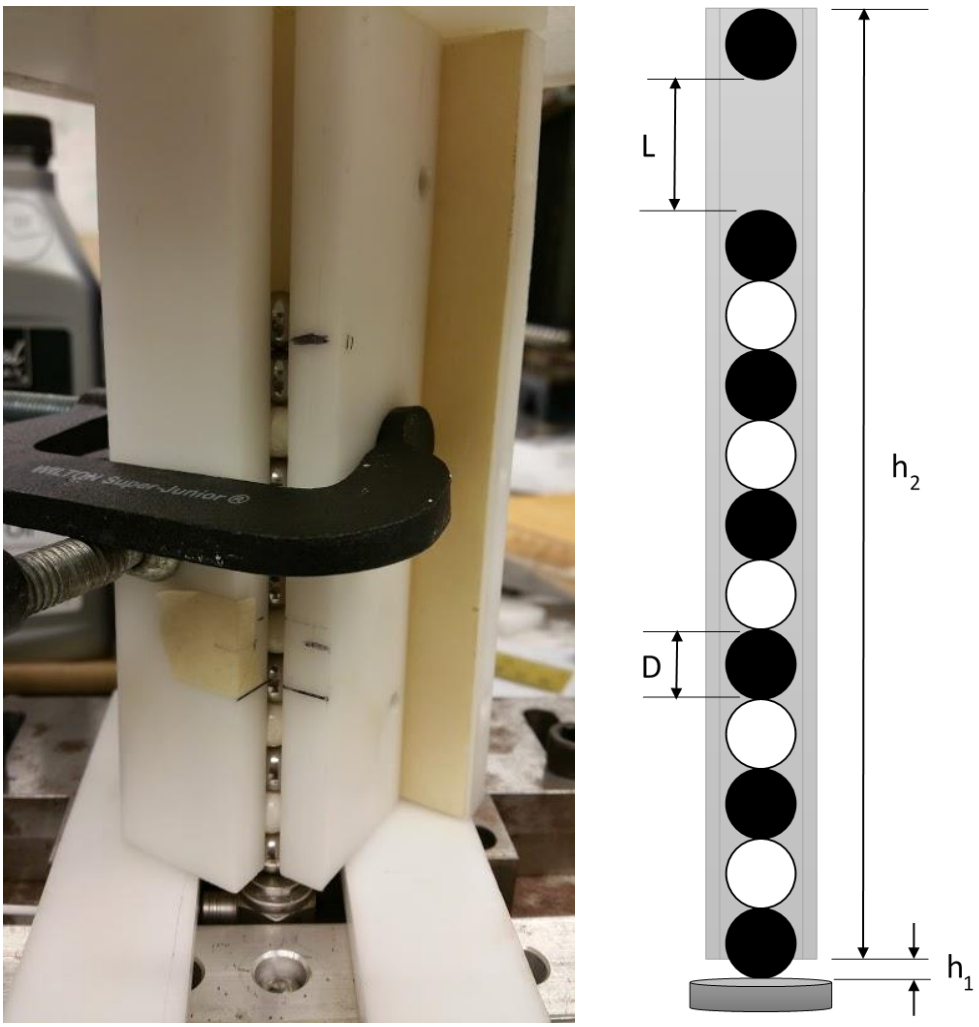

Fig. 5.5. Experimental set up and schematic view of free drop test.

5.4 Results

a. Double Chain with Different Lateral Gaps

As shown in Fig. 5.1, the two rows of granular chains embedded in PDMS matrix and the energy transfer and redirection through the matrix were experimentally investigated in this work. First of all, the propagation of a solitary-like wave was observed in a single chain to verify the strongly nonlinear dynamics due to the Hertzian interaction between adjacent beads and possible

bead separation under collision between neighboring beads. By fitting numerical simulation to the experimental results of a single embedded chain, the numerical parameters such as k_1 (the stiffness coefficient of the linear elastic foundation between beads and the Teflon wall due to the surrounding PDMS matrix), γ (the stiffness coefficient of the axial coupling element between neighboring beads due to the surrounding PDMS matrix), λ_1 (the viscous damping coefficient from interaction of the granular bead with the embedding matrix) and λ_3 (viscous damping coefficient between neighboring beads during Hertzian interaction) were optimized and determined.[17]

From the optimization process to determine the parameters of a single embedded chain, more complex models (two chains with PDMS matrix in this study) could be analyzed in the same way. The two chains were connected by the surrounding PDMS matrix, thus two parameters, k_2 (linear coupling coefficient) and λ_2 (viscous damping coefficient), needed to be identified as shown in Fig. 5.6. In order to study the effect of lateral gap on energy transfer, three specimens with lateral gaps of 0.5, 1.5 and 2.5 mm were prepared and tested. Therefore, the three different values of k_2 and λ_2 should be determined for each specimens. The higher value was observed at lower lateral gap, thus the 0.5 mm showed the highest linear stiffness compared to other lateral gaps while the damping coefficients were almost the same in specimens. The detail of the optimization process and the values of parameters were more fully described in our previous paper.[17]

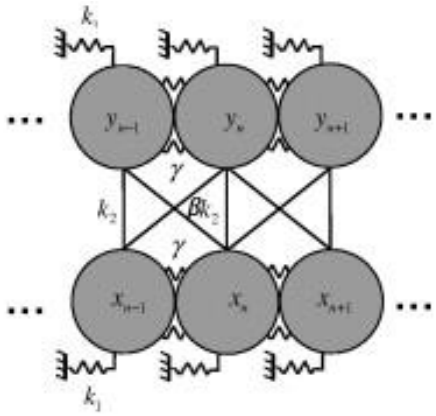

Fig. 5.6. Theoretical model for primary pulse propagation in two weakly coupled granular chains mounted on weak linear elastic foundations.

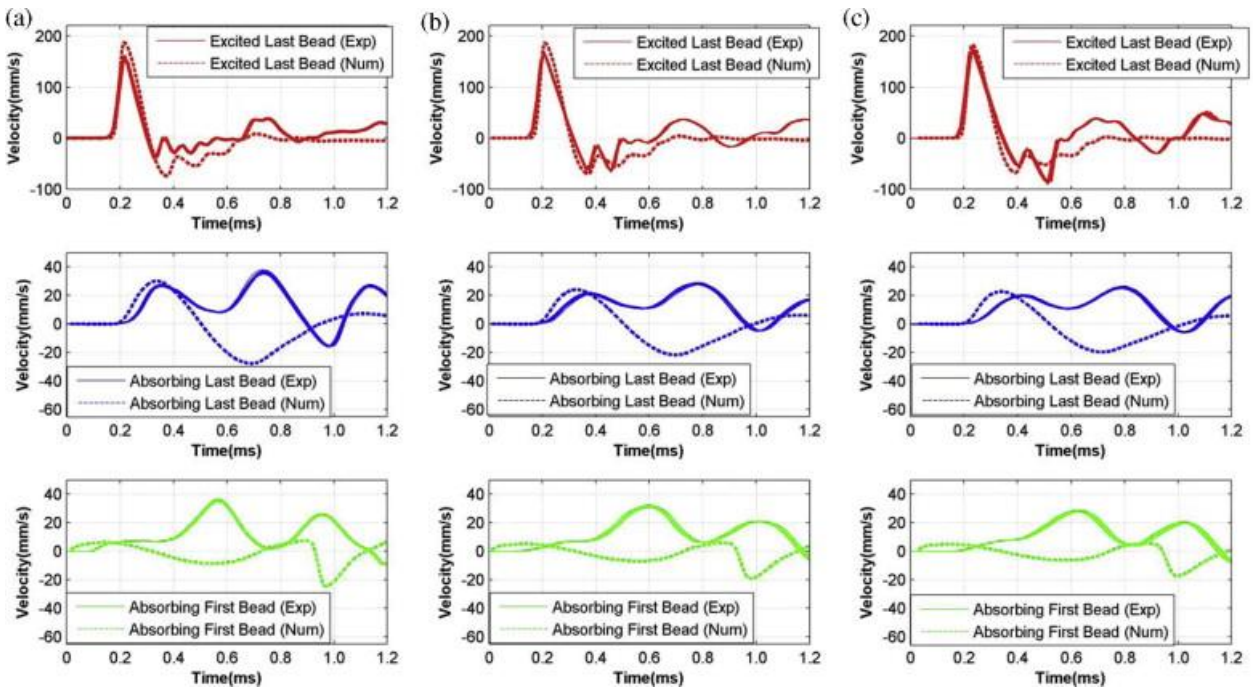

Fig. 5.7. Comparisons between experimental results and simulations for the velocity responses of each set of chains at low excitation, 0.29 m/s. (a) lateral gap: 0.5 mm, (b) lateral gap: 1.5 mm, (c) lateral gap: 2.5 mm

Fig. 5.7. showed the comparison between experimental results and simulation in different lateral gap specimens. The input of these tests was fixed as 0.29 m/s which was low excitation and

all of the samples showed the same phenomena that the excited chains had higher velocity peaks than absorbing chains. In detail, the peak velocity of the excited chain of 2.5 mm lateral gap was higher than that of 0.5 mm, whereas the velocity of the last bead of the absorbing chains of the 2.5 mm lateral gap was lower compared to the 0.5 mm chain (a and c). These indicated that the increase of lateral gap between excited and absorbing chains resulted in the weakening of coupling between two chains. Thus, the energy transfer from excited chain to absorbing chain decreased. Subsequently, the velocity of the last beads of the absorbing chain decreased as the lateral gap increased for the same level of excitation, 0.29 m/s.

These effects of energy transfer were further confirmed by comparing the excited chain response to that of the single embedded chain. The velocity of last bead of the excited chain was higher at 1D chain compared to all three lateral specimens. It clearly indicated that energy was transferred from the excited chain to the absorbing chain through the PDMS matrix. As we described in the optimization process, the quantitatively studied coupling parameters could simulate the effective coupling of PDMS matrix to transfer the energy from the excited to the absorbing chain. The coupling stiffness, K_2, varied nonlinearly with the later gap between chains.

In addition to the energy transfer through the matrix, additional parametric studies were performed and subsequently predicted that an 11 times stiffer matrix would end up with equi-partitioning of energy between excited and absorbing chains for low excitations (0.29 m/s). As the later gap increased, the stiffness of the matrix increased by up to 16 times at 2.5 mm lateral gap to achieve 50% of energy transfer from the excited chain. This multiple of nominal K_2 values was varied with the level of excitations (0.29 m/s and 0.41 m/s). Higher excitation required a stiffer matrix to reach the energy equi-partitioning between chains. Therefore, the

harden PDMS (hPDMS, 9 MPa)) would be the most possible material to substitute for the PDMS (0.9 MPa), in order to observe the energy equi-partition experimentally.

b. Single Chain

i. Sliding Bead Input

The two granular chains within a PDMS matrix transferred the impact energy from the excited chain to the absorbing chain, so that the energy taken into the excited chain was reduced compared to the 1D granular chain within PDMS matrix. For stress wave mitigation, granular media enclosed in a matrix effectively reduced the excited energy by directing the energy to other chains. Furthermore, the optimized stiffness of the matrix could transfer half of the excited energy to the other chain. This effective and customizable energy transfer could be enhanced by using a dimer chain as well as the beads in the matrix.

In addition to the matrix enclosed granular system, the dimer effect of the granular chain without a surrounding matrix has been analyzed and the highly effective energy absorption was also observed experimentally. The mass ratio of beads (alternating heavy and light) played an important role to achieve the minimum energy transfer and highest energy absorption. Previous studies have used the same material (stainless steel beads) with different sizes to change the mass ratio, ε, but it resulted in a difficulty to manufacture process. Therefore, two types of beads with different density but in the same size, 9.525 mm, have been used to vary the mass ratio and to observe the dimer effect on energy absorption.

As we describe above, the main beads (striking, top and bottom beads) were stainless steel and five different types of beads (aluminum, zirconia, alumina, geopolymer and polyethylene) were inserted between the stainless steel beads to construct the dimer chain having

various mass ratios (density ratio in this case). Except for the geopolymer bead, other metal, ceramic and polymer beads were commercially available. The purpose of this work was to substitute the stainless steel bead chain for geopolymer beads in order to construct a lightweight and effective dimer chain as well as compare the effect of energy absorption to other types of beads. Since geopolymer is a relatively new and unknown material, the behavior of wave propagation through geopolymer beads should be investigated prior to construct the dimer chain containing geopolymer beads.

By the sliding bead input test, the response of 11 geopolymer bead chains was experimentally measured using a force transducer and compared with aluminum and polyethylene beads chains. One dimensional homogeneous chains consisting of 11 beads were aligned on a Teflon plate as shown in Fig. 5.4. For this experiment, the striking bead and the beads of the homogeneous chain was matched so that the geopolymer beads chain was excited by a geopolymer bead. The force of the striking bead was fixed at 6 N and the profiles of the input force are described in Fig. 5.8. A single bead slid down and hit the force transducer, so that the force transducer measured the force profile of the single bead excitation. The numerical simulation was also conducted for material properties, density, elastic modulus and Poisson's ratio. As shown in Fig. 5.8, the simulation was well matched to the experimental results for aluminum and geopolymer. The width and height of the input profile from the transducer exactly matched the simulation results. Thus, it confirmed that the models for this type of nonlinear bead interactions were correctly designed and analyzed quantitatively by numerical simulation. However, the experimental results for the polyethylene input did not fit the simulation since the simulation excluded the damping effect between a striking bead and the force transducer where

high damping was introduced due to the low elastic modulus of the polyethylene beads compared to the stainless steel force transducer.

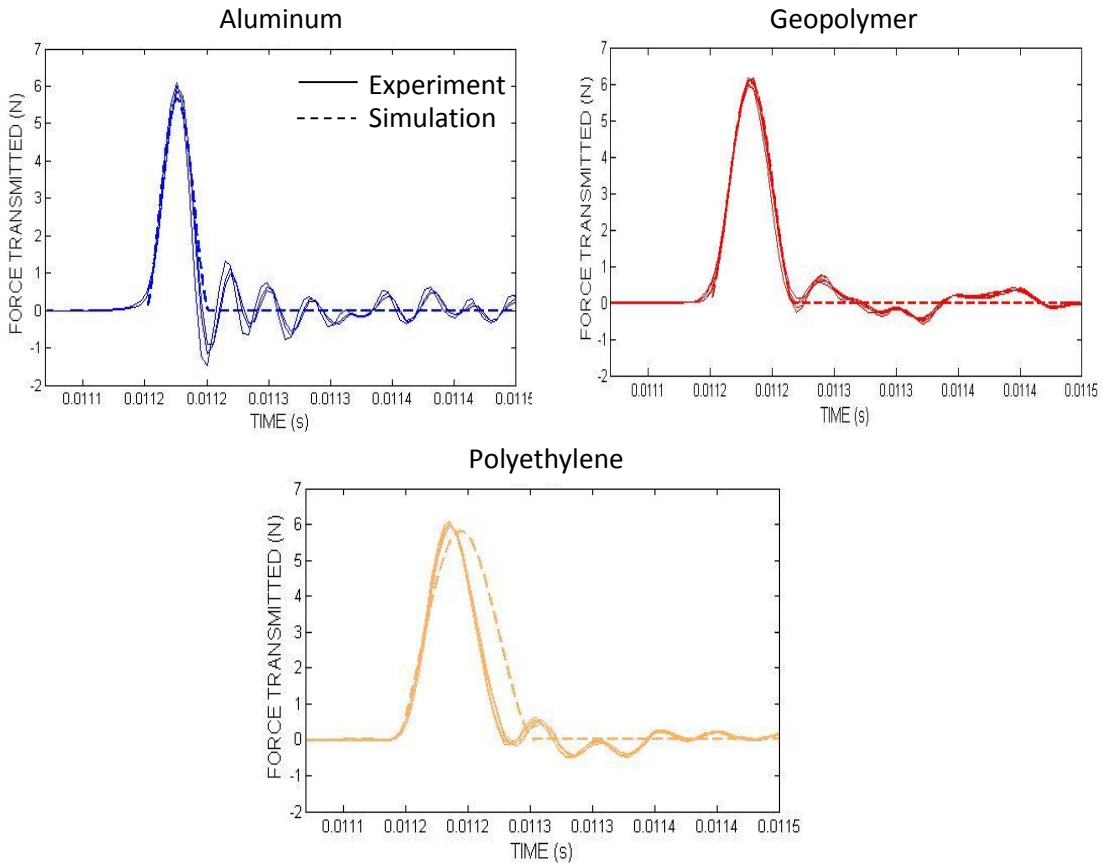

Fig. 5.8. Comparisons between experimental results and simulations of fixed sliding input, 6N, by different beads.

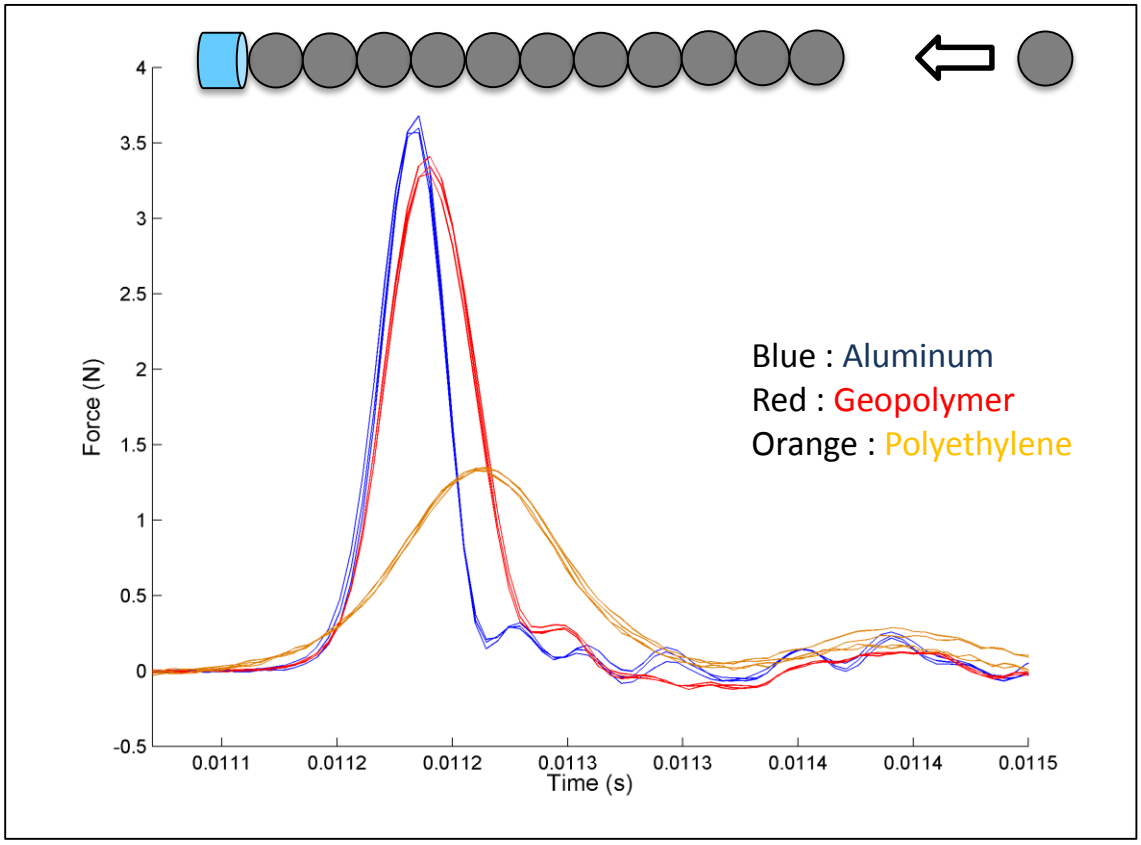

Fig. 5.9. Experimental results of transmitted forces of homogeneous chains with different beads under fixed sliding input, 6N.

The homogeneous chains with three different types of 11 beads were tested by the sliding input method and the transmitted forces were measured by a force transducer and are described in Fig. 5.4. for comparison. First of all, the energy was reduced through the homogeneous chain from 6 N to around 3.5 N for both aluminum and geopolymer and to around 1.3 N for the polyethylene bead chain. The width of the force profile indicated the formation of a solitary wave in the granular chain which meant that nonlinear dynamics of granular media could be

applied to predict the response of the homogeneous chain. As shown in Fig. 5.9. the blue, red and orange lines indicated the profiles of transmitted forces of aluminum, geopolymer and polyethylene bead chains, respectively. The profile of geopolymer beads (the width and height of first peak) was comparable to the aluminum beads rather than that of polyethylene due to the low elastic modulus and high damping properties of the polymer beads. This indicated that the solitary-like wave form in the geopolymer chain as the metal beads chain did and the modeling of granular media based on the metal beads could be applicable to the geopolymer beads chain as well. Note that the polymer chain had the lowest transmitted force in the same excited force which meant that the most energy absorption took place in the chain. However, the width of the first peak was almost twice wider than that of the aluminum bead chain and indicated that the solitary-like wave was not formed and the dynamics of polymer beads would be quite different from that of metal or geopolymer beads.

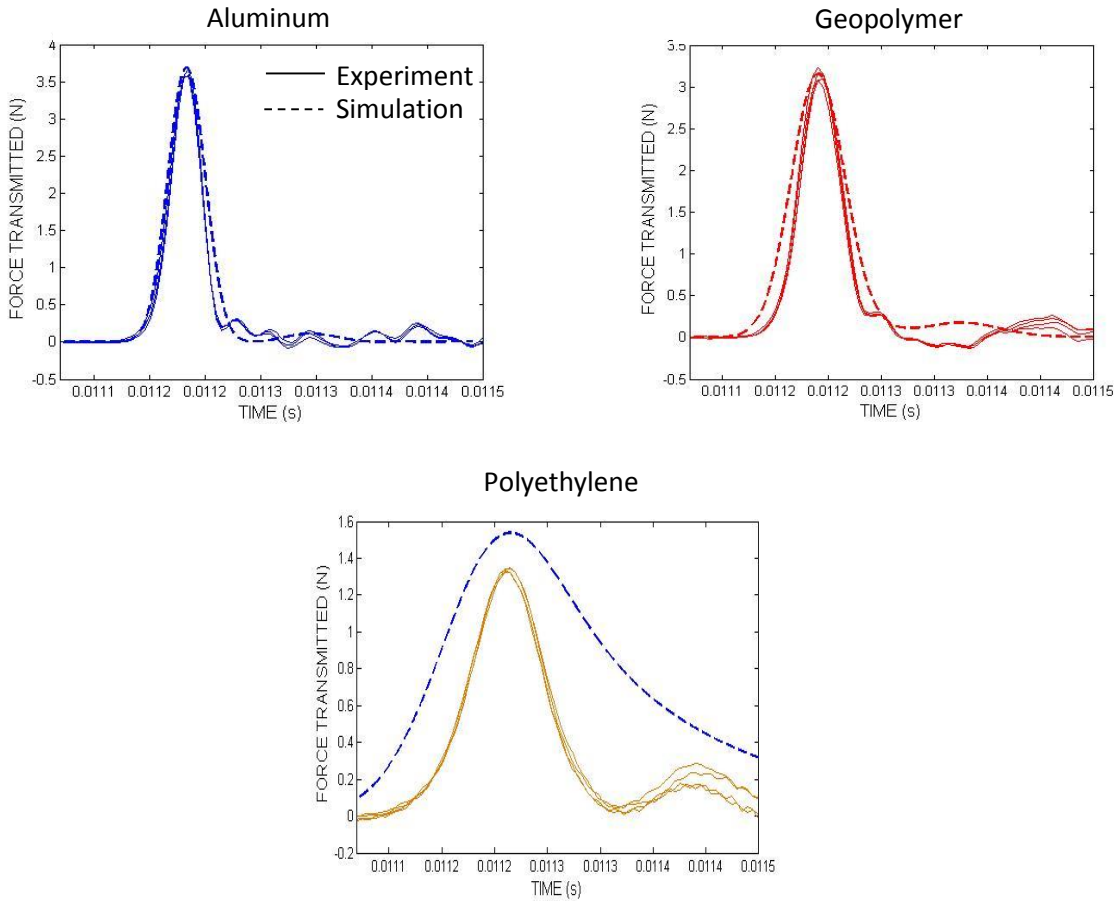

Fig. 5.10. Comparisons between experimental results and simulations of transmitted forces of homogeneous chains with different beads under fixed sliding input, 6N.

In Fig. 5.10, both experimental results and numerical simulations are shown and compared for 11 homogenous bead chains. The solid line and dashed line indicate experiment and simulation, respectively. As we have seen in the profile of input forces in Fig. 5.8, the numerical simulations for transmitted forces were well matched to the aluminum and geopolymer bead chains as well. In order to fit the simulation to experimental results, damping between beads was introduced and numerically determined. Many nonlinear dynamics for granular media do not consider the damping between beads since the main beads in those studies were stainless steel which has a relatively high elastic modulus and low damping. In our study,

we used different beads having a relatively lower elastic modulus than stainless steel beads, so that the damping effect of beads should be accounted for in the discrepancy between simulation and experiment. By doing this, the damping values of aluminum and geopolymer bead chains were 2.55 and 1.31 Ns/m, respectively. Despite the effort to match the simulation to the experimental data, the polyethylene beads chain could not be fitted to any values of damping. This indicated that the current model of granular media could not be applied to polyethylene bead chains and needed to be modeled differently for metal and geopolymer bead chains for a more quantitative analysis.

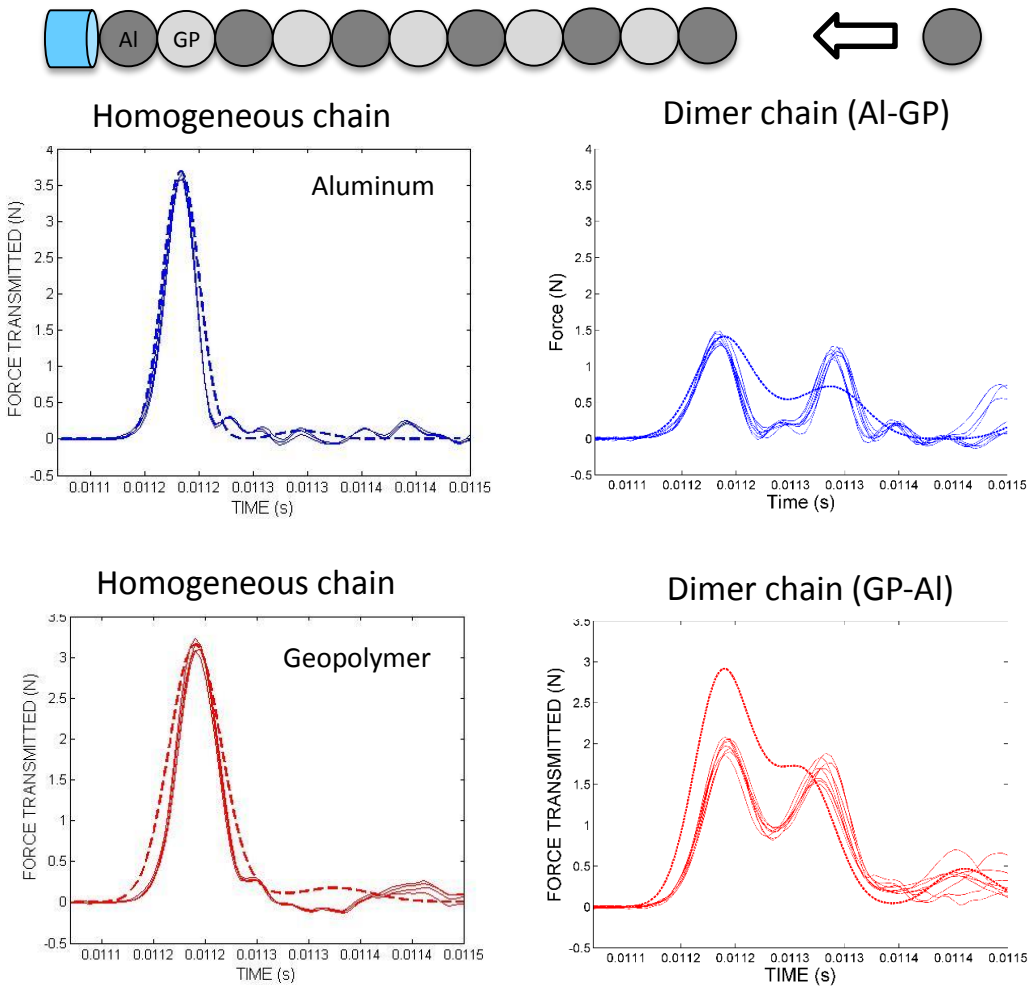

Fig. 5.11. Comparisons between experimental results and simulations of transmitted forces of dimer chains under fixed sliding input, 6N. The results of homogeneous chains were compared with those of dimer chains.

Dimer chains were constructed by substituting 5 beads in the homogeneous chain within the heavy-light-heavy-light permutation. The main beads of the dimer chain meant that the end bead (left-most), first bead (right-most) and striking bead should be the same. In Fig. 5.11, the blue line indicated the aluminum main chain with geopolymer beads as light beads. On the other hand, the red line showed the dimer effects of geopolymer main chain with aluminum beads. The transmitted forces of dimer chains are described in Fig. 5.11 and the experimental results are

compared with simulation for both cases. The dimer chain showed a lower value at the first peak of the response than that of the homogeneous chain and the second peak was developed by a significant amount, comparable to the first peak. By comparing the peak value of the first wave between the homogeneous and dimer chain, the aluminum main chain with geopolymer beads reduced the transmitted force from 3.7 to 1.5 N and geopolymer main chain also lowered the transmitted force from 3.1 to 2 N. These observation indicated that the dimer effect actually reduced the transmitted forces in different permutations. The same procedure was repeated for the homogenous chain applied to match the numerical simulation to experimental results for the dimer chains. The same damping values of the homogeneous chain for the main beads were used in the dimer chains (aluminum main chain: 2.55 Ns/m and geopolymer main chain: 1.31 Ns/m) and the first peak of the aluminum main chain was fitted to the experimental results. However, the profile of the second peak of aluminum main chain was destroyed when the damping value of aluminum beads was used. On the other hand, the first peak of the geopolymer main chain was not fitted in the simulation by using the damping value of geopolymer beads.

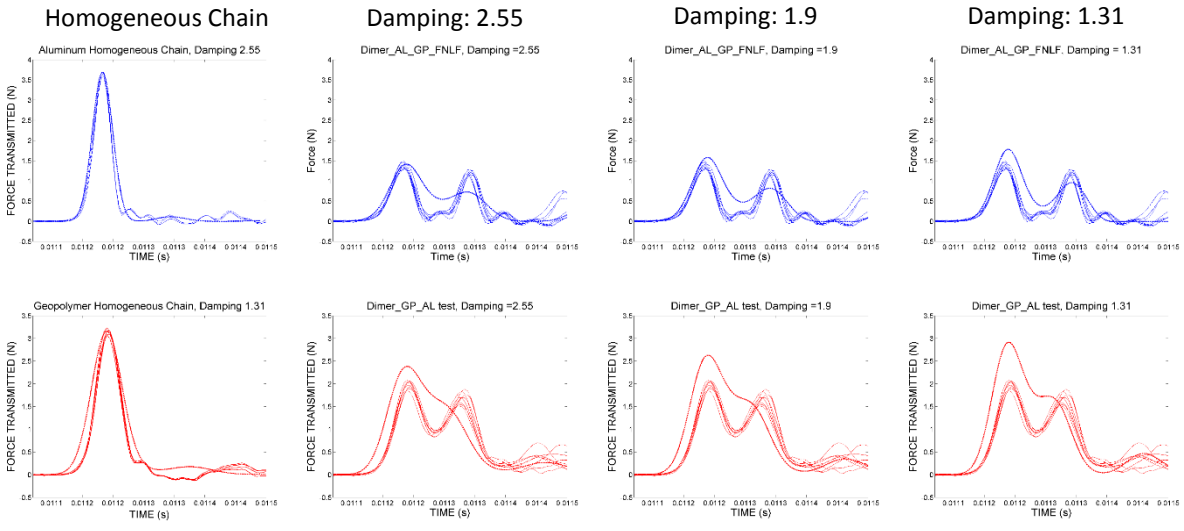

Fig. 5.12. Comparisons between experimental results and simulations of transmitted forces of dimer chains with different damping values under fixed sliding input, 6N.

Therefore, different damping values were used to fit the first and second peaks as shown in the Fig. 5.12. The lowest damping value was confined to the value of the geopolymer homogeneous chain (1.31 Ns/m) and the highest value was limited as a damping of the aluminum chain (2.25 Ns/m). For the aluminum main chain with geopolymer interstices, the highest damping fitted the first peak value but was destroyed in the second peak. When the damping decreased, the second peak was developed to fit the overall profile but the increased first peak induced a deviation from the experimental results. On the other hand, for the geopolymer main chain it was hard to fit the simulation to the experiment since the highest damping value from the aluminum beads even did not fit the first peak of the experimental results. The further higher damping could reduce the first peak value but it destroyed the overall profile. With the lowest damping value, the second peak of the geopolymer main chain was not developed enough to show the trend in the overall profile. With current numerical model of dimer chains, the transmitted force profile could not be fitted to the experimental results by changing the damping values. Further modification of modeling should be performed to carry out the impedance mismatch between the end bead (aluminum or geopolymer) and the force transducer (stainless steel).

ii. Free Drop Input

The vertical bead array allowed us to calculate a more reliable initial velocity for striking beads compared to that of the sliding input and there was no impedance mismatch between the end bead and the force transducer since the main beads of the dimer chains were fixed as stainless steel beads. The de-convolution process should be carried out to get rid of the effect of

the force transducer in the response of transmitted forces. After de-convolution, the initial force was 250 N and the velocity was 0.92 m/s as shown in Fig. 5.13.

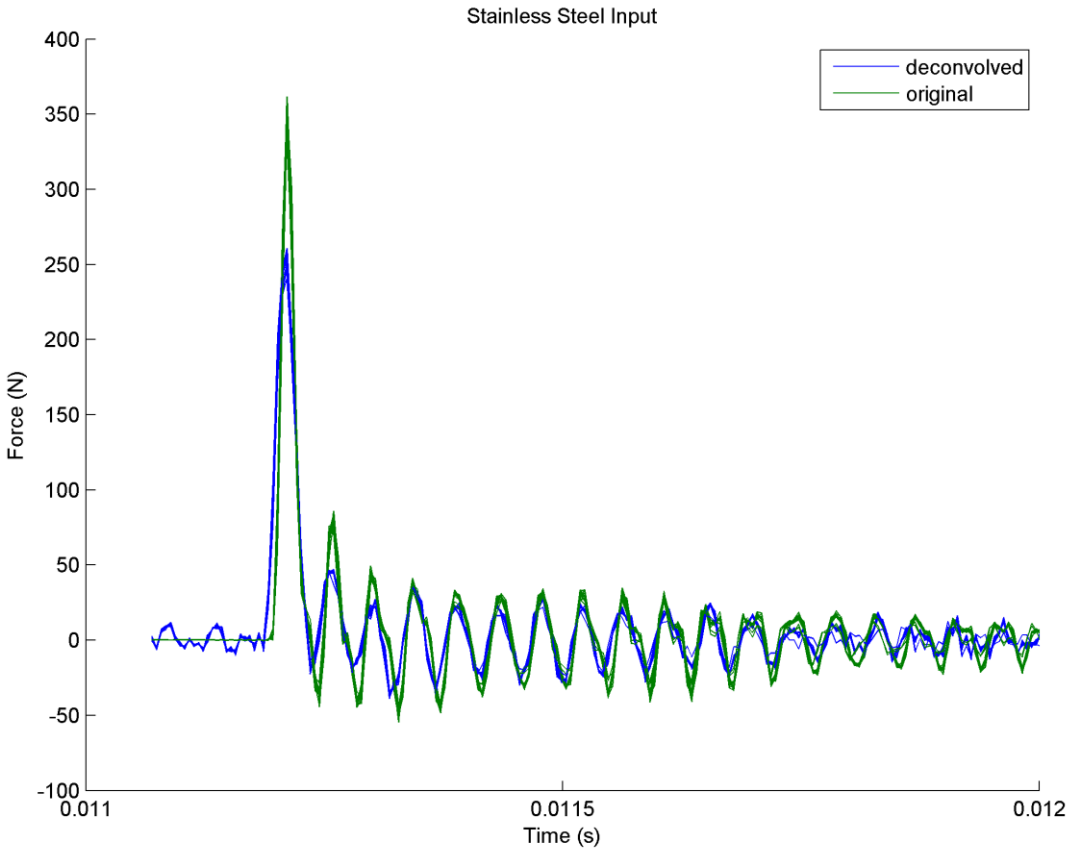

Fig. 5.13. Transmitted force of free drop input with/without de-convolution.

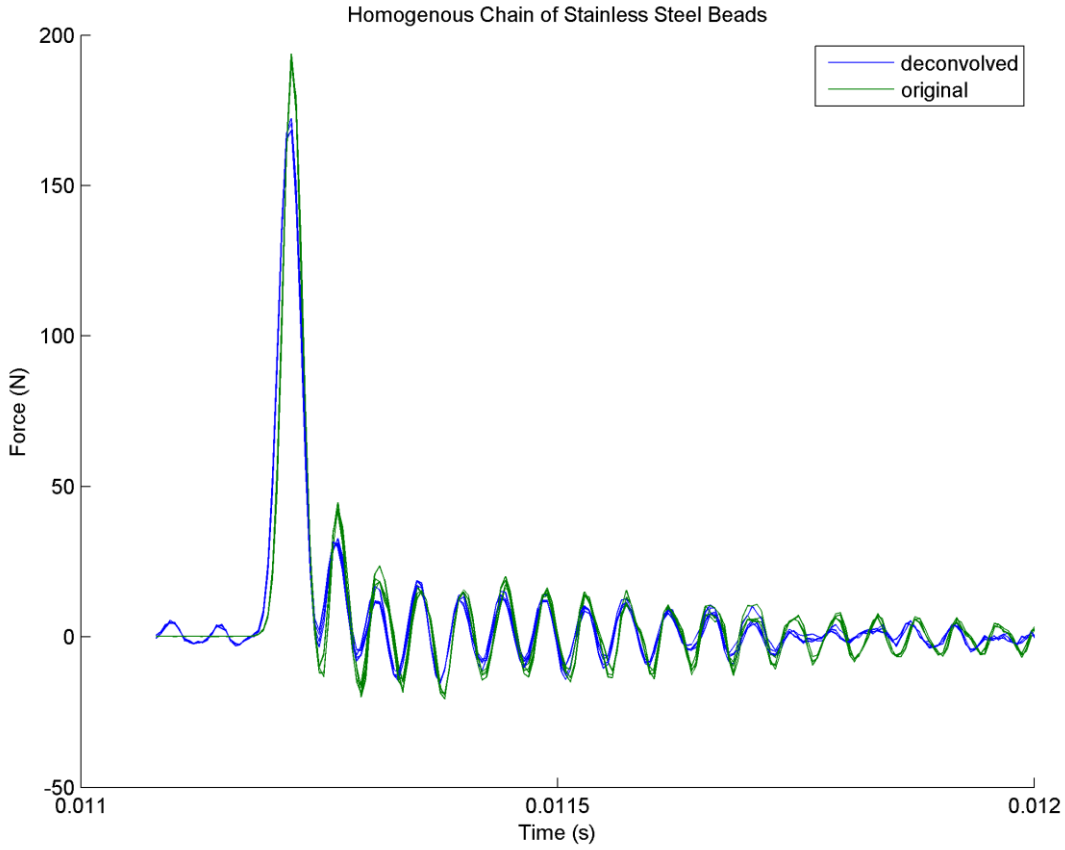

Fig. 5.14. Transmitted force of homogeneous chain of stainless steel beads with/without de-convolution under fixed free drop input, 250N and 0.92 m/s.

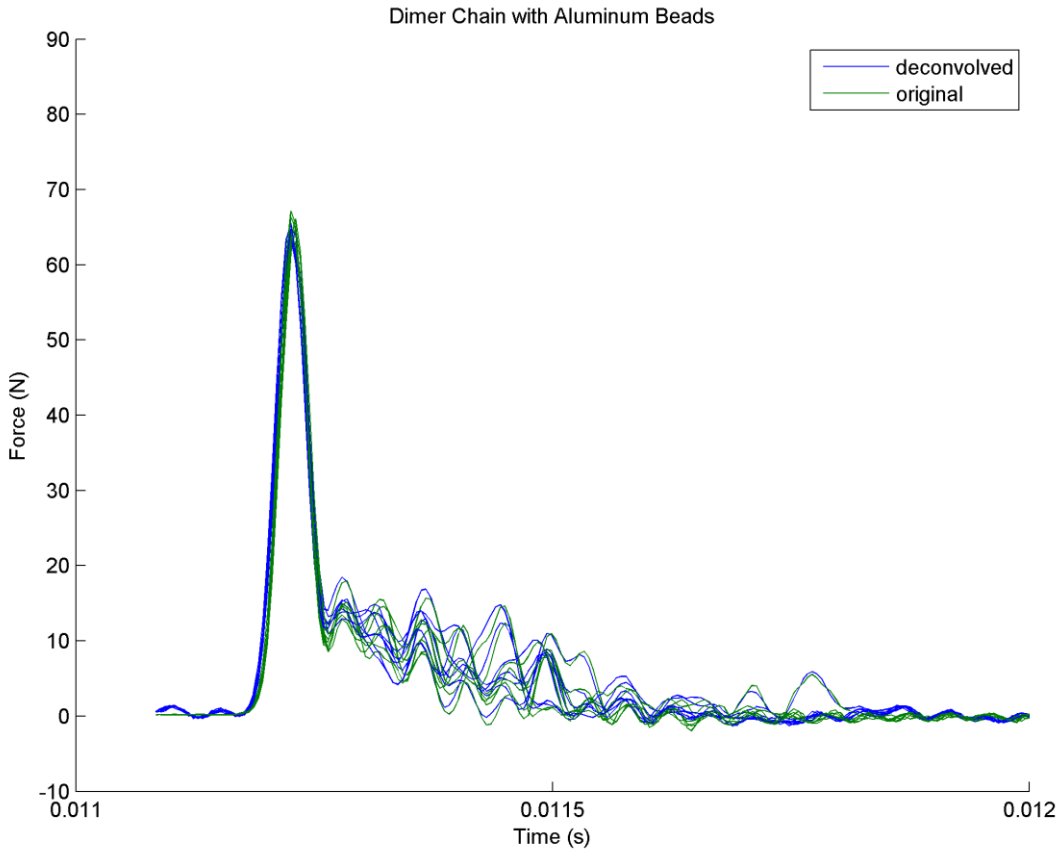

Fig. 5.15. Transmitted force of dimer chain with aluminum beads with/without de-convolution under fixed free drop input, 250N and 0.92 m/s.

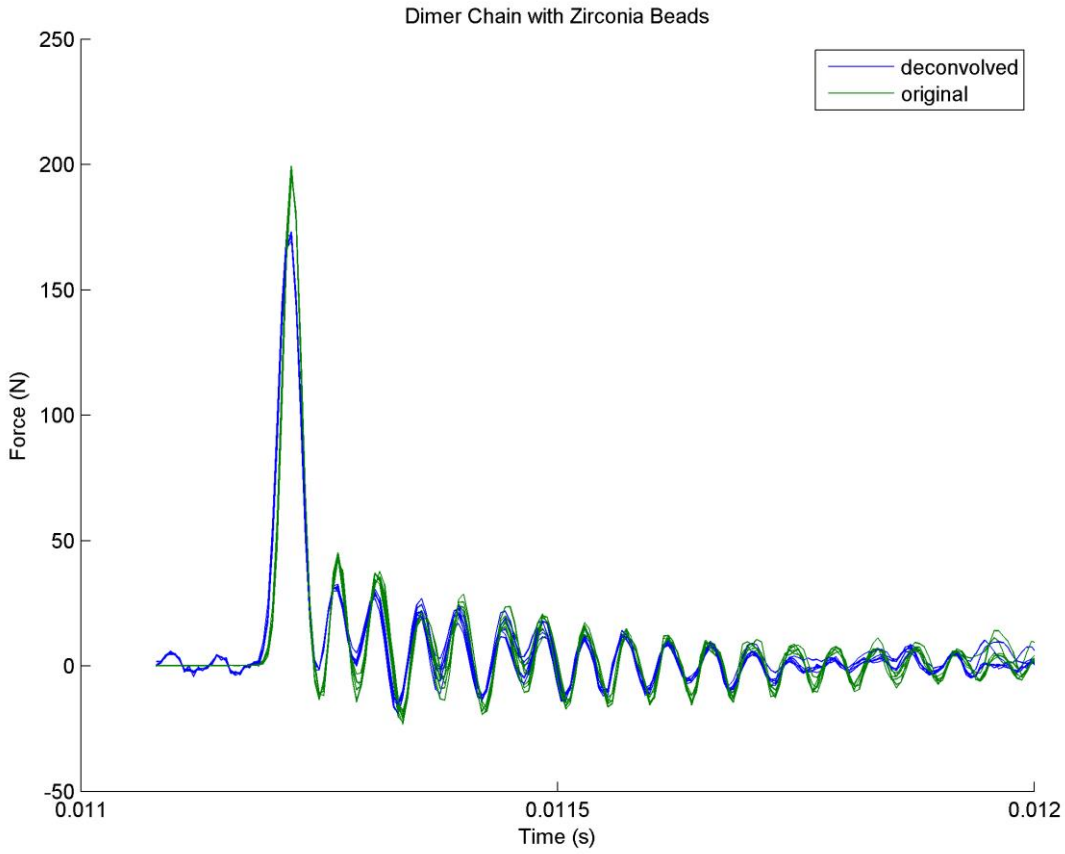

Fig. 5.16. Transmitted force of dimer chain with zirconia beads with/without de-convolution under fixed free drop input, 250N and 0.92 m/s.

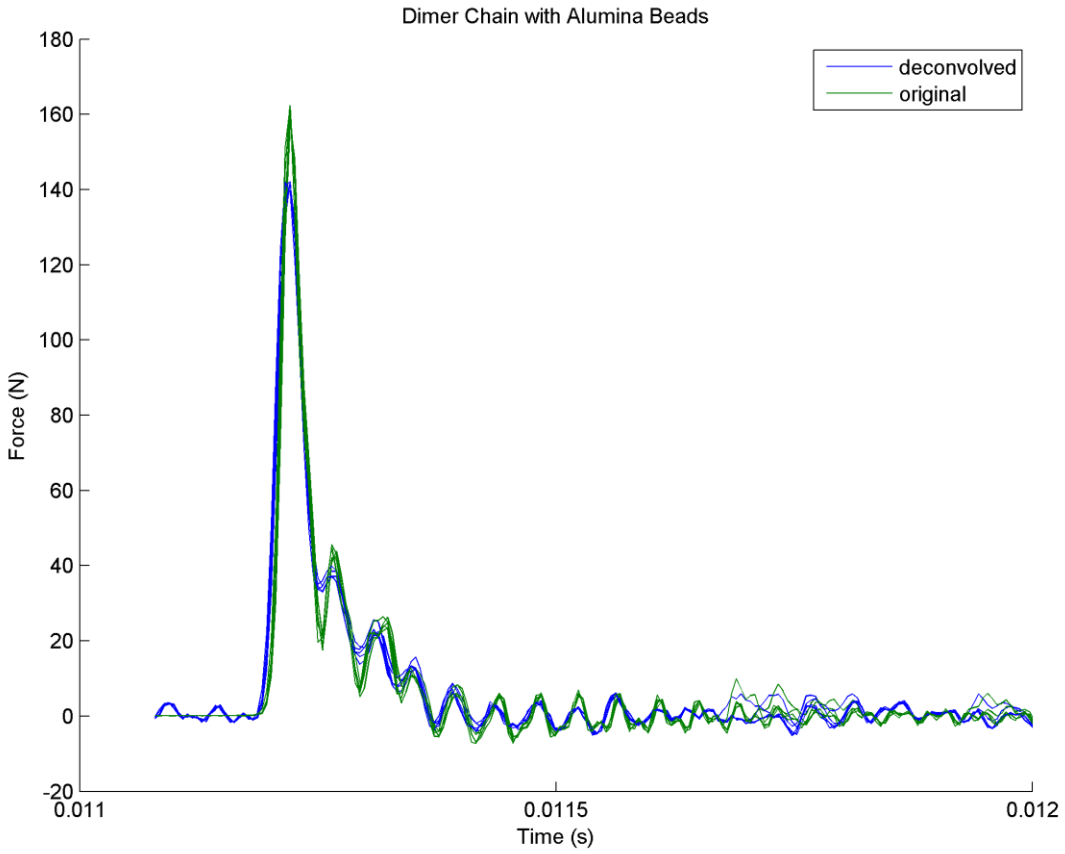

Fig. 5.17. Transmitted force of dimer chain with alumina beads with/without de-convolution under fixed free drop input, 250N and 0.92 m/s.

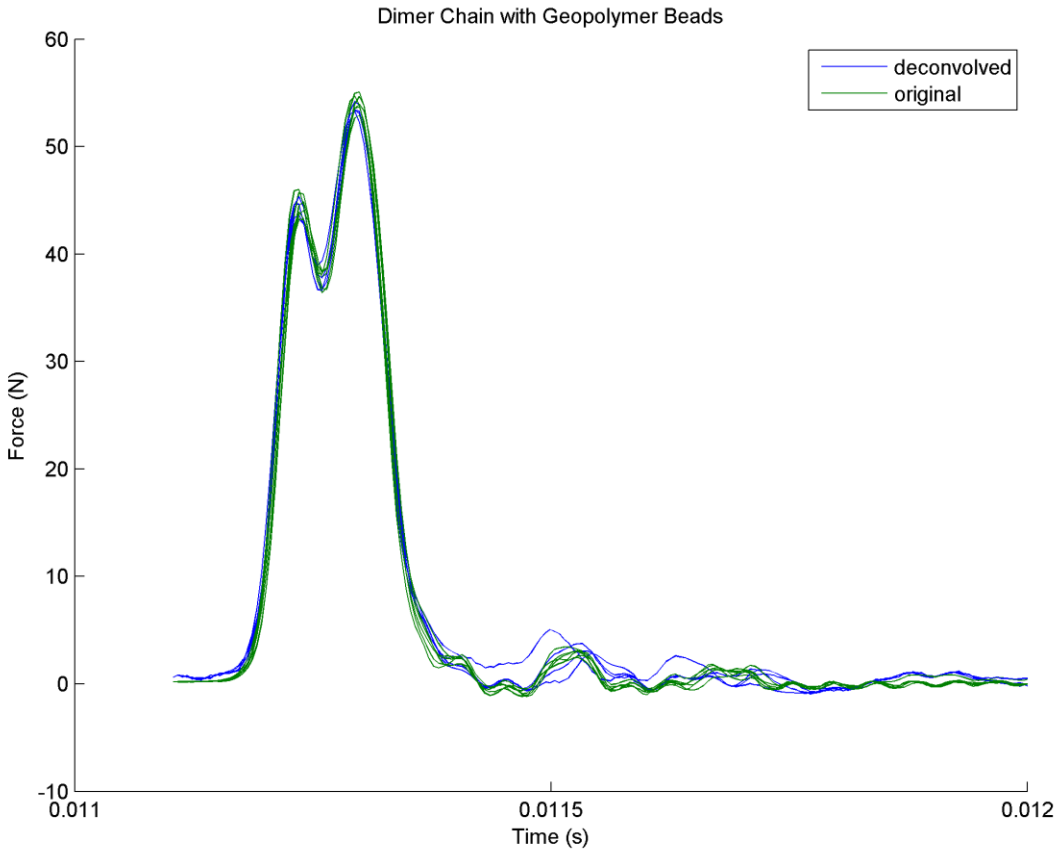

Fig. 5.18. Transmitted force of dimer chain with geopolymer beads with/without de-convolution under fixed free drop input, 250N and 0.92 m/s.

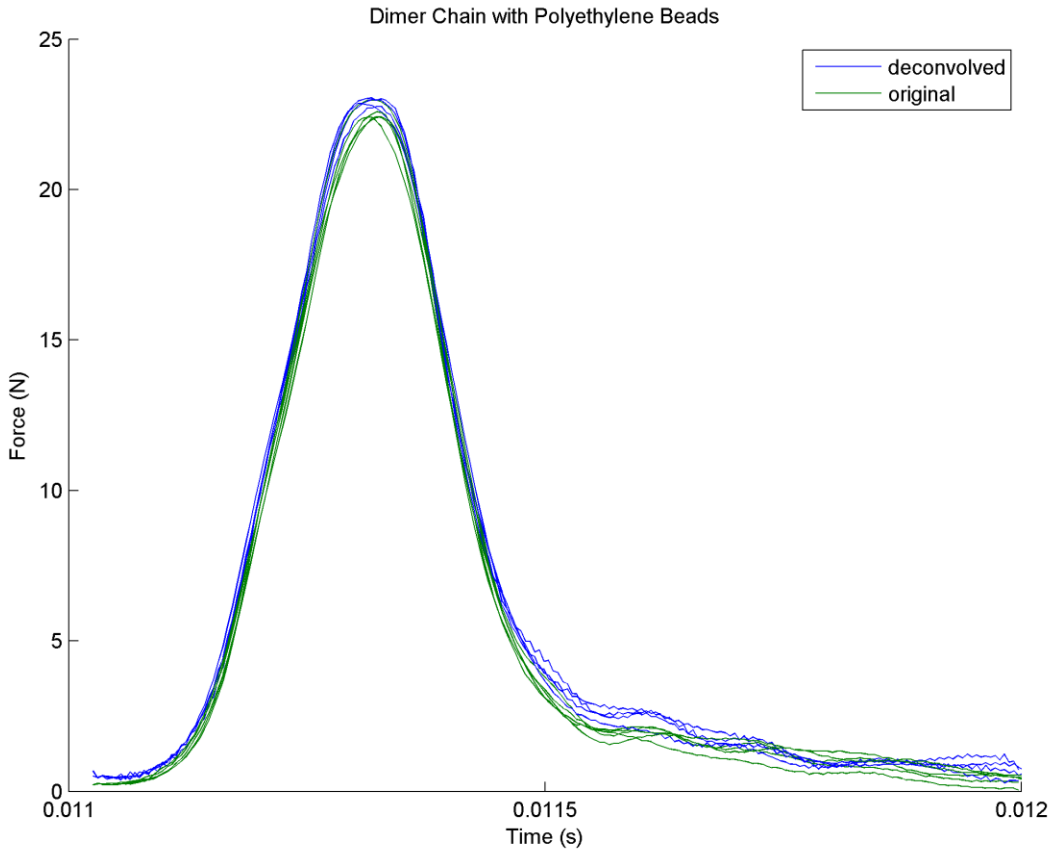

Fig. 5.19. Transmitted force of dimer chain with polyethylene beads with/without de-convolution under fixed free drop input, 250N and 0.92 m/s.

Table 5.2. Transmitted Forces and Absorption Ratios of Dimer Chains after de-convolution

	Transmitted Force (N)	F_T / F_I	Absorption (%)	Absorption Ratio	Absorption Ratio / kg
S.S	250				
S.S-S.S	170	0.68	32	1	1
S.S-A.L	62	0.25	75	2.35	3.37
S.S-Z.O	170	0.68	32	1	1.16
S.S-Al_2O_3	140	0.56	44	1.38	1.79
S.S-G.P	53	0.21	79	2.46	3.96
S.S-P.E	22	0.09	91	2.85	4.75

The transmitted force profiles are seen in Figs. 5.15-19. The maximum transmitted force of each dimer chains was obtained and the ratio of absorption was quantified for each system as

shown in Table 5.2. The absorption ratios which were normalized by the absorption of the homogeneous chain were further analyzed by considering the actual weight of the dimer chains. For the metal beads, the dimer chain with aluminum absorbed 3.37 times more energy than did the stainless steel homogeneous chain. For the ceramic beads, the highest absorption was observed in the dimer chain containing geopolymer beads, 3.96 times higher absorption. Note that the dimer chains with other ceramics beads, zirconia and alumina, showed an increase of the absorption ratios, 1.16 and 1.79, respectively, although the elastic modulus of those ceramics were higher than stainless steel. The dimer chain with polyethylene beads showed the highest absorption, 4.75 times higher than that of the homogeneous chain, among different types of beads due to its high damping, as shown in the transmitted force profile, which broadened the first peak.

5.5 Conclusion and Discussion

In this work, the two chains embedded in a PDMS matrix and a one dimensional granular chain composed of different types of beads and dimer chains were experimentally studied to investigate the capacity of stress wave mitigation by their intrinsic strongly nonlinear dynamics. The energy transfer from the excited chain to the absorbing chain through the matrix was observed by measuring the velocity profiles of end beads by laser vibrometry. The lower gap between chains induced higher energy transfer for the same material, PDMS in this study. The analytical study proposed that half of the energy from the excited chain could be transferred to the absorbing chain when the matrix had 11 times higher elastic properties to those of PDMS.

The one dimensional homogenous chains (without a matrix) containing different types of beads, aluminum, geopolymer and polyethylene, were tested to investigate the formation of a

solitary-like wave and their responses to transmitted forces from the force transducer were compared for each chain. The profile of the transmitted force of the geopolymer chain was comparable to that of the aluminum chain, which indicated that the geopolymer could conserve nonlinear dynamics in granular media. However, the polymer bead chain showed a broadening effect for the first peak of a solitary-like wave due to its low elastic modulus and high damping. Although the amplitude of the transmitted force was minimized in the polymer chain, the attenuation mechanism of the polymer chain was damping of the material itself rather than due to the nonlinear dynamics of the granular media. It was concluded that geopolymer can substitute for other metal beads to construct lightweight granular media (6 times lighter than stainless steel) while it conserved the theoretical analyses based on metal granular media.

For the dimer chain, the main beads of the chain were stainless steel beads to reduce the effect of impedance mismatch between the end bead and the force transducer and five different types of beads (aluminum, zirconia, alumina, geopolymer and polyethylene) having the same radii were used as dimer interstices (heavy-light bead paring). Since the transmitted force was measured through a force transducer, the internal dynamics of the force transducer should be considered to be removed by a de-convolution process for further analyses. The energy absorption or dissipation ratio increased with dimer chains. In particular containing the dimer chain geopolymer beads showed almost 4 times better stress wave mitigation than that of stainless steel homogenous chains.

5.6 References

1. V. F. Nesterenko, "Dynamics of Heterogeneous Materials.″ Springer Science & Business Media, (2001).

2. C. Coste and B. Gilles, "Sound Propagation in a Constrained Lattice of Beads: High-Frequency Behavior and Dispersion Relation," *Physical Review E,* **77**[2] 021302 (2008).

3. C. Daraio, V. Nesterenko, E. Herbold and S. Jin, "Energy Trapping and Shock Disintegration in a Composite Granular Medium," *Physical Review Letters,* **96**[5] 058002 (2006).

4. F. Fraternali, M. A. Porter and C. Daraio, "Optimal Design of Composite Granular Protectors," *Mechanics of Advanced Materials and Structures,* **17**[1] 1-19 (2009).

5. K. Jayaprakash, Y. Starosvetsky, A. F. Vakakis, M. Peeters and G. Kerschen, "Nonlinear Normal Modes and Band Zones in Granular Chains with No Pre-Compression," *Nonlinear Dynamics,* **63**[3] 359-85 (2011).

6. M. A. Hasan, S. Cho, K. Remick, A. F. Vakakis, D. M. McFarland and W. M. Kriven, "Experimental Study of Nonlinear Acoustic Bands and Propagating Breathers in Ordered Granular Media Embedded in Matrix," *Granular Matter,* **17**[1] 49-72 (2015).

7. A. Spadoni and C. Daraio, "Generation and Control of Sound Bullets with a Nonlinear Acoustic Lens," *Proceedings of the National Academy of Sciences,* **107**[16] 7230-34 (2010).

8. C. M. Donahue, P. W. Anzel, L. Bonanomi, T. A. Keller and C. Daraio, "Experimental Realization of a Nonlinear Acoustic Lens with a Tunable Focus," *Applied Physics Letters,* **104**[1] 014103 (2014).

9. Y. Starosvetsky, M. A. Hasan, A. F. Vakakis and L. I. Manevitch, "Strongly Nonlinear Beat Phenomena and Energy Exchanges in Weakly Coupled Granular Chains on Elastic Foundations," *SIAM Journal on Applied Mathematics,* **72**[1] 337-61 (2012).

10. A. Leonard, F. Fraternali and C. Daraio, "Directional Wave Propagation in a Highly Nonlinear Square Packing of Spheres," *Experimental Mechanics,* **53**[3] 327-37 (2013).

11. M. Manjunath, A. P. Awasthi and P. H. Geubelle, "Plane Wave Propagation in 2d and 3d Monodisperse Periodic Granular Media," *Granular Matter,* **16**[1] 141-50 (2014).

12. K. Jayaprakash, A. F. Vakakis and Y. Starosvetsky, "Solitary Waves in a General Class of Granular Dimer Chains," *Journal of Applied Physics,* **112**[3] 034908 (2012).

13. R. Potekin, K. Jayaprakash, D. McFarland, K. Remick, L. Bergman and A. Vakakis, "Experimental Study of Strongly Nonlinear Resonances and Anti-Resonances in Granular Dimer Chains," *Experimental Mechanics,* **53**[5] 861-70 (2013).

14. S. Sen, J. Hong, J. Bang, E. Avalos and R. Doney, "Solitary Waves in the Granular Chain," *Physics Reports,* **462**[2] 21-66 (2008).

15. N. Boechler, G. Theocharis and C. Daraio, "Bifurcation-Based Acoustic Switching and Rectification," *Nature Materials,* **10**[9] 665-68 (2011).

16. M. Hasan, Y. Starosvetsky, A. Vakakis and L. Manevitch, "Nonlinear Targeted Energy Transfer and Macroscopic Analog of the Quantum Landau–Zener Effect in Coupled Granular Chains," *Physica D: Nonlinear Phenomena,* **252** 46-58 (2013).

17. M. A. Hasan, S. Cho, K. Remick, A. F. Vakakis, D. M. McFarland and W. M. Kriven, "Primary Pulse Transmission in Coupled Steel Granular Chains Embedded in PDMS Matrix: Experiment and Modeling," *International Journal of Solids and Structures,* **50**[20] 3207-24 (2013).

18. Y. Zhang, M. A. Hasan, Y. Starosvetsky, D. M. McFarland and A. F. Vakakis, "Nonlinear Mixed Solitary—Shear Waves and Pulse Equi-Partition in a Granular Network," *Physica D: Nonlinear Phenomena,* **291** 45-61 (2015).

19. K. Jayaprakash, Y. Starosvetsky, A. F. Vakakis and O. V. Gendelman, "Nonlinear Resonances Leading to Strong Pulse Attenuation in Granular Dimer Chains," *Journal of nonlinear science,* **23**[3] 363-92 (2013).

20. D. C. Arik Avagyan, Nathan Dostart, Kaiyuan Zhu, Shinhu Cho, A. F. Vakakis, D. M. McFarland and W. M. Kriven, "Experimental Study of Embedded-in-Matrix and Non-Embedded Ordered Granular Chains under Impulsive Excitation," *Sumitted; GranularMatter* (2015).

21. D. Fuard, T. Tzvetkova-Chevolleau, S. Decossas, P. Tracqui and P. Schiavone, "Optimization of Poly-Di-Methyl-Siloxane (PDMS) Substrates for Studying Cellular Adhesion and Motility," *Microelectronic Engineering,* **85**[5] 1289-93 (2008).

22. K. Khanafer, A. Duprey, M. Schlicht and R. Berguer, "Effects of Strain Rate, Mixing Ratio, and Stress–Strain Definition on the Mechanical Behavior of the Polydimethylsiloxane (Pdms) Material as Related to Its Biological Applications," *Biomedical Microdevices,* **11**[2] 503-08 (2009).

23. M. A. Eddings, M. A. Johnson and B. K. Gale, "Determining the Optimal PDMS–PDMS Bonding Technique for Microfluidic Devices," *Journal of Micromechanics and Microengineering,* **18**[6] 067001 (2008).

24. K.-S. Koh, J. Chin, J. Chia and C.-L. Chiang, "Quantitative Studies on PDMS-PDMS Interface Bonding with Piranha Solution and Its Swelling Effect," *Micromachines,* **3**[2] 427-41 (2012).

25. S. Cho, R. D. Schmidt, E. D. Case and W. M. Kriven, "Short Carbon Fiber-Reinforced, Geopolymer Composites. Part II. Effect of Fiber Length on Mechanical Properties," *Submitted; Ceramics International (2015).*

CHAPTER 6: CONCLUSIONS AND RECOMMENDATIONS FOR FUTURE WORK

6.1 Conclusions

In this research, the potassium geopolymer composites have been made containing various reinforcements, 60 and 100 μm carbon fibers and graphene nanoplatelets, with or without silicon groups. Various test methods used to investigate the mechanical properties of those composites as well as the microstructures. Moreover, Weibull analyses have been performed to find the optimal contents of reinforcements for desired properties. The IE and RUS techniques measured the Young's moduli and shear moduli of composites based on the frequency responses of given specimens with known dimensions. These are beneficial techniques for brittle materials since tensile testing is not applicable in most cases. These empirical results were compared to the various theoretical predictions as well. The measured elastic properties of potassium geopolymer were applied to the analysis of nonlinear dynamics of geopolymer bead chains.

Not only the mechanical properties but also the electrical and thermal properties of GNP KGP have been investigated since graphene has exceptional mechanical, thermal and electrical properties. To increase the interfacial bonding between GNP and the potassium geopolymer matrix, silicon functionalized GNP was fabricated by a plasma and chemical process. The mechanical properties increased as the amount of GNP or sGNP increased. The electrical conductivity of GNP KGP improved approximately 29 times higher than that of pure KGP and the electrical threshold was observed at 3 wt% of GNP contents. The thermal conductivity increased linearly with GNP contents.

The geopolymer beads were created by simple injection in PDMS mold. The solitary-like wave formation of homogeneous geopolymer chain was verified by measuring the transmitted force under impact excitation. The de-convolution method was used to obviate the dynamics of the force transducer itself from the response of the transmitted force. The dimer chains composed of geopolymer beads performed four times better in energy absorption compared to the stainless steel homogeneous chain and resulted in the lightweight granular acoustic metamaterials.

6.2 Recommendations for Future Work

SELF-ASSEMBLED POROUS MATERIALS AS A NEW CLASS OF STRONG AND LIGHTWEIGHT METAMATERIALS

a. Proposal Summary

Lightweight and mechanically strong materials have been reported made from different manufacturing techniques such as two-photon lithography[1] or projection microstereolithography[2]. In particular, nano ceramic lattice structures in Figure 6.1 fully recovered their shape under compression loading[3], which is not achievable in general due to their brittleness and sensitivity to flaws. The size effect plays an important role in nanostructures in order to achieve their exceptional properties. Therefore, sophisticated manufacturing processes are required to construct such small structures. On the other hand, complicated manufacturing and material processing require significant amounts of time and

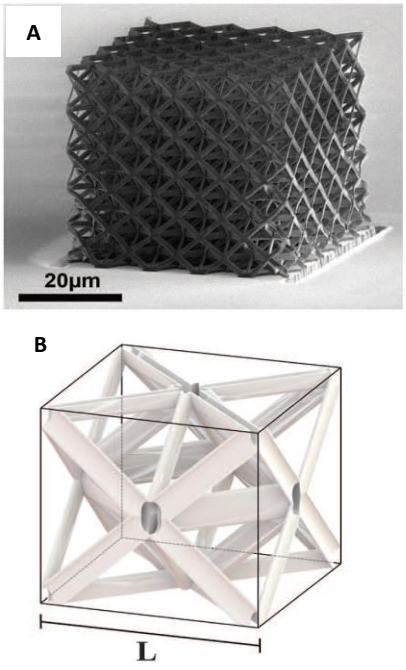

Figure 6.1. Architecture, design, and microstructure of alumina nanolattices. (A) SEM image of alumina octet-truss nanolattices. (B) Cutaway of hollow octet-truss unit cell[3].

resources. For easy processing and mass production, a new class of self-assembled nanoporous ceramics could be introduced. Since this new material has self-assembled nano and micro structures in nature, we can reduce the size of a single unit cell (Figure 6.1, B) of strong and lightweight ceramic structures from 5 μm^3 to 20 nm (overcoming the size limitation of current lithographic techniques) as well as simplifying the entire manufacturing processes for mass production.

b. Research Objectives

The research objective of this proposal is to investigate and develop a new class of self-assembled nanoporous ceramics, which is called aluminosilicate inorganic polymer or "geopolymer", as a next generation metamaterial that can be a strong and lightweight three-dimensional structure. The following research tasks should be carried out to accomplish such a new paradigm for metamaterials:

1) Investigation of the mechanical properties of self-assembled nanoporous inorganic polymer (geopolymer) on a nanoscale to achieve the ultrastrong and ultralight properties
2) Design and fabrication of three-dimensional geopolymer structure with controlled porosity and pore size by incorporating two-photon lithography
3) Mass production of strong and lightweight metamaterials using a molding process or additive manufacturing with geopolymer which is a liquid precursor ceramic.

c. Proposed Approach

Geopolymer is formed by shear mixing aluminosilicate materials (highly reactive metakaolin) with alkali or alkali-silicate solutions at ambient temperatures followed by curing within 24 hours. Geopolymer is X-ray amorphous and consists of four coordinated (IV) silica and alumina tetrahedra, where the charge of AlO_4^- tetrahedra are balanced by hydrated alkali cations,[4] as shown in Figure 6.2. Mechanical strength, rapid setting and substantial chemical and thermal resistances are dependent on the molar ratio and material selections. Due to the cost and performance concerns, the potassium based geopolymer ($K_2O \cdot Al_2O_3 \cdot 4SiO_2 \cdot 11H_2O$) could be used.

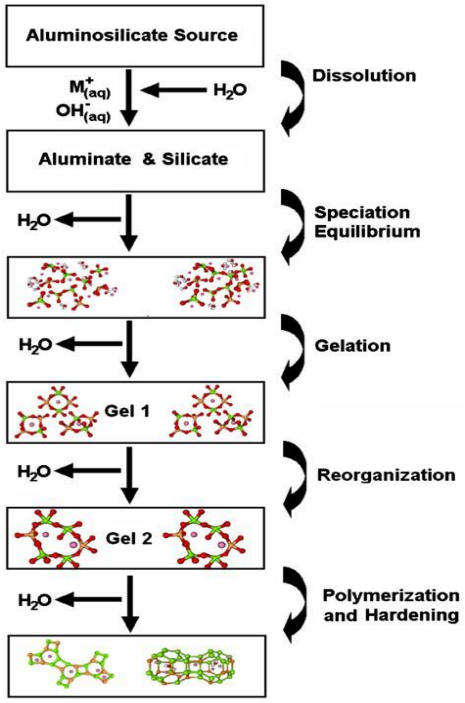

Figure 6.2. Conceptual model for geopolymerization[4]

There are three-part chemical reactions to form geopolymers. The aluminosilicate source (metakaolin) is dissolved into highly alkaline solution. Then, polymerization of SiO_4 and AlO_4^- tetrahedral occurs, followed by precipitating into circular polysialates. The precipitate diameter is of the order of 20 ~ 30 nanometers for potassium-based polysialates precipitates[5]. In Figure 6.3, we observed the existence of self-assembled sub-nanotexture inside individual precipitates by HRTEM[6] and we have recently measured the average size of pore diameter of 0.5 nm by Positron Annihilation Lifetime Spectroscopy (PALS). In this proposal, we suggest to use potassium-based geopolymer as a source of strong and lightweight metamaterial. The individual precipitate corresponds to the unit cell of the lattice structure and the self-assembled porosity inside the precipitate corresponds to the designed structure of the unit cell. Thus, we could

reduce the size of a unit cell by about 250 times smaller. In order to accomplish this exciting concept, focused ion beam milling (FIB) and compression testing by an in situ nanomechanical instrument (InSEM) should be incorporated to fabricate nanostructures and measure the mechanical responses of brittle geopolymer at the nanoscale.

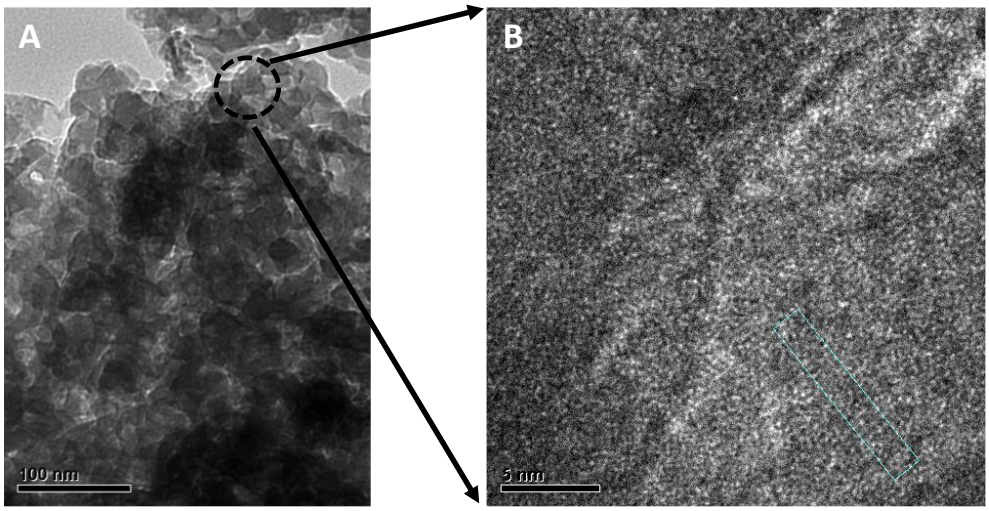

Figure 6.3. (A) TEM micrographs for geopolymer in high magnification. (B) HRTEM image of precipitates of geopolymer showing amorphous sub-nanometer structure[6]

The sub-nanometer pores are self-assembled during polymerization of SiO_4 and AlO_4^- tetrahedra while closed pores are also formed between precipitates in the precipitation process. Fully reacted potassium geopolymer has 40 vol% porosity with an average pore size of 6.8 nm in diameter due to the closed pores between precipitates. The size of closed pores and porosity can be controlled by adding functionalized alkoxysilane where geopolymer clusters are self-assembled. The maximum size of pores and porosity are 1 μm in diameter and 75 vol%, respectively[7]. The self-assembled closed pores between precipitates correspond to the unit cell of the lattice structure in this case. Therefore, taking advantage of the self-assembled broad range of pore size and porosity of geopolymers, we can easily scaled up the strong and lightweight nano structures to micro, meso and even macro sizes without involving a complicated manufacturing processes. In order to prove this concept, the FIB will be used to cut the pore size controlled

geopolymers down to nano and micro cubes and the compression test will be performed by the in situ nanomechanical instrument.

Note that the lithography process was skipped in this proposed work since the self-assembled porous material itself can substitute for the man-made, three-dimensional nano structure, while maintaining the exceptional mechanical properties. In this Ph.D. work, it has been verified that geopolymers can imprint nano features[8], so that the three-dimensional structure can be imprinted on geopolymers by a simple molding process. Moreover, additive manufacturing can be applicable since geopolymer is a liquid-based ceramic precursor. Therefore, once we can prove the concept of geopolymer as a new class of metamaterial, the manufacturing process will be significantly simplified to save time and money, which will result in mass production.

6.3 References

1. D. Jang, L. R. Meza, F. Greer and J. R. Greer, "Fabrication and Deformation of Three-Dimensional Hollow Ceramic Nanostructures," *Nature materials,* **12[10]** 893-98 (2013).

2. X. Zheng, H. Lee, T. H. Weisgraber, M. Shusteff, J. R. Deotte, E. Duoss, J. D. Kuntz, M. M. Biener, S. O. Kucheyev and Q. Ge, "Ultra-Light, Ultra-Stiff Mechanical Metamaterials," *Science,* **344[6190]** 1373-77 (2014).

3. L. R. Meza, S. Das and J. R. Greer, "Strong, Lightweight, and Recoverable Three-Dimensional Ceramic Nanolattices," *Science,* **345[6202]** 1322-26 (2014).

4. P. Duxson, A. Fernández-Jiménez, J. L. Provis, G. C. Lukey, A. Palomo and J. S. J. Van Deventer, "Geopolymer Technology: The Current State of the Art," *Journal of Materials Science,* **42[9]** 2917-33 (2007).

5. W. M. Kriven, "Inorganic Polysialates or" Geopolymers"," *American Ceramics Society Bulletin,* **89[4]** 31-34 (2010).

6. J. L. B. W. M. Kriven, S. W. Mallicoat and M. Gordon, "Intrinsic Microstructure and Properties of Metakaolin-Based Geoolymers," *contributed chapter to Proc. of Int. Worshop on Geopolymer Binders – Interdependence of Composition, Structure and Properties, Weimar, Germany* **71-86** (2007).

7. B. E. Glad and W.M. Kriven, Highly Porous Geopolymers through Templating and Surface Interactions." *Journal of the American Ceramic Society,* (2015).

8. S. Cho and W. M. Kriven, "Short Carbon Fiber-Reinforced, Geopolymer Composites. Part I. Intrinsic Mechanical Properties," *Submitted; Ceramics International* (2015).